MATERIALS-STRUCTURE-PROPERTY CORRELATION OF TUNGSTEN CONTAINING HIGH ENTROPY ALLOYS

Ph.D. Thesis

DEVESH KUMAR

(I.D. 2014RMT9535)

DEPARTMENT OF METALLURGICAL AND MATERIALS ENGINEERING

MALAVIYA NATIONAL INSTITUTE OF TECHNOLOGY

JAIPUR

April 2019

Materials-Structure-Property Correlation of Tungsten Containing High Entropy Alloys

Submitted in

fulfillment of the requirements for the degree of

Doctor of Philosophy

by

Devesh Kumar
(2014RMT9535)

Under the Supervision of

Dr. Vinod Kumar **Dr. Y.V.S.S. Prasad** **Dr. V.K. Sharma**

Department of Metallurgical and Materials Engineering
MALAVIYA NATIONAL INSTITUTE OF TECHNOLOGY
JAIPUR

April 2019

Dedicated to:

My Parents: Sh. Rajesh Mittal

Smt. Madhu Mittal

My wife: Mrs. Sonam Mittal

My Daughter: Ms. Dishi Mittal

DECLARATION

I, **Devesh Kumar**, declare that this thesis titled, **"Materials-Structure-Property Correlation of Tungsten Containing High Entropy Alloys"** and the work presented in it, are my own. I confirm that:

- This work was done wholly or mainly while in candidature for a research degree at this institution.
- Where any part of this thesis has previously been submitted for a degree or any other qualification at this institution or any other university, this has been clearly stated.
- Where I have consulted the published work of others, this is always clearly attributed.
- Where I have quoted from the work of others, the source is always given. With the exception of such quotations, this thesis is entirely my own work.
- I have acknowledged all main sources of help.
- Where the thesis is based on work done by myself, jointly with others, I have made clear exactly what was done by others and what I have contributed myself.

Date:

Devesh Kumar

(2014RMT9535)

CERTIFICATE

This is to certify that the thesis entitled **"Materials-Structure-Property Correlation of Tungsten Containing High Entropy Alloys"** being submitted by **Mr. Devesh Kumar (ID: 2014RMT9535)** is a bonafide research work carried out under our supervision and guidance in fulfillment of the requirement for the award of the degree of **Doctor of Philosophy** in the Department of Metallurgical and Materials Engineering, Malaviya National Institute of Technology, Jaipur, India. The matter embodied in this thesis is original and has not been submitted to any other University or Institute for the award of any other degree.

Dr.Vinod Kumar	**Dr.Y.V.S.S.Prasad**	**Dr. V.K.Sharma**
(Co-Supervisor External)	**(Co-Supervisor Internal)**	**(Supervisor)**
Discipline of Metallurgy Engg. & Materials science IIT Indore, India	Dept. of Met.& Mat Engineering MNIT, Jaipur, India	Dept. of Met. & Mat. Engineering MNIT, Jaipur, India

Place: Jaipur

Date:

ACKNOWLEDGEMENT

I would like to first say a very big thank you to my supervisor **Dr**. **V. K. Sharma** for all the support and encouragement he gave me, during my completion of thesis. Without his guidance and support me in some challenging period, this Ph.D. would not have been achievable.

I am really indebted to my Co-supervisor **Dr. Y. V. S. S. Prasad** who provided me precious opportunity to pursue research under their guidance. After that, I also give my special thanks to my Co-supervisor **Dr. Vinod Kumar** for his guidance and providing a new platform of wonderful and challenging materials world. His unique guiding quality, interest, working enthusiasm and analytical approach towards the experimental results impressed me so much. It is great honour for me to work with him.

I would like to express my sincere thanks to **Prof. M. K. Banerjee, Dr. Amar Patnaik and Dr. A. K. Pradhan** for being in my DREC committee as well as for their encouragement, analytical insights and recommendations. I further extend my thanks to **Prof. V. S. Raja (IIT Bombay),** all the staff members of **Materials Research Center (MNIT Jaipur) and ACMS (IIT Kanpur)** for providing characterization facilities and **BRNS, Mumbai** for the financial support.

I express my deep appreciation to my friends and co-workers **Dr. Ornov Maulik, Dr. Anil Kumar**, **Mr. Ankit Goyal**, **Mr. Arun Kumar, Mr. Saurav Kumar, Dr. Priyanka Meena, Mr. Sheetal Dewagan** and all the post graduate students of the department of Metallurgical and Materials Engineering for their moral support and help. I would like to extend my sincere thanks to all the faculty and staff members of MNIT, Jaipur for their support during my Ph.D.

I would also like to say a heartfelt thank you to my **Mummy, Papa, Amma and Baba** for always believing in me and encouraging me to follow my dreams and **Paras Ji, Shivani, and Annu,** for helping in whatever way they could during this challenging period.

And finally to **Sonam**, my wife who has been by my side throughout this PhD, living every single minute of it, and without whom, I would not have had the courage to embark on this journey in the first place. And to my darling **Dishi** for being such a good little baby that past three years, and making it possible for me to complete what I started. I would also give thanks **to my father in law, mother in law, Yatesh, Diksha and Pankaj** for their unconditional support.

(Devesh Kumar)

ABSTRACT

Novel $AlCuCrFeMnW_x$ (x= 0, 0.05, 0.1, 0.5 & 1 mol) high-entropy alloys (HEAs) have been synthesized by mechanical alloying followed by spark plasma sintering. The effect of tungsten content on the phase evolution of as-milled and bulk HEAs was investigated by using X-Ray diffractometry (XRD), transmission electron microscopy (TEM) and selected area electron diffraction (SAED) pattern analysis. The particle morphology and composition of HEAs were investigated by scanning electron microscopy (SEM) and electron dispersive spectroscopy (EDS) respectively. During Mechanical alloying, the formation of a supersaturated solid solution with the formation major BCC 1 and BCC 2 phase with minor FCC fraction in $AlCuCrFeMnW_x$ (x=0, 0.05, 0.1, 0.5 & 1 mol) HEAs. TEM–SAED analysis of $AlCuCrFeMnW_x$ HEAs concurred with XRD results. The phase stability with respect to temperature has been studied using a differential scanning calorimeter (DSC). Thermodynamic parameters for $AlCuCrFeMnW_x$ alloys are calculated and analyzed to explain the formation of a solid solution. The microstructure of bulk sintered $AlCuCrFeMnW_x$ (x=0, 0.05, 0.1 & 0.5 mol) HEAs consisted of predominantly AlFe type ordered structure, BCC phase and FeMn phase along with metastable Chromium rich σ-phase precipitates. Microstructure of AlCuCrFeMn was AlFe type ordered structure, FeMn phase with metastable Cr rich σ-phase precipitates. The formation and growth of Cr rich precipitates in FeMn phase in case of $AlCuCrFeMnW_x$ HEAs are due to the high enthalpy difference between the binary elements.

A peak hardness value of 891 HV has been observed in the case of AlCuCrFeMnW HEA due to the combined effect of solid solution hardening, grain boundary hardening and precipitation hardening. It was observed that the fracture strength under compression (σ_f) increased from 1010 to 1820 MPa with the increased tungsten content of $AlCuCrFeMnW_x$ (x=0, 0.05, 0.1, 0.5 & 1mol) HEAs. Further, materials-structure-property correlation has been established and a mathematical model has been proposed utilizing conventional strengthening mechanisms. Room temperature Creep studied using nanoindendation have been performed on a $AlCuCrFeMnW_x$ (x=0, 0.05, 0.1, 0.5 & 1 mol) HEAs at different maximum loads. The main mechanisms of creep are the dislocation creep at high indentation load and self-diffusion at low indentation loads.

The electrochemical performance of $AlCuCrFeMnW_x$ (x = 0, 0.05, 0.1, 0.5 & 1 mol) HEAs was studied in a 3.5 wt% NaCl solution. With the addition of tungsten, the corrosion potential of the

alloys increased from -0.892 V to -0.313 V and the corrosion current density decreased from 6.97 x 10^{-6} to 3.32 x 10^{-6} A/cm^2, which demonstrated that a high content of tungsten enhanced the corrosion resistance of the alloys. The FTIR and XRD spectra of the surface after the polarization experiment also showed that the formation of the passive layer WO_3 increased with the increase in the content of tungsten. The Nyquist plot was constituted with one capacitive semicircle at high frequency region and a long diffusion tail at low frequency region. The capacitive semicircle was attributed to the existing of a passive film. The present studies suggest that these alloys may have potential usage in structural and marine application.

CONTENTS

CHAPTER 3:

List of Figures

List of Table

LIST OF ABBREVIATIONS

HEA	High Entropy Alloy
MA	Mechanical Alloying
SPS	Spark Plasma Sintering
XRD	X-Ray Diffraction
SEM	Scanning Electron Microscopy
BSE	Back Scattered Electron
EDS	Energy Dispersive X-Ray Spectroscopy
TEM	Transmission Electron Microscopy
STEM	Scanning Transmission Electron Microscopy
DSC	Differential Scanning Calorimetry

Chapter 1

INTRODUCTION

1.1 Background

So many centuries, the theory of alloy systems design has been based on using one or two elements as the base components, and from time to time, an addition of other elements in small amounts are used to improve the properties, such as steels and other intermetallics. In recent year, this concept has been challenged by the theory of high-entropy alloys (HEA) given by Yeh et al [1]. An HEA is defined as an alloy consisting five or more than five principal elements in an equimolar or near equimolar ratio with the concentration from 5 to 35 at.% of every element [1,2]. The effect of high entropy of mixing by multi-component elements will make high entropy effects, lattice distortion, sluggish diffusion and cocktail effect. As a combination of these four effects, HEA can make a simple solid solution structure instead of a complex intermetallic structure. HEA consisting of more than 5 major alloying elements violates the conventional phase rules for the formation of three microstructures: (1) simple solid solution (FCC/BCC/HCP) or a mixture of FCC and BCC, (2) a combination of solid solution and intermediate phase, and (3) amorphous metal glass. The formation of different types of microstructures in HEA leads to some excellent properties such as high specific strength, good thermal stability, high oxidation and corrosion resistance and better wear resistance. Due to these characteristics, HEA has potential applications in marine and structural components [3,4]. Continuous efforts have focused on the empirical correlation of the formation of solid HEA solutions with the understanding of the relationship between atomic size and thermodynamic parameters and structure-property in HEA. In addition, some HEAs have excellent thermal stability and high temperature oxidation resistance.

It has been recommended that so far many investigational HEA studies have focused on the narrow range of alloy compositions (Al, Ti, Cr, Mn, Fe, Co, Ni and Cu are commonly used) to develop new alloys with many different compositions. Maybe only significant refractory metal-based HEAs could be introduced to provide significant phase changes in this regard. Therefore, I

consider one of the most promising potential applications of HEAs is structural materials. It has been suggested that some HEAs have some higher mechanical properties than conventional alloys, which can make them attractive for structural applications. For example, $Al_{0.5}$CrFeCoNiCu [5] has an impressive fatigue resistance and CrFeMnCoNi has excellent strength and toughness at low temperatures [6]. However, it seems clear that many of the HEAs examined so far are too brittle to be used as engineered materials. Although low ductility is certainly not ideal for structural alloys, the same is true for the low yield strength observed in alloys containing simple solid solutions, especially when the conditions of use involve high temperatures. Almost all successful engineering alloys are based on precipitates or enhanced interfaces that serve as a thermal barrier to the dislocation movement. This fact shifts the focus of HEA research from the realization of single-phase microstructures to the development of solid mixed / intermetallic microstructures similar to those found in Ni-based super alloys [7]. In general, good corrosion resistance, toughness and microstructural stability will be required alongside strength. HEA research often adds elements directly to the resulting mechanical properties [8].

Numerous techniques have been used to synthesize HEAs so far such as arc melting, induction melting, solid state processing technique and direct laser fabrication methods [9-11]. Most of the work reported suggests that melting and casting methods are widely used for the synthesis of HEAs. Major advantage of melting and casting method is reduced synthesis time, cost efficient, and energy saving. Although in case of light weight HEAs difference between the melting point of low density elements and other transition elements makes it difficult to synthesize light weight HEAs by this method. Mechanical alloying (MA) is solid state processing techniques which comprises of synthesis of alloy systems from the blend of elemental powders. MA involves repeated cold welding and fracturing of the elemental powders by the impact of balls and vials during milling action resulting in the formation of equilibrium or non-equilibrium phases of alloy. Thus, MA is the only techniques by which alloys can be synthesize even when there is high positive enthalpy of mixing between the individual elements [12]. Further, as milled alloy powders after MA can be consolidated by compaction and sintering operation to form the bulk alloys. There are various techniques for the synthesis of bulk alloys from the as milled powders such as conventional pressure less sintering, hot isostatic pressing, and spark plasma sintering

(SPS). It can be pointed out that SPS is the most cost effective and energy saving consolidation technique compared to all other techniques. SPS comprises of pulsed DC current passing through a powder compact and graphite dies which results in compaction and densification through internal heating in order to approach the theoretical density value. The advantages of SPS include retention of nanostructured materials due to very short heating times, the low pressure required for compaction and better grain to grain contacts.

Based on the indication already existing in the literature to date, it seems to like that the core effects of HEAs related with entropy stabilization, lattice distortion and sluggish diffusion may not be as prominent as initially proposed. Few examples of HEA are considered to be entropy stable solid solutions: both experiments and theories show that adding more components to the alloy can lead to intermetallic formation or phase separation. There have been some recent thoughts about alternative naming conventions, such as the “Compositionally complex alloys " or " complex concentrated alloys’". Still, there is argues that since the terminology of "HEA" is so ingrained in the discourse, changes in the naming convention can only lead to confusion

1.2 Objectives of the Research Work

The demand of high strength, superior corrosion resistant and application in high temperature materials is increasingly becoming a necessary requirement for better energy efficiency in structural and marine applications. Some of the conventional alloys like Al-based and Mg-based have poor mechanical properties compared to steel and also not suitable for high temperature applications. High strength alloys like refractory alloys (base alloy) are not cost effective. The shortcomings and requirements motivated the investigator to undertake the research to synthesize high entropy alloys (HEAs) with to achieve properties such as higher strength to weight ratio, excellent mechanical property such as hardness and superior corrosion resistance similar to stainless steel.

Still there are major complications in designing of high strength HEAs as most of the elements in periodic table possessing high strength and high melting point are having high density and low ductility. Also, most of these elements are immiscible with transition group of elements in periodic table due to their varying atomic radius and high positive enthalpy. Also, many refractory HEAs made of high-melting transient metal elements such as Ta, W, Nb, Mo, and V exhibit high strength and low plasticity. Tungsten is a high melting point and good high

temperature performance, and it has not found much literature when studying its role in HEA. Tungsten (W) is a good metal structural element in the periodic table of all refractory elements (eg. Mo, V, Nb). Therefore, it can be incorporated into HEA to obtain high strength, good corrosion resistance and low cost, and has good mechanical properties and high temperature applications.

For HEAs, their properties may be different from any constituent elements. The type of structure is a major factor in controlling the strength or hardness of the HEA. Structured BCC HEAs generally have high yield strength and limited plasticity, whereas FCC structures HEAs have low yield strength and high plasticity. The BCC + FCC mixture is expected to have balanced mechanical properties such as high strength and good ductility. Recent studies have shown that the microstructure of certain "HEA" can be very complex because they often undergo spinodal decomposition and are ordered, and disordered phases precipitate at lower temperatures. The mechanism for solid solution strengthening in HEAs is very different from traditional alloys. HEAs usually have a high melting point and high yield strengths can usually be kept at very high temperatures.

It is not appropriate to talk about the properties of HEAs in general terms, since their different compositions can deliver very different properties, arguably to an greater extent than that which can be expected across alloys systems like steels. However, it seems clear that many of the HEAs examined so far are too weak to be used as engineered materials. Although low ductility is certainly not ideal for structural alloys, the same is true for the low yield strength observed in alloys containing simple solid solutions, especially when the conditions of use is high temperatures. The idea is to balance the performance of the key - some people think HEA studies tend to focus on the performance of interest, rather than the majority required for the combination of application performance. In general, good corrosion resistance, hardness and microstructure stability is required in addition to its strength. Especially with regard to corrosion resistance, it is expected that HEA can provide potential advantages compared to conventional alloys - even if they are a solid solution. it is also stabilized by entropy effects, it can be added to the solution more protection elements such as Al and Cr , increasing the probability of forming a protective oxide layer. When I consider the huge range of possible HEA alloy compositions, the scale of the challenges that HEA has in the development of structural applications is reached. HEA research often adds elements directly to the resulting mechanical properties.

The above shortcomings and requirements motivated the investigator to undertake the research to synthesize a high strength HEAs. HEAs can have outstanding properties such as higher strength to weight ratio, and better mechanical property such as hardness, creep and compressive strength. Thus, it is scientifically and technologically important to synthesize high strength, superior corrosion resistant and application in high temperature HEAs having simple microstructure with superior properties and cost effectiveness. Hence, the present research work focuses on attempt to synthesize bulk HEA by choosing the structural element according to their application i.e. W (Melting point ~ 3895K, Hardness ~ 2600 HV) along with other alloying elements such as Al for high ductility ($\rho \sim 2.70$ g/cc), Fe (low cost and high strength), Cu (high ductility and thermal conductivity), Cr (high corrosion resistance), Mn (enhance hardenability and wear resistance), for the potential application in high temperature, structural and marine environment. Furthermore, the effect of variation in tungsten content has been studied to establish the materials-structure-properties correlation in case of proposed high entropy alloy system

Lot of research has been going on in the recent days to design new alloy systems with improved properties which could be suitable for different engineering applications. Also, an on-going effort is focused on empirically correlating the phase evolution and thermodynamic parameters of the HEAs and understanding the structure-property relation. Therefore, the present research work focuses on the designing of alloy by introducing varying concentration of tungsten element with the transition elements to synthesize HEA which are higher mechanical properties.

1.3 Outline of the Thesis

- **Chapter 1:** The present research work is split into 8 chapters including an introduction to the high entropy alloys.
- **Chapter 2:** Review of thermodynamic parameters proposed and some previous work on the phase formation, stability, properties of HEAs described.
- **Chapter 3:** The methodology for the alloy preparation, phase characterization and properties has been described.
- **Chapter 4:** Novel AlCuCrFeMnWx (x=0, 0.05, 0.1, 0.5 and 1 mol) HEAs were synthesized by mechanical alloying. The effect of tungsten content on the phase

evolution of HEAs was investigated. Also, phase formation of the present HEAs has been correlated with calculated thermodynamic parameters.

- **Chapter 5:** Spark plasma sintering of as-milled $AlCuCrFeMnW_x$ alloys and the study of phase evolved after sintering was studied. The phase evolved after sintering in these alloys has been considered using thermodynamic parameters and thermal study in discussed in detail.
- **Chapter 6:** Discusses the structure-property relationship has also been proposed by conventional strengthening mechanism and Nanoindentation creep behavior of $AlCuCrFeMnW_x$ high entropy alloys.
- **Chapter 7:** Corrosion behavior of $AlCuCrFeMnW_x$ (x=0, 0.05, 0.1, 0.5 and 1 mol) HEAs in 3.5% NaCl solution are discussed.
- **Chapter 8:** Conclusions and suggestion for future work is given in last chapter.

Chapter 2

LITERATURE REVIEW

2.1 Introduction

Metallurgy plays a pivoted role to civilization of human beings. In the last century, thanks to rapid progress of technology and the enormous demand for the improved materials, new alloys systems such as Al, Mg and Ti based alloy to design to cope with challenging working applications in the power, transport and structural related industries [13]. Moreover, these alloys showed superior mechanical properties than the pure metals and are used in major part of engineering applications even today. Majorly steel, an alloy of iron and carbon has been widely usedfrom ages due to its superior properties like good strength, better oxidation/corrosion resistance, and superior wear resistance. Although first successful synthesis aluminum alloys and magnesium alloys in the 1900s led to bring the concept of energy efficiency in different applications such as transportation, aerospace, etc. In the later years many improved alloy systems like nickel alloys, titanium alloys had been synthesized for high-temperature applications like in turbine, etc.

Although the concept of multi-principle alloys had not been explored in the first half of 20^{th} century [14]. In 1970s Prof. Brain Cantor first thought of multicomponent alloys but he was unable to perform work due to lack of funding. Moreover he was also unable to persuade other people in this field. First work on multicomponent alloys was in 1981 by his undergraduate student. Surprisingly, he found single phase FCC microstructure with excellent mechanical properties in $Fe_{20}Cr_{20}Ni_{20}Mn_{20}Co_{20}$ multicomponent system but this work was not published. Much later his undergraduate student Peter Knight and Isaac Chang repeated the work and found the same result and the results was published in 2004 [13]. Independently Prof. J.W. Yeh also reconnoitered the concept of multicomponent alloys since 1995 [1]. First paper on concept of HEA was printed in Journal of Advanced Engineering Materials in 2004. This paper had reported the development of single phase solid solution in multi-component alloy system and explained the related theory accompanying the solid solution formation. Moreover also used for the first time term HEA to designate multicomponent alloy systems.

In this chapter, I review the previous studies of HEAs. As per findings of this literature review, the achievements of previous findings is summarized the objectives of the research are clarified as well.

2.2 Concept of High Entropy Alloys

2.1 Definition

High-entropy alloys constitute of multi-principal elements (≥ 5) with each element having an atomic percentage of 5 to 35 [15-20]. Some studies suggest the definition must include that HEA must be single-phase solid solution [21] and in others the meaning is broadened to include four component systems. There is no right or wrong answer, and the appropriate approach will depend on the intent of the work being performed. Thus it can be said that there are multiple definition of high entropy alloy based on composition, phase etc. so as to allow researchers to explore the field with flexibility [22].

2.2 Four core effects

Physical metallurgy is a branch of science that specializes in studying the correlation between composition, processing, crystal structure, microstructure, physical and mechanical properties. Fig. 2.1 shows a physical metallurgy scheme where direct correlations can be observed. Composition and synthesis route determine the microstructure, which decides the performance. Composition, processing, and the relationship between crystal structure and microstructure are thermodynamics, dynamics, and deformation theory. The relationship between crystal structure, microstructure, and physical-mechanical properties is the theory of solid state physics and strengthening, fatigue, creep, wear, and so on.

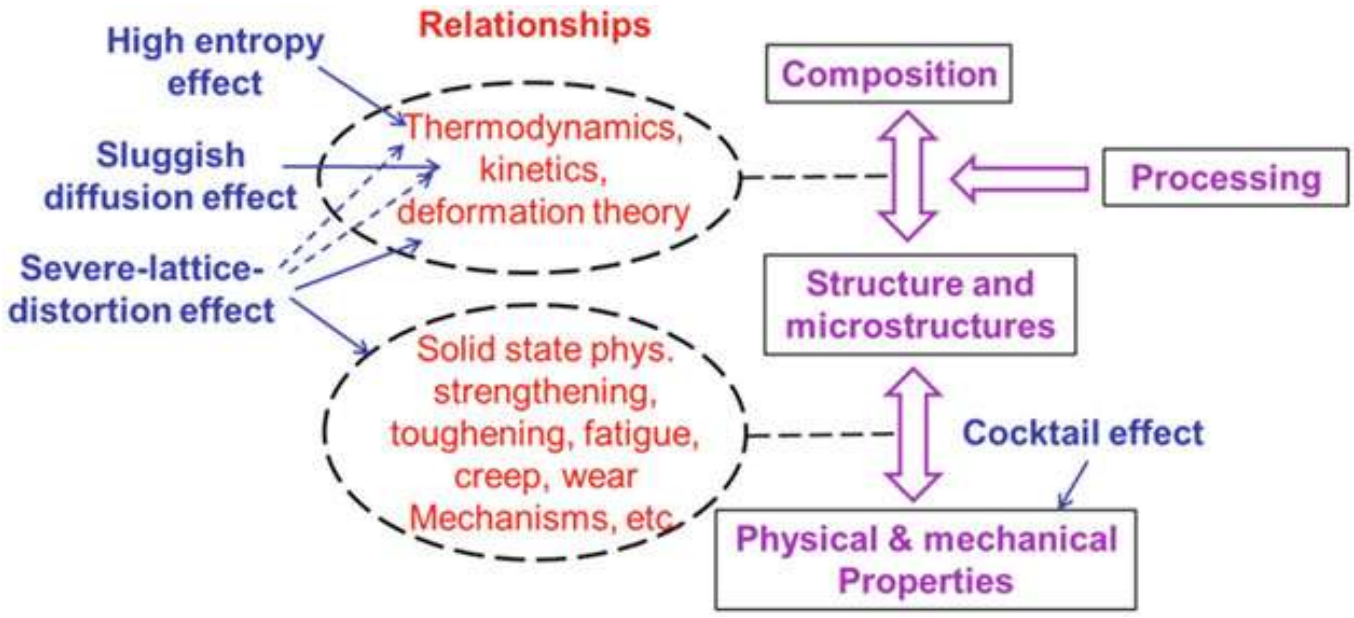

Fig. 2.1: The system of physical metallurgy in which those areas influenced by four core effects of HEAs are indicated [5]

Unlike conventional alloys, HEA compositions are complicated due to the equimolar concentrations of the components. Yeh [23] summarized the four main effects of HEA, namely: (1) thermodynamics: high entropy effect; (2) kinetics: sluggish diffusion; (3) structure: severe distortion of the lattice; and (4) properties: cocktail effect

2.2.1 High-entropy effect

The high entropy effect, tends to steady the high entropy phase, e.g., solid-solution phases, is initially presented given the Yeh [3]. Because it is expected that the intermetallic compounds that they form are relative to those of the equimolar of the isometric alloy composition, they are placed in the middle of phase diagram (for example, the AlCrCo effect of compounds formed in the middle of Al-Cr-Co System) [24]. As per the laws of the Gibbs phase rule, the number of phases (P) of any alloy system at constant pressure under equilibrium conditions is [3]:

$$P = C + 1 - F \qquad (2.1)$$

Where C is the number of components and F is the maximum number of thermodynamic degrees of freedom in the system. In the case of six components alloy system at a certain pressure, one

might suppose a constant response of up to 7 equilibrium levels. However, to my surprise, HEA forms a solid solution phase rather than an intermetallic phase [25-28]. This does not mean that all the multiple components in the same molar ratio will form a solid solution phase in the middle of the phase diagram. In fact, only carefully selected compositions that meet HEA training standards can form solid solutions rather than intermetallic compounds.

According to the traditional physical metallurgy theory, the solid solution stage is also known as terminal solid solution. The solid solution phase is based on an element called solvent and contains other trace elements called solutes. In HEA, it is difficult to differentiate a solvent from a solute because of their equimolar parts. Many researchers have reported simple steps in which several major elements of an alloy can form a single phase of body-centered-cubic (BCC) or face-centered cubic (FCC) solution, and the number of phases formed is well below the Gibbs phase rule, the maximum number of phases [29, 30]. This characteristic also indicates that the high entropy of the alloy tends to inflate the element, which can further confirm the limits of the solution between high entropy effects.

Furthermore, it has been reported that some equimolar compositions slowly cool them from the melt [31] as different phases containing different compositions of AlCoCrCuFeNi, so it is contentious whether they can still be part of as HEA. The empirical rules in supports HEA development are proposed, which includes differences in atomic size and heat of mixing.

Entropy is the thermodynamic properties which deal with the measure of the disorderness of the system given by Eq. 2.2 [1,9,10]

$$S = k \ln W \qquad (2.2)$$

where k = 1.38 X 10^{-23} J/K is Boltzmann's constant and W is the no. of possible microstates in a macroscopic state.

Thermodynamically every alloy system is in an equilibrium state when its Gibbs free energy of mixing ($\Delta G_{mix,}$ Eq. 2.3) is minimum.

$$\Delta G_{mix} = \Delta H_{mix} - T\Delta S_{mix} \qquad (2.3)$$

Eq. 2.3 suggests that the minimization that ΔG_{mix} always depends on enthalpy of mixing (ΔH_{mix}) and entropy of the mixing (ΔS_{mix}). In the case of HEAs ΔS_{mix} becomes large which tends to

reduce ΔG_{mix} which will be more negative making the system more stable. Thus for a random alloy system with N no. ofelements, ΔS_{mix} is given by Eq. 2.4

$$\Delta S_{mix} = -R\sum_i c_i ln c_i \quad (2.4)$$

Were c_i is the molar content of i^{th} element, R (8.31 J/K mol) is the universal gas constant. It is to be noted that here there are only considering the configurational entropies of the system as it is assumed that in random solid solution alloy systems containing N elements the configurational entropy plays a major part for stabilization [1]. Configurational entropy of mixing becomes maximum for equiatomic compositions and is given by Eq. 2.5 [1]:

$$\Delta S_{mix} = R \ln N \quad (2.5)$$

For ternary and quaternary equiatomic alloys systems the configurational mixing of entropy is 1.1R and 1.3R and are sometimes classified as medium entropy alloys [32,33]. It was suggested by Yeh [34] that the system can be only called as high entropy alloy when it's configurational mixing of entropy is equivalent or greater than 1.6R which is shown in Fig. 2.2. However, for a real alloy system other

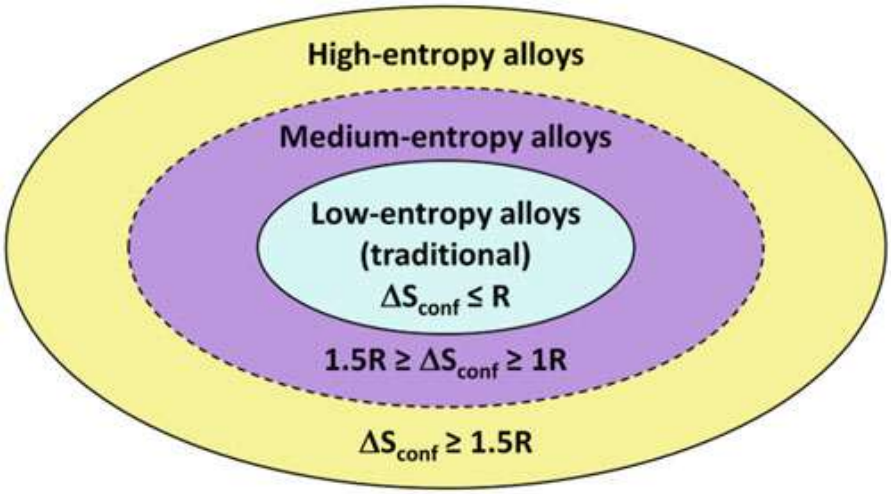

Fig. 2.2: Types of alloys in the alloy world based on configurational entropy

entropy terms like magnetic, electronic and vibrational entropies also plays there part thus making overall entropy much more complicated to explain the phase stabilization in the alloy.

2.2.2 Lattice distortion effect

The multi-element matrix in the HEA solid solution leads to high lattice stress, mainly due to different atomic radii associated with each element. In addition to the difference in atomic size, other factors such as binding energy and crystal structure also make a significant contribution to the distortion of higher lattices. The overall distortion of the HEA lattice is more severe than the conventional alloy system [35]. Figure 2.3 shows the distorted lattice due to the different atomic sizes in the case of HEA.

The severe distortion effect of the lattice is generally compared with the alloy as the main element, where the lattice sites are mainly occupied by the main component. For HEA, if chemical ordering are ignored, each element has the same chance of occupying the lattice position. Because the size of different elements may be very different in some cases, this can cause the lattice to be heavily distorted. The ultra-high strength of BCC HEA confirms this effect [36]. Yeh et al. [37] studied the anomalous reduction of X-ray diffraction intensity (XRD) of a CuNiAlCoCrFeSi alloy system with multi-elements. A series of CuNiAlCoCrFeSi alloys have been studied, systematically added with elements from pure elements to seven elements for quantitative analysis of XRD intensity. The change in the XRD peak intensity of the alloy system is similar to that caused by the thermal effect, but the strength is further reduced beyond the thermal effect by increasing the number of major constituent elements. For the abnormal decrease in the intensity of XRD, the distortion effect of the intrinsic lattice due to the addition of multi-dominant elements having different atomic sizes was added. The mathematical processing used to modify this distortion effect of the XRD structural factor was formulated to be similar to the thermal effect. The greater the roughness of the atomic plane, the lower the XRD intensity of the HEA is than the strength of the monomeric solid.

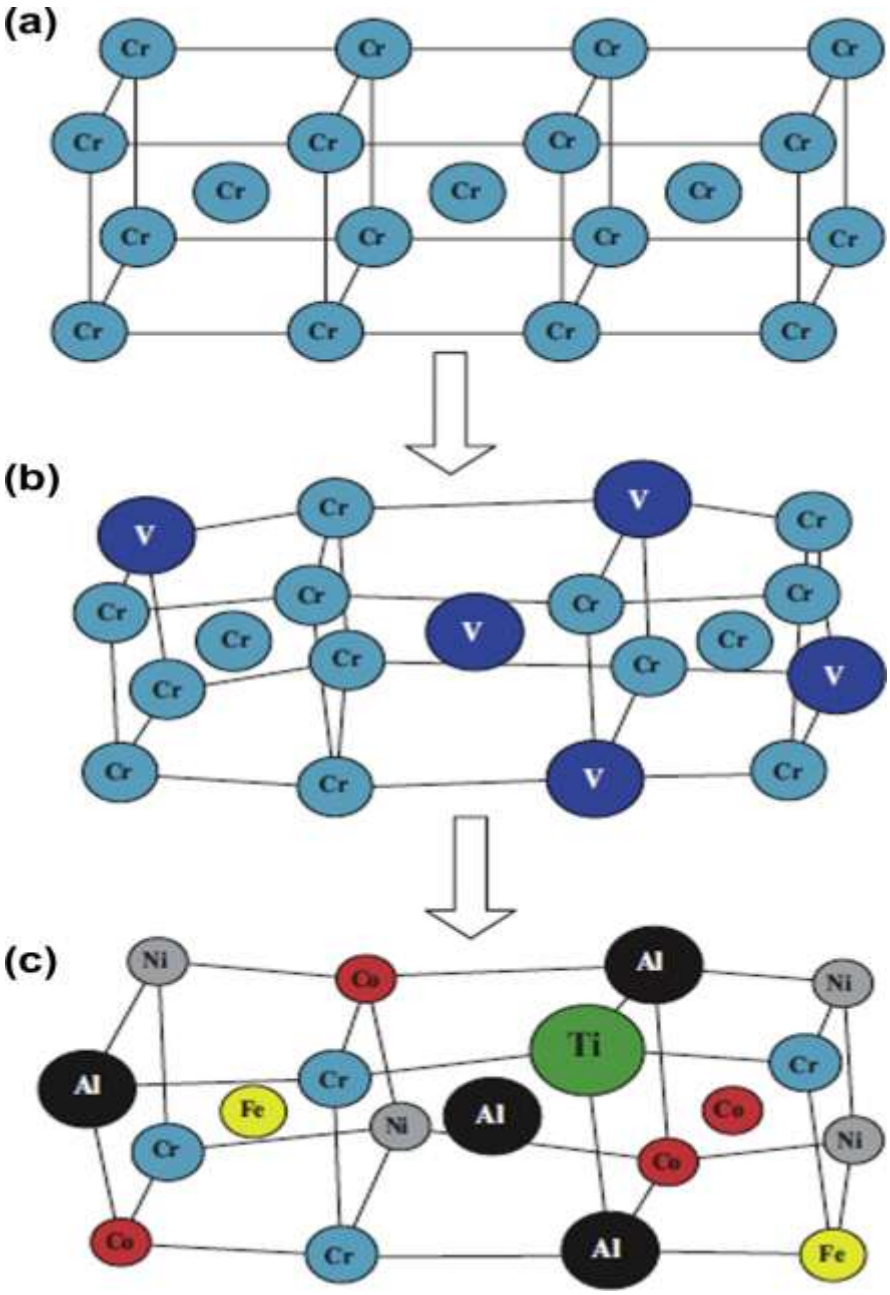

Fig. 2.3: Schematic illustration of BCC crystal structure

The severe distortion of the lattice is also used to explain the high resistance of HEA, especially the HEAs of BCC structures [38-40]. The severe distortion effect of the lattice is also related to the tensile brittleness and the slower kinetics of HEAs [41-42]. However, the many authors also point out that the single-phase HEA of the FCC has a very low intensity [43], which of course cannot be explained by the severe demonstration of lattice distortion. The quantification of HEA lattice distortion requires basic research.

2.2.3 Sluggish diffusion effect

Diffusion kinetics is an important phenomenon in the formation of new phases in any alloy system. It has been proposed that the low diffusion of HEA reduces the diffusion rate of the atoms, which internally slows the phase transition rate in the multi-elements matrix of the phases. The development of a new stage in the old phase needs the cooperative diffusion of many different types of atoms to achieve the division of the composition. Tsai et al. [45] conducted the first study on the diffusion kinetics of CoCrFeMnNi HEAs. The study concluded that the order of decrease in diffusion rate was Mn, Cr, Fe, Co, and Ni. In addition, the diffusion coefficient is lower than pure FCC metal and Fe-Cr-Ni(-Si) alloy.

.

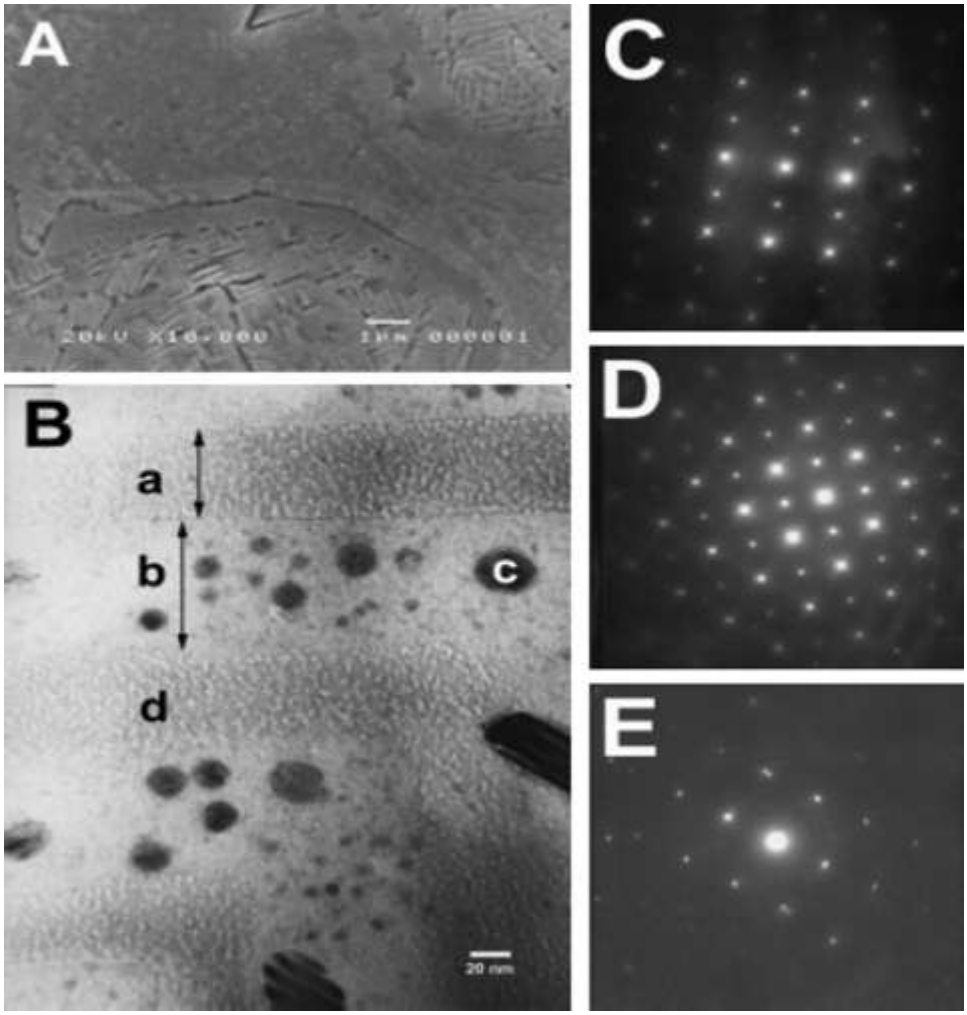

Fig. 2.4: Microstructures of an as-cast CuCoNiCrAlFe alloy. [46] .

The sluggish diffusion effect here is related to conventional alloys rather than the alloys that make up bulk glass. Recently, Yeh [34] studied vacancy formation and composition distribution in HEA and compared diffusion coefficients of elements in pure metals, stainless steel and HEA. The order in which the diffusion rate is found is as follows:

HEA <Stainless Steel <Pure Metal

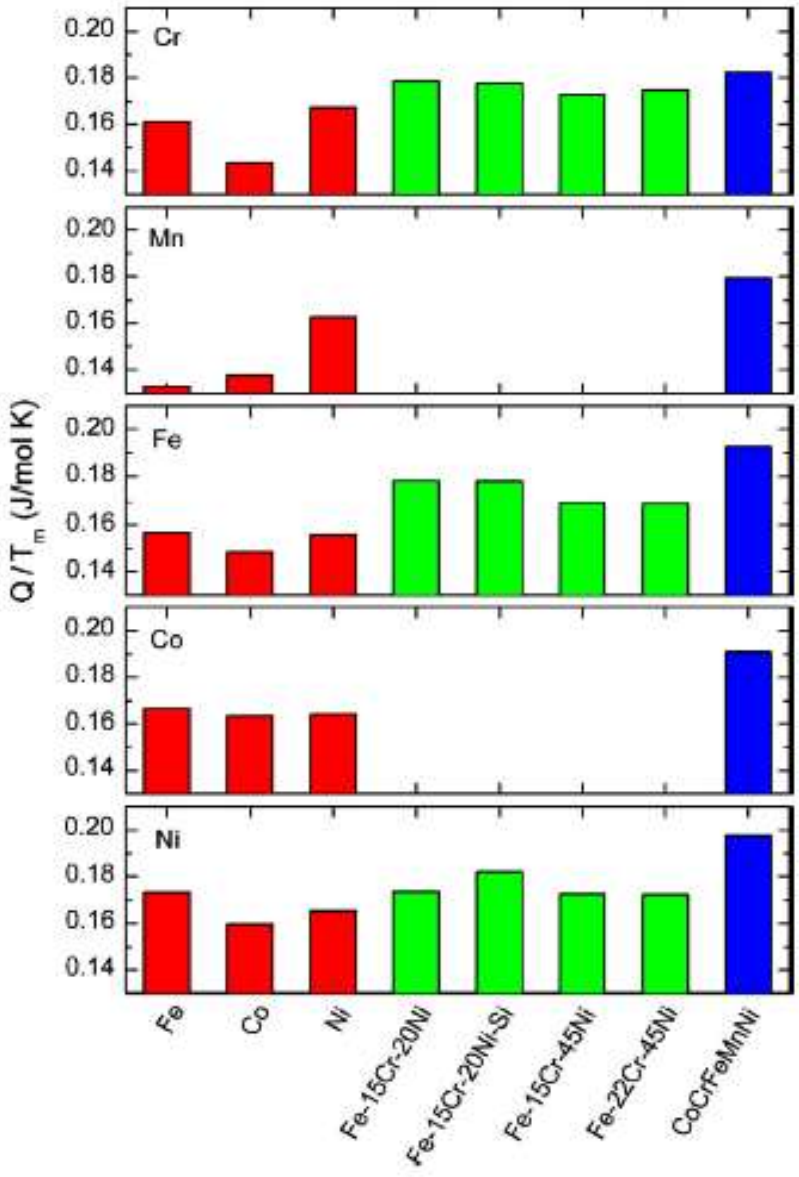

Fig. 2.5: Comparison among the melting point normalized activation energy of diffusion for Cr, Mn, Fe, Co, and Ni in different matrices: pure metals, stainless steels, and high-entropy alloy CoCrFeMnNi [45].

The sluggish diffusion effect is often used to explain the formation of nanoprecipitates because the nuclei are easier to form but slow to grow, as shown in Figure 2.4 for the CuCoNiCrFe as-cast alloy [46]. In the figure, a nanoprecipitate with a diameter of 7-50 nm appears, close to the FCC phase in the spinodal plate, as shown in Figure 2.4B(b). Figure 2.4 also illustrate that the microstructure of some HEAs is likely to be very complex and may consist of nano-precipitates, ordered solid solution phases, disordered solid solution phases and even amorphous phases. This feature is due to the high interaction between the main element and the content of all elements.

However, the Q/Tm normalized activation energy in current HEA is higher for CoCrFeMnNi alloys than other reference standards are shown in Figure 2.5. It has been found that the increase in sluggish diffusion is increased due to many constituent elements in the matrix. Therefore, these results lead to the conclusion that the diffusion effect in HEA is slow. It has also been suggested that there is a slower diffusion rate due to the rich low potential energy lattice (LPE) sites that act as traps and hinder atom diffusion. Therefore, higher LPE fluctuations in HEA result in higher normalized activation energy and lower diffusion rate, which results in sluggish diffusion in HEA.

2.2.4 Cocktail effect

This effect was first given by Prof. Ranganathan [47]. It was suggested that there could be unexpected properties obtained after mixing many elements in an alloy system, which could not be obtained from any independent element. It suggests that alloy can be attuned by finely adjusting the number and composition of the individual elements. The ‘cocktail’ effect allows researchers to remain open for unexpected results that may come due to larger possibilities of the combination of different elements in case of HEAs [22].

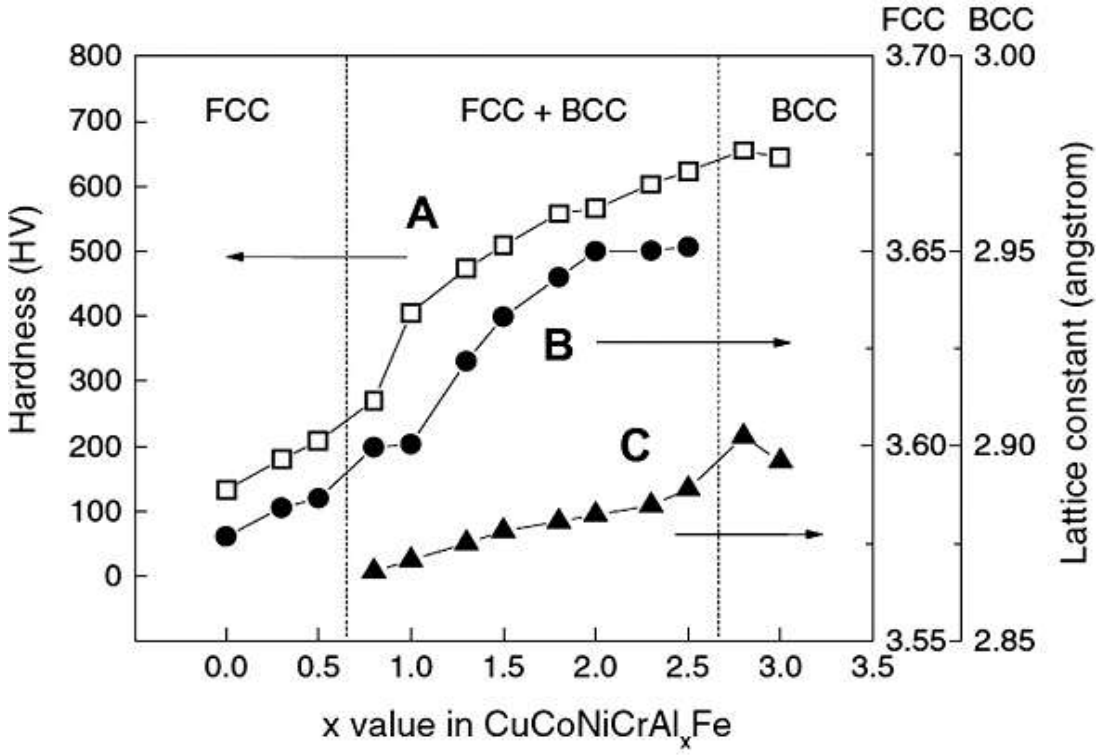

Fig. 2.6: Hardness and lattice constants of a $Al_xFeCuCrCoNi$ alloy system with different x values: (A) hardness of $Al_xFeCuCrCoNi$ alloys, (B) lattice constants of an FCC phase, (C) lattice constants of a BCC phase [48]

The cocktail effect in HEAs can be understood by two examples first, $Al_xFeCuCrCoNi$ [48] HEA prepared by casting route shows variation from complete FCC microstructure at Al content x=0.5 with hardness value 133HV to complete BCC microstructure at Al content x=3 and hardness 653HV, both are described in Fig 2.6

Figure 2.7 relates the specific resistance, which is defined by the yield strength and density of the material and the density between HEA, BMG, conventional alloys, polymers and foams [49]. I can see that the density of HEA is close to that of steel, but it has a higher specific resistance value (yield strength / density). This is partly due to the fact that the HEA, I recently reported is mainly composed of late, high-density transition elements.

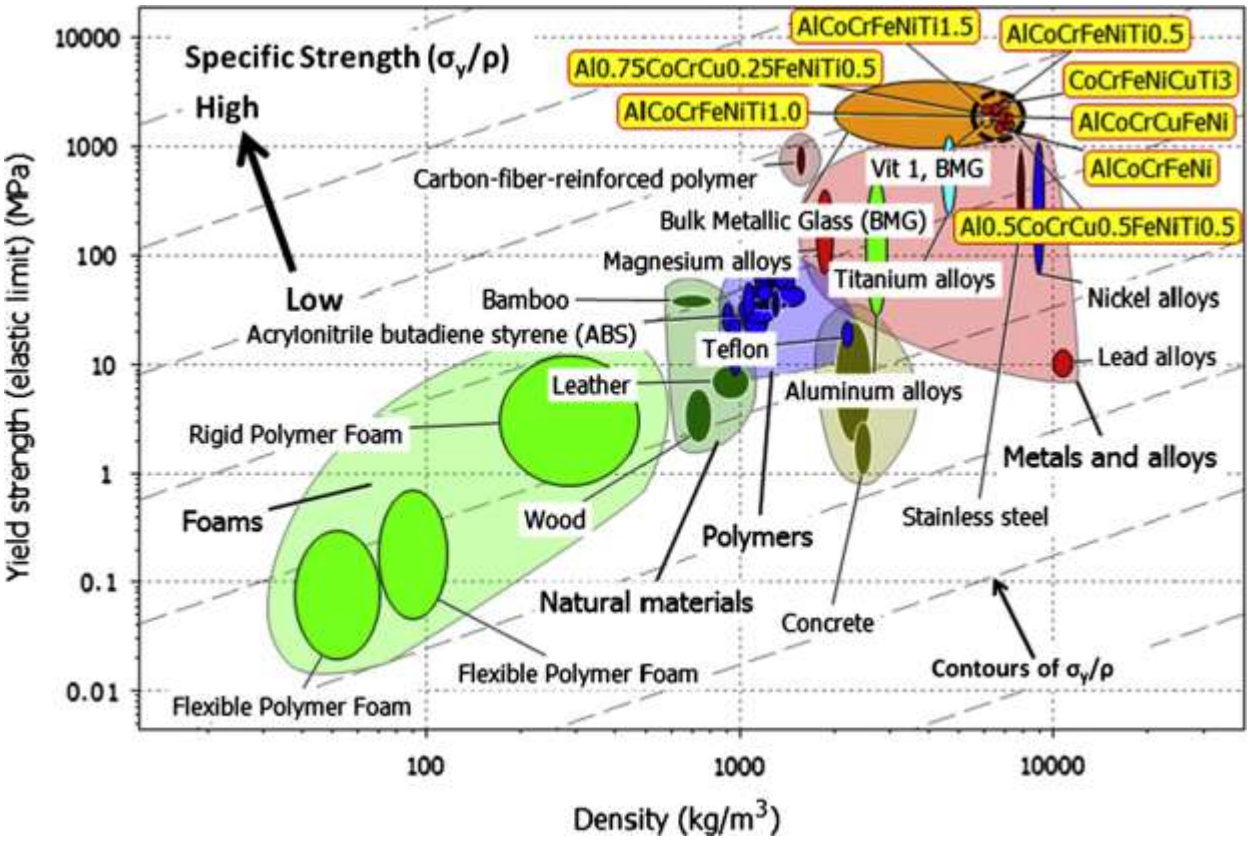

Fig. 2.7: Yield strength, vs. density, HEAs (dark dashed circle) compared with other materials, particularly structural alloys. Grey dashed contours (arrow indication) label the specific strength, from low (right bottom) to high (left top). HEAs are among the materials with highest strength and specific strength [49].

2.3 Thermodynamics for Phase Formation for HEAs

Earlier it was believed that the addition of 5 or more elements in equal composition will lead to the development of intermetallic phase rather than a solid solution due to the different heat of formation and atomic size difference between binary elements. On the other hand, Cantor and Yeh [1,13] have found that some multi component alloy systems forms random solid solution phases which can be explainedon the basis ofthermodynamic parameters between elements supports the formation of solid solution. Development of solid solution in conventional binary alloys follows the condition called as Hume-Rothery rules which are being developed to understand the conditions by which one element is soluble into another. Hume-Rothery rules suggested that the solid solubility majorly depends upon the atomic size, crystal structure, electronegativity and valence.

The Hume Rothery rules are stated as follows:

1. The atomic size of the solute and solvent may not differ more than 15%.
2. The crystal structure of the two elements should be same.
3. Electronegativity of the two elements should be same.
4. Valency of solute and solvent should be same.

In the case of HEAs, earlier studies on the microstructure evolution by J.W. Yeh discussed mainlyatomic size difference, crystal structure, enthalpy of mixing, electronegativity. In addition to these effects Tong et al. [50] concluded that high mixing entropy also leads to the formation of the solid solution rather than the formation of intermetallic compounds. However, Otto et al.[51] studied the effects of entropy and enthalpy on the phase stability in HEAs and suggested that phase evolution in HEAs is associated with a minimization of Gibbs free energy, including both enthalpy and entropy contributions. Further, it was concluded that high configurational entropy might rarely form a single phase solid solution. It was also suggested that highest entropy values are obtained in a single phase solid solution and should be called as real HEAs while alloys that consist of multiple phases can be referred to as multicomponent alloys. Therefore, to design and define the formation of solid solution in HEAs different criterions based on the basic thermodynamic parameter such as mixing enthalpy, atomic size misfit, electronegativity, mixing entropy have been defined. In case of HEAs the mixing of enthalpy (ΔH_{mix}) and atomic radii mismatches (δ) was given by Eq. 2.6 and Eq.2.7 respectively

$$\Delta H_{mix} = \sum_{i=1,i\neq j}^{N} 4\,\Delta H_{AB}^{mix} c_i c_j \tag{2.6}$$

$$\delta = \sqrt{\sum_{i=1}^{N} c_i (1 - r_i/(\sum_{i=1}^{N} c_i r_i))^2} \tag{2.7}$$

where $\Delta H_{AB}^{mix}$is the enthalpy of mixing between binary A and B elements, c_i, c_j are the molar content of i^{th} and j^{th} element, r_i atomic radii of ith component. Zhang et al. [52] predicted that simple solid solution may be formed when -15kJ/mol < ΔH_{mix}< 5kJ/mol, and δ < 5% and a 2D plot in support for the criterion is shown in Fig 2.8.

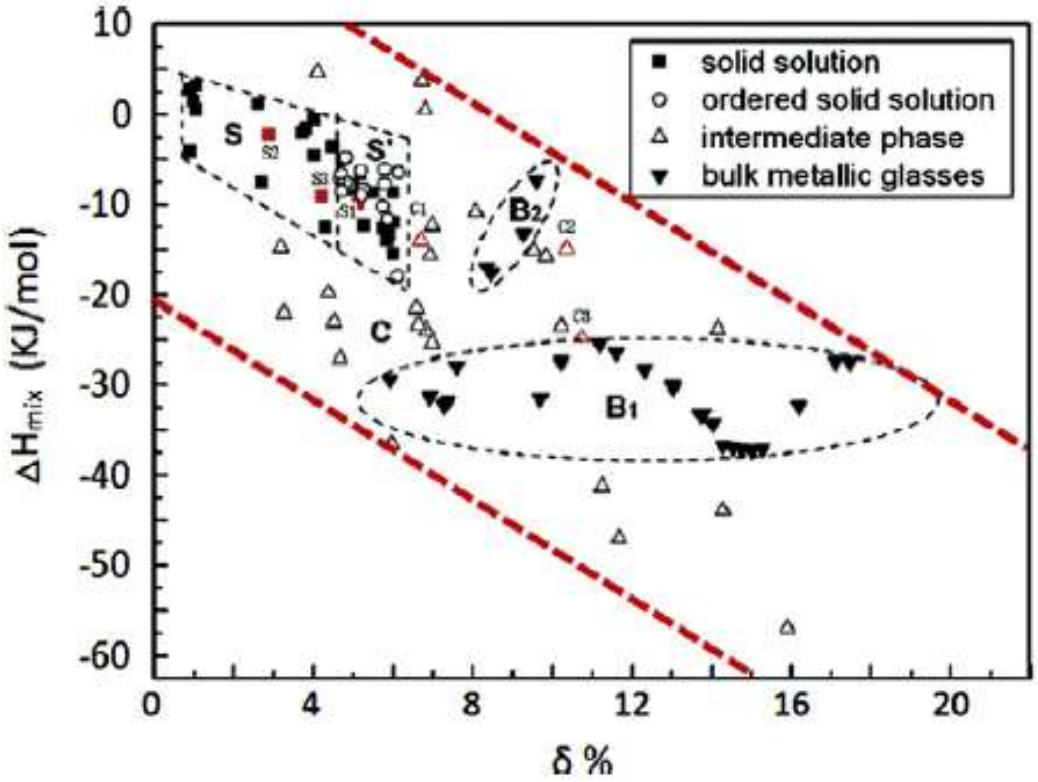

Fig. 2.8: A phase formation map based on the enthalpy of mixing ΔHmix and the atomic size difference δ, for the formation of solid solution, ordered solid solution, intermediate phase and bulk metallic glasses.

Similarly, Guo et al. [53] predicted that formation of simple solid solution microstructure is related to ΔH_{mix}, ΔS_{mix} and δ as $11 \leq \Delta S_{mix} \leq 19.5$ J/Kmol, $-11.6 \leq \Delta H_{mix} \leq 3.2$Kj/mol and $\delta \leq 6.6$. Zhang et al. [54] has also defined the criterion for the formation of simple solid solution in case of HEAs as $\Delta S_{conf} > 13.38$J/K mol, -10kJ/mol $< \Delta H_{mix} <$ 5kJ/mol, and $\delta < 4\%$.

Later other parameters (Ω) for the formation of the solid solution was defined as Eq. 2.8 [55,56]:

$$\Omega = \frac{T_m \Delta S_{mix}}{|\Delta H_{mix}|} \qquad (2.8)$$

Theoretical melting temperature, T_m of an alloy containing N elements is calculated by relation as given in Eq. 2.9:

$$T_m = \sum_{i=1}^{N} c_i (T_m)_i \qquad (2.9)$$

It has been proposed that if $\Omega > 1$, then the contribution of $T\Delta S_{mix}$ will exceed that of ΔH_{mix} and HEAs will form a solid solution and in case when $\Omega < 1$, then ΔH_{mix} will be a predominant part, thus resulting in formation of intermetallic compounds in HEAs system. This relationship has been shown by Yang et al.[55] in 2D maps between Ω and δ in Fig 2.9.

Electronegativity also have an significant role in stabilization of solid solution in HEAs. Electronegativity is a tendency of an atom to attract an electron and according to the Hume-Rothery rules high electronegativity of a solute tends to form intermetallic compounds. In, HEAs the electronegativity difference is calculated by the composition of the HEA and not by lattice type, and is given by Eq. 2.10:

$$\Delta X = \sqrt{\sum_{i=1}^{N} c_i \, (X_i - X_{avg})^2} \qquad (2.10)$$

Where, X_i is the Pauling electronegativity for the ith element and $X_{avg}=\sum_{i=1}^{N} c_i X_i$. The role of electronegativity on the phase stability of HEAs was described by Dong et al. [57] showing that a topologically closed packed (TCP) structure is stable in HEAs where $\Delta X > 0.133$ shown in Fig 2.10.

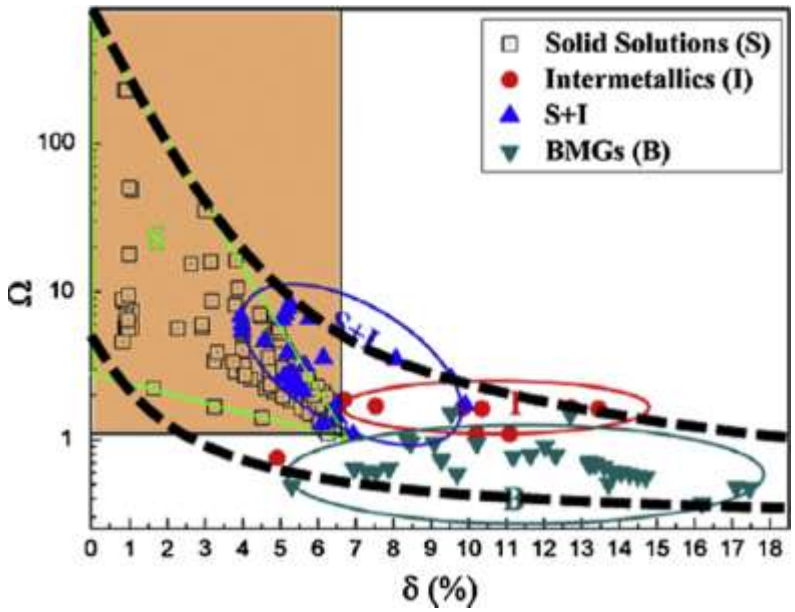

Fig. 2.9: Phase-formation map based on the $\Omega$and δ for the multi-component alloys. For the formation of solid-solutions, $\Omega > 1.1$ and $\delta < 6.6\%$ [55]

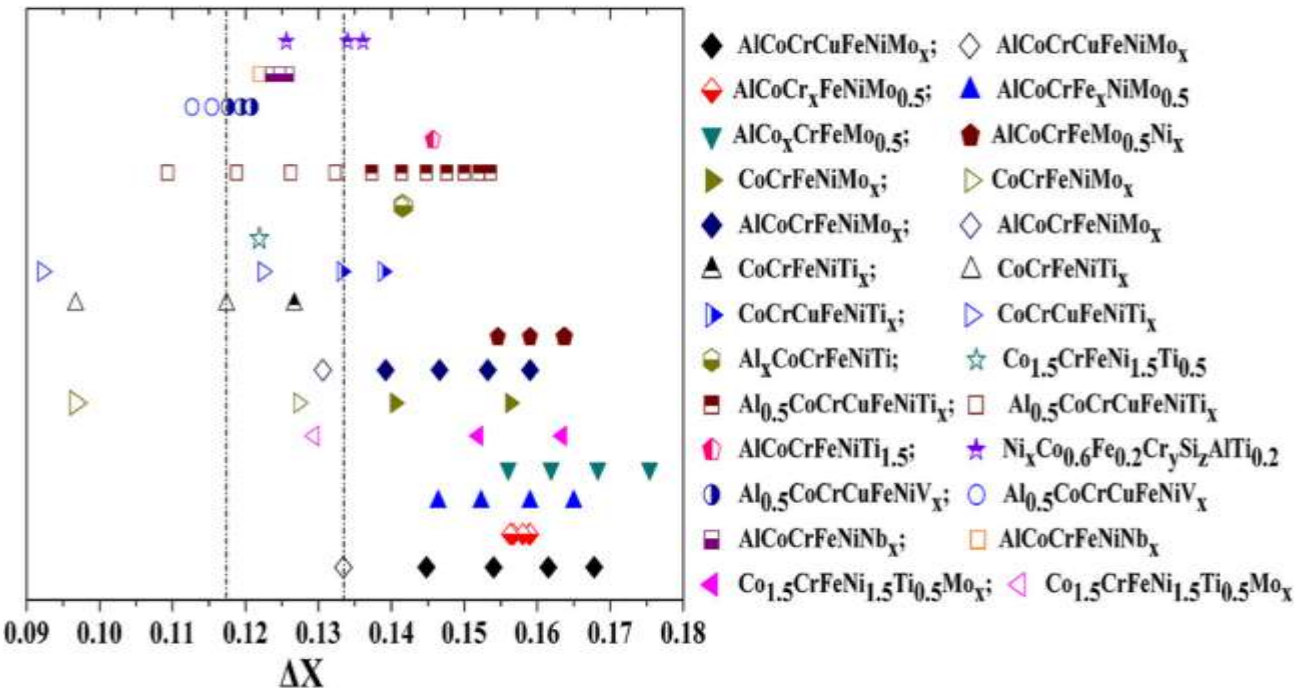

Fig. 2.10: Relationship between the DX and the TCP phase stability for the HEA systems containing Mo, Si, Ti, V, and Nb elements. [57].

Apart from all these models recently, Laurent-Brocq et al. [61] proposed that higher value of configurational entropy is not sufficient to form a simple solid-solution in HEAs. Further, it had been concluded that all the existing thermodynamic models, not well predict the range of formation of a solid-solution. Moreover, it was suggested that the present definition of high entropy alloys is not suitable as it do not give any difference between multi-component alloy i.e. the alloy having the multiphase microstructure and HEAs. Thus, a new definition, based on a structural, physical, chemical or mechanical parameter, is required.

2.4 Processing Routes for HEAs

Several different methods have been adopted for the synthesis of HEAs such as casting route, powder metallurgical route, coating and spraying are shown in Fig.2.11. Mostly all the methods are being discussed in detail in this section.

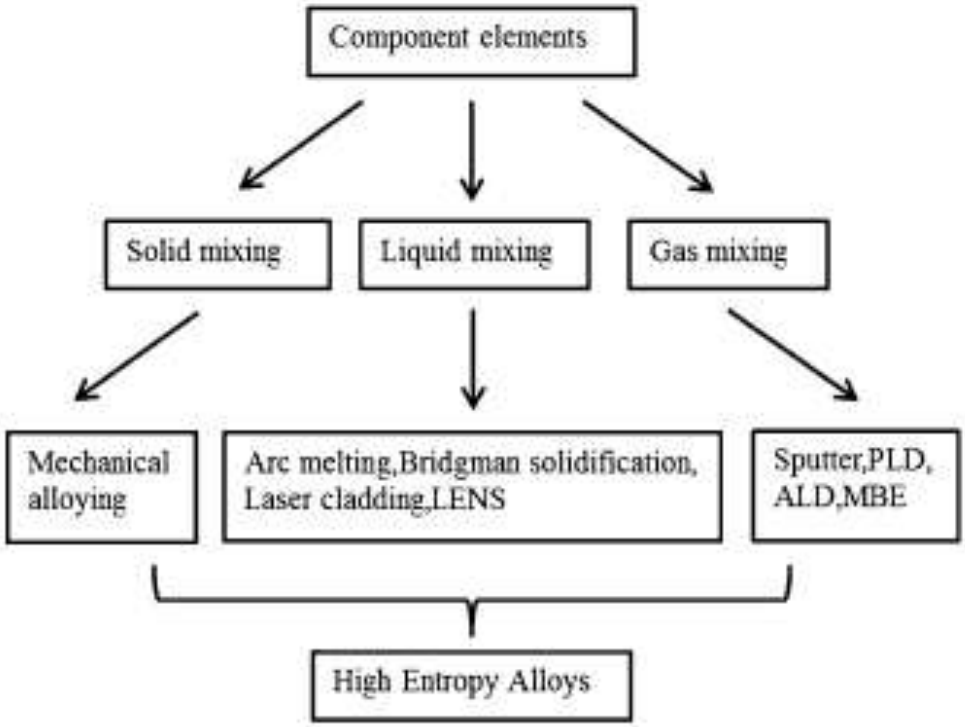

Fig. 2.11: Summary of the fabricating routes for HEAs

2.4.1 Casting route

Melting and casting route has been widely used for the synthesis of conventional alloys and HEAs [16,17,19,20]. Up till now the maximum number of HEAs reported is synthesized by melting and casting route. Melting and casting route has advantages such as reduced synthesis time, cost efficient, and energy saving which gives it an edge over other alloy synthesis techniques. Although the major drawback of this technique is that high temperature leads to the evaporation of low melting point elements like Mg, Zn and Mn which leads to change in the stoichiometry of the alloy during synthesis. Arc melting is most commonly used for the synthesis of HEAs which is illustrated in Fig.2.12. Moreover, the advantage of using an arc melting method is its ability to attain high temperature (~ 3000^{o}C) which enables it to melt most of the elements in periodic table. Basic limitations involved in the synthesis of HEAs through this route is that at low cooling rates typically dendritic and interdendritic microstructures are formed in HEAs due to elemental segregation.

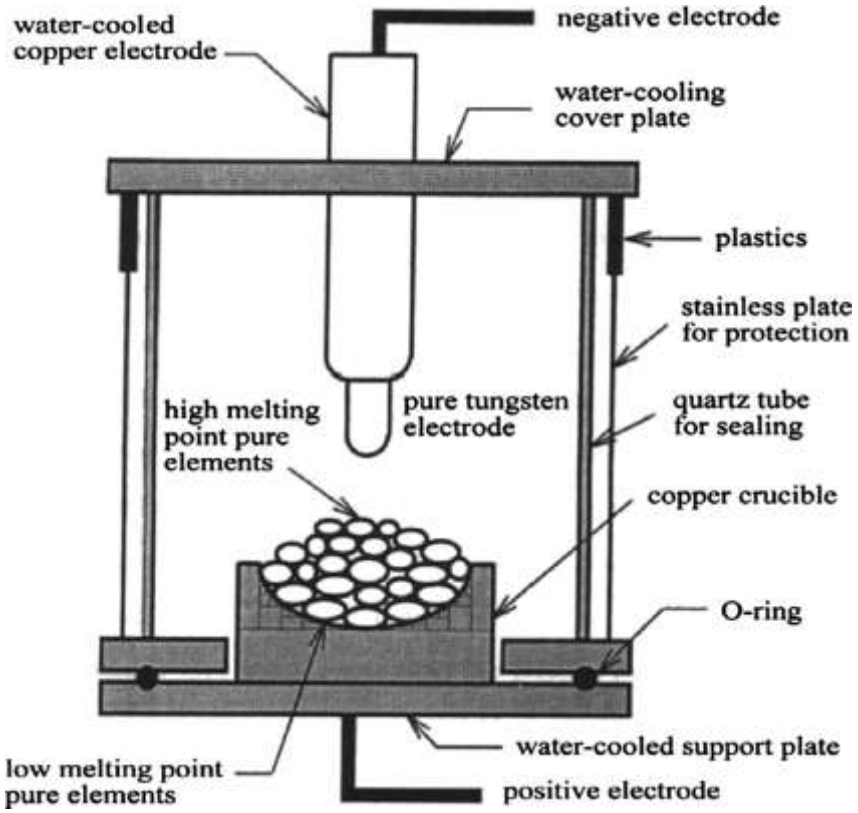

Fig. 2.12: A schematic diagram of the arc melting method [62].

Cui et al. [63] reported AlCoCrFeNi alloys, by Bridgman solidification and results indicate that the microstructure constitutes of the finer dendritic region and decreased the concentration difference between the dendritic and interdendritic regions due to rapid growth rate and high temperature gradients. Ma et al. [64] reported low withdrawal velocity of 5 μm/s to synthesize a single crystal FCC $CoCrFeNiAl_{0.3}$ using a Bridgman solidification technique.

2.4.2 Laser fabrication method

Direct laser fabrication technique is also is used for synthesis of HEA [65-67]. The procedure for synthesis includes two hopper system used to prevent powder segregation. By varying the flow-rate of elemental powder to the melt region the various alloys compositions were manufactured. To reduce oxide formation high purity argon gas was continuously purged in the sealed melt deposition region. Thus, maintaining an atmospheric oxygen concentration of 10ppm or less. The depositions were performed on a 15mm thick stainless steel plate which was locally preheated via laser scanning in the deposition region in order to reduce thermal stress between at interface

of the deposited material and the plate. Joseph et al. [9] synthesized $Al_xCoCrFeNi$ HEAs using direct laser fabrication and the resulting microstructure consists of FCC, BCC+FCC and BCC for $Al_{0.3}CoCrFeNi$, $Al_{0.6}CoCrFeNi$ and $Al_{0.85}CoCrFeNi$ HEAs respectively. Also, the microstructure of $Al_{0.6}CoCrFeNi$ resembles widmanstatten structure which is mainly observed in steels.

2.4.3 Solid state processing route

Mechanical alloying (MA) is a solid state synthesis method that permits synthesis of both miscible and immiscible alloy materials starting from elemental powder blends. MA was first developed in 1966 by John Benjamin and his colleagues at the International Nickel Company (INCO). This process uses a high-energy ball mill to favor plastic deformation required for cold welding and reduce the process times.

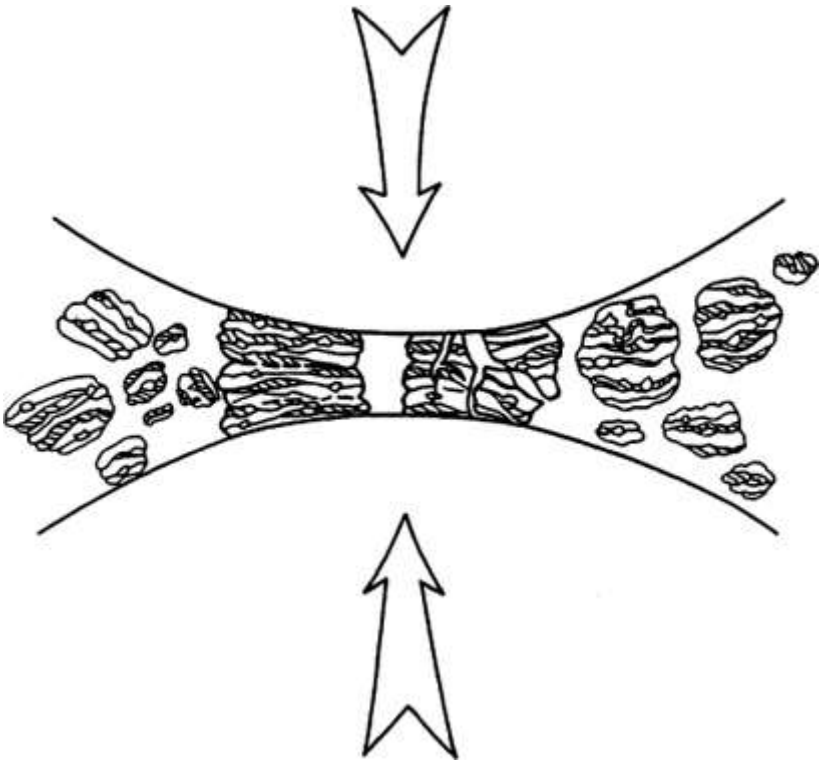

Fig. 2.13: Schematic diagram for mechanical alloying [68].

In the process of ball milling, different elemental powder particles are mixed in a vial containing the ball. The basic mechanism while MA is governed by the cold welded, fractured and again welded during milling action, which is shown in Fig 2.13. Generally, when two balls while milling collide, some elemental powders are stuck between them ,which in turn deforms the

elementparticles leading to cold welding and fracture. In the initial hours of milling, the tendency of cold welding of different particles is predominant due to softer nature of particles. The increase in the milling causes particle deformation, which results in increased work hardening thus increasing the brittleness of powder particle causing it to fracture into smaller flakes leading to a reduction of the particle size [3,4]. Further milling tends inter-layer spacing of different elements to decrease and the number of different elemental layers in a particle to increase. Prolonged hours of milling during MA causes heavy deformation into the particles which in turn increasing various crystal defects such as vacancies, dislocations, and stacking faults. The presence of these defect enhances the diffusivity in such a way that an atom of one element is diffused into the lattice of another.

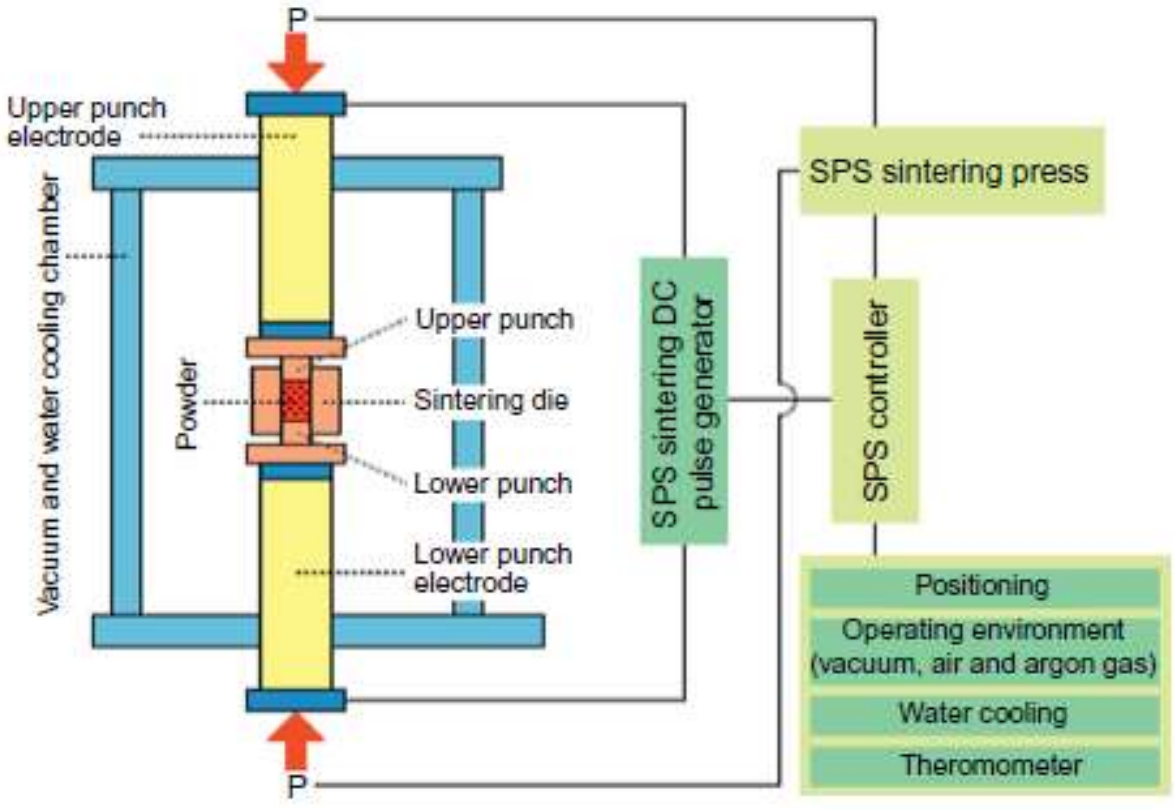

Fig. 2.14: Schematic representation of spark plasma sintering [73].

There are three different combinations of interactions between particles while MA. These are ductile-ductile interaction, ductile-brittle interaction, and brittle-brittle interaction [68]. Also,

MA operation takes place at room or slightly higher temperature and may take prolonged hours of milling for alloying which also causes the refinement of the crystallite size up to the nanometer level. Thus, MA is also the technique which can be used for the synthesis of nanocrystalline materials. Dovelopment of high entropy alloys (HEAs) by MA method was very first published by Varalakshmi et al. [69] and the resulting microstructure consisted of a BCC solid solution.

Compaction and sintering of the as milled powder to produce bulk alloys in solid state processing has mostly been done by conventional method which leads to coarse grains microstructure due to long period of heating. For the synthesis of nanocrystalline microstructure HEAs spark plasma sintering (SPS) technique is generally used for the as-milled alloy powders which is shown in Fig. 2.14.[70,71]. SPS technique was first discovered in 1960 although this technique gained its usage much later after 1990s for the producing bulk alloys [72]. SPS finds applications to synthesize wide variety of the bulk metallic, ceramic and nanostructured materials.

2.4.4 Sputtering

Sputtering techniques are also used for preparation of HEA thin films from the gaseous state. The sputtering is a technique in which thin films are synthesized onto the substrate by atoms from the target is deposited on the substrate by the bombardment of charged gas ions. The sputtering can be divided between DC sputtering, RF sputtering (radio frequency) and magnetron sputtering [74]. Difference between the DC and RF sputtering techniques is that in case of DC sputtering the deposition is mainly governed by the higher values of voltage and argon pressure compared to RF sputtering. As a result the RF sputtering technique is suitable for the deposition of insulating materials. In case of magnetron sputtering, both electric as well as magnetic fields are used to increase the ions path length leading to higher deposition rates (Fig 2.15). Magnetron sputtering is widely used for coating of HEAs. An et al. [75] synthesized a single phase CrCoCuFeNi thin films by RF sputtering route. It was observed that the elements distribution in the thin film much more uniformly distributed.

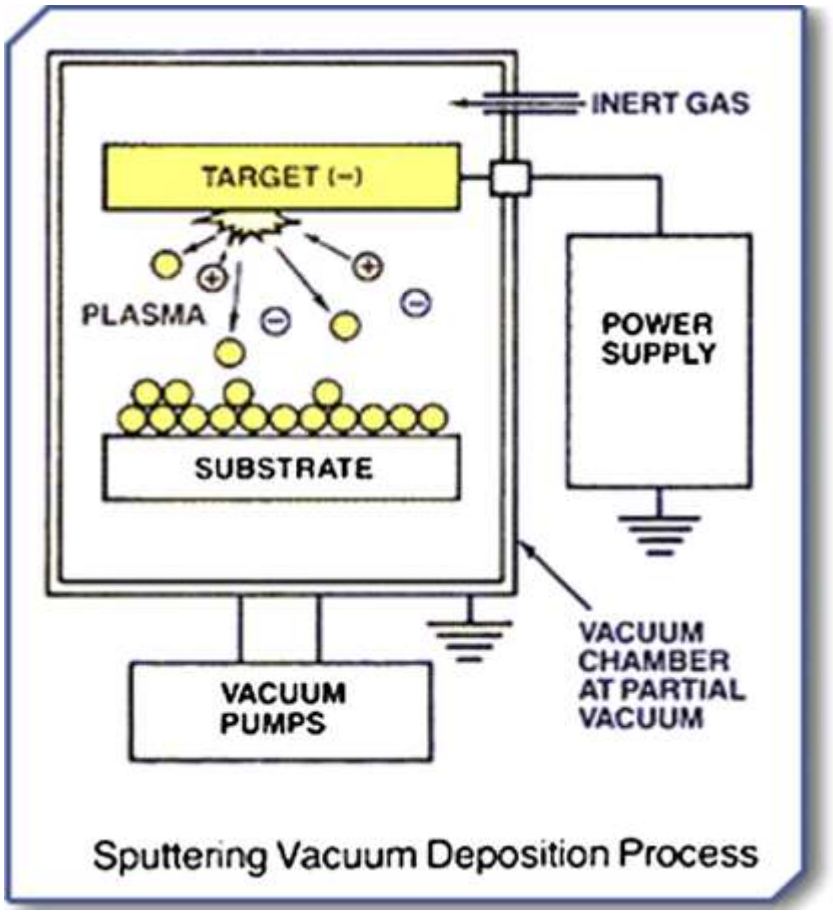

Fig. 2.15: Schematic diagram of sputtering [76].

Other techniques such as plasma spray techniques, thermal spray techniques and plasma nitriding are also some of the efficient methods for the synthesis of HEA coatings on the substrate.

2.5 Current Literature on the Structure-Properties of HEAs

This chapter reviews the microstructure and mechanical properties of high entropy alloys (HEA) in the areas of hardness, compression, stretching, corrosion and nanoindentation. It shows that the hardness of HEA varies greatly from 140 to 900 HV, which strongly depends on the alloy system and the associated processing methods. The hardness at high temperature is also summarized. For the compression test, several material parameters such as Young's modulus, yield strength in compression, elastic deformation and plastic deformation were determined and discussed. A micro-compression experiment was performed on HEA. Nanoindentation studies of initial plasticity and creep behavior are discussed.

In HEAs, different parameters like atomic size effect, enthalpy of mixture and high configurational entropy leads to the formation of simple disordered solid solution. Generally these disordered solid solution phases are having FCC, BCC, or HCP structures leading to some unique properties. Structure and the properties of the HEAs can be varied by changing the content of the elements from equiatomic to near equiatomic compositions. The effect of Al on the microstructure and the properties of $Al_xCoCrFeNi$ alloys have been studied by Yang et al. [76] XRD studies showed that the $Al_{0.1}CoCrFeNi$ alloys (Fig 2.16(a)) show single phase FCC structure.

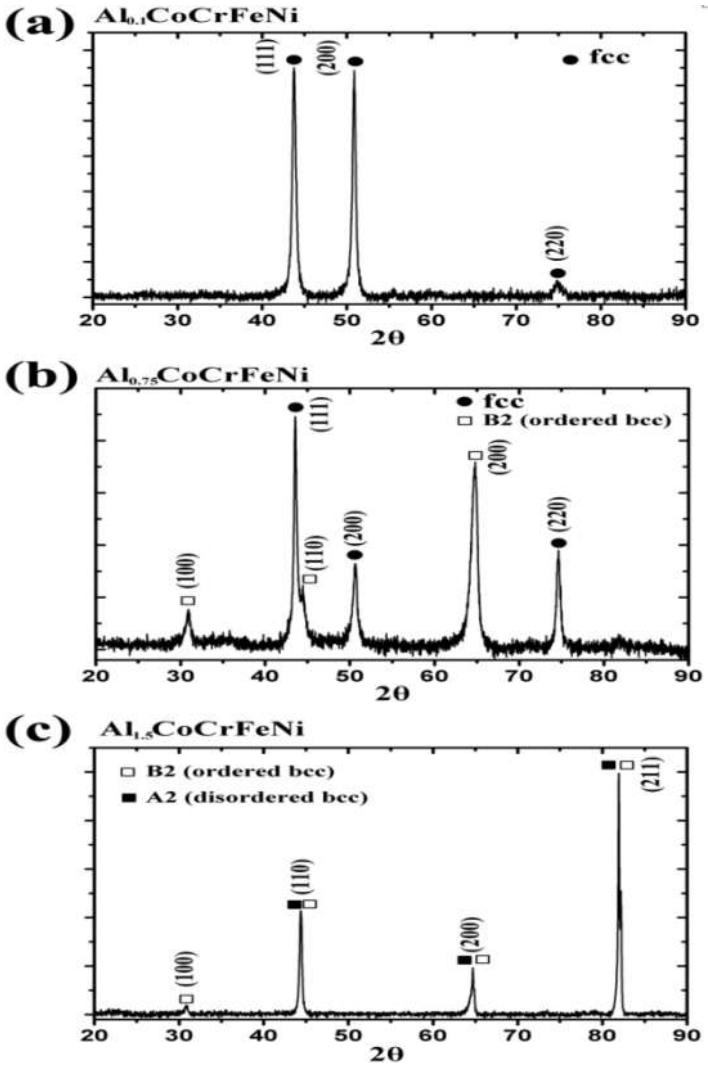

Fig. 2.16: XRD Pattern for $Al_xCoCrFeNi$ (x= 0.1, 0.75 &1.5) [76]

Increase in the Al content upto x=0.75 (Fig 2.16(b)), some fraction of B2 structure also forms along with the FCC phase. Further it was observed that increase in the Al content up to x=1.5, microstructure transforms from the FCC phase (x=0.1 & 0.75) to the BCC phase and ordered B2 structures. The mechanical properties studies on $Al_xCoCrFeNi$ alloys suggested that hardness increases from 1.85 GPa in case of x=0.1 alloy to 5.60 GPa for x=1.5 alloy. This variation in the hardness value was found to be due to the formation of B2 and BCC phases in case of x=1.5 alloy which are having poor ductility in comparison to FCC phase. Thus, structural transformations from FCC to BCC with increasing Al content results in higher hardness.

Heat treatment behavior of equi-atomic AlCoCrFeNi alloy was studied by Munitz et al. [77] Heat treatment of these alloys was performed at different temperatures i.e. 850^{o}C, 975^{o}C, 1100^{o}C and 1200^{o}C in air atmosphere for 3 hrs. An XRD result in Fig 2.17 showed that as-cast alloy consisted majorly of BCC phase with a minor B2 phase. On heat treating these alloys at 850^{o}C, FCC and σ phase is evolved with BCC phase. It was interesting to note that σ phase disappears when the heat treatment was performed at 975^{o}C, 1100^{o}C and rest of the phases like BCC, FCC and B2 mainly constitute the microstructure of the alloy.

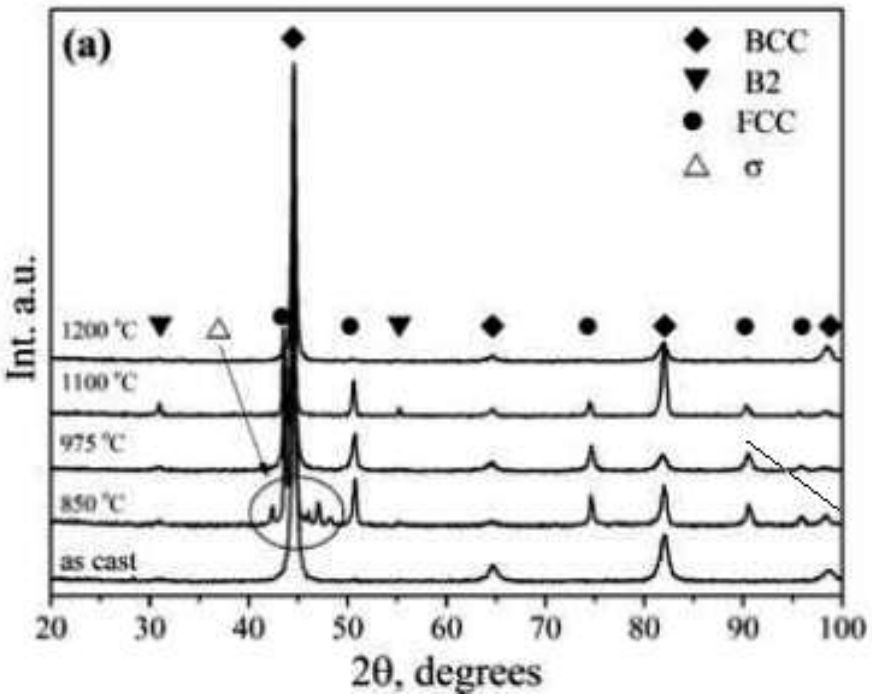

Fig. 2.17: XRD patterns from the AlCoCrFeNi alloy in as-cast condition and after different heat treatments [77]

Heat treatment at 1200^{o}C causes FCC phase to disappear and primarily BCC phase become the major phase with very small fraction of B2 phase. Microstructural studies suggested the AlCoCrFeNi constitute of mainly two types of regions Al rich dendrite core (DC) and Fe and Cr rich inter dendritic (ID) regions.

Zhang et al. [78] have synthesized equi-atomic AlCoCrFeNi alloy using the elemental mixture in SPS. The elemental powder mixture sintered at 1200 °C for 20min under a pressure of 30MPa. The phase evolution studies had shown the formation of FCC, BCC and small fraction of B2 type structures. The micro hardness was found to be 518 HVN. These alloys also possess high strength and ductility which is because of the combination FCC+BCC phase.

Ornov et al. [79] synthesized Novel AlFeCuCrMgx (x = 0, 0.5, 1 &1.7 mol) HEAs by mechanical alloying. XRD analysis indicates the formation major BCC phase with minor FCC fraction in AlFeCuCr and AlFeCuCrMg0.5 HEAs. Although AlFeCuCrMg and AlFeCuCrMg1.7 have two BCC phases i.e. BCC 1 and BCC 2 as confirmed by XRD. Phase fraction of BCC 2 is found out to be 27.45% and 34.06% for AlFeCuCrMg and AlFeCuCrMg1.7 respectively shown in Fig 2.18. Even with a high enthalpy of mixing, the formation of solid solution is being observed due to the combined effect of severe plastic deformation during the mechanical alloying and sluggish diffusion. Moreover, calculated thermodynamical parameters suggest that present HEAs do not follow criterions given for the formation of a single phase solid solution. From the present study, it can also be concluded that the addition of Mg enhances the probability of formation of BCC structure. DTA analysis depicts the thermal stability of AlFeCuCrMgx (x=0, 0.5, 1 & 1.7 mol) HEAs up to 500 °C. The results also suggested that the range of δ parameter to form ordered solid solutions proposed by Zhang et al. [56] can be extended to higher values.

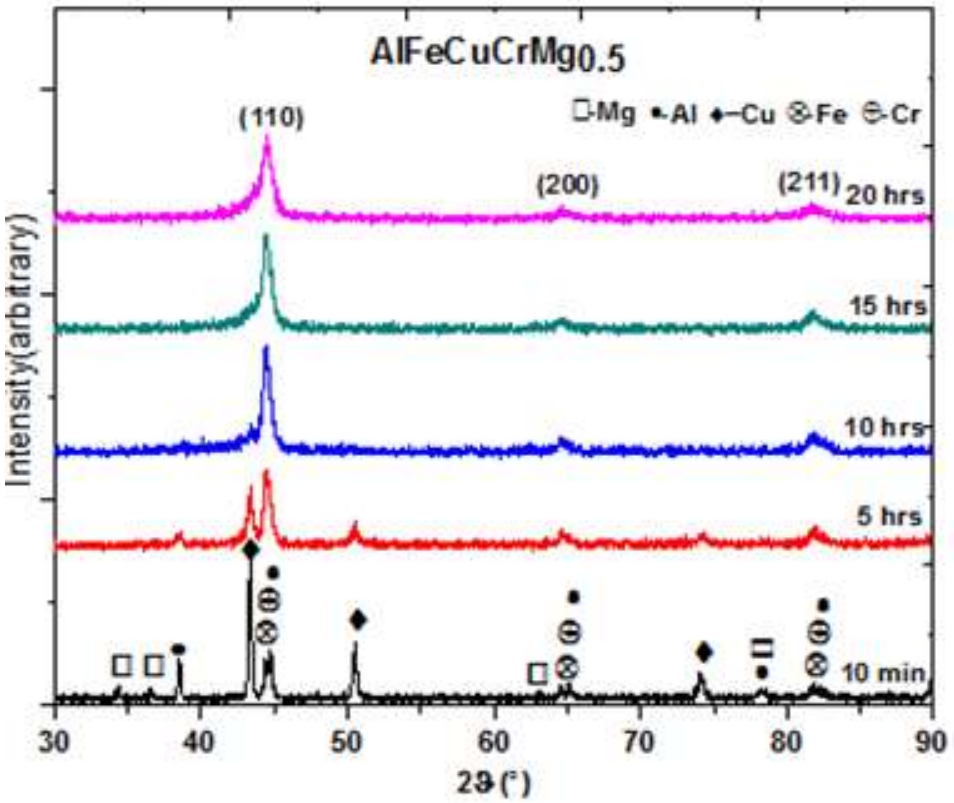

Fig. 2.18: XRD Pattern of as milled AlFeCuCrMg$_{1.7}$ alloys [79]

Further As-milled AlFeCuCr and AlFeCuCrMgx (x = 0.5, 1 & 1.7) has been compacted by spark plasma sintering at 800 ^{o}C and 700 ^{o}C respectively and 50 MPa pressure [80]. The microstructure of bulk sintered AlFeCuCr consisted of two BCC phases and a small quantity of σ-phase are shown in Fig. 2.19. As the Mg content increased from 0.5 to 1.7 mol, the microstructure was composed of predominately AlFe type ordered structure, BCC phase and Cu2Mg laves phase, with metastable Cr rich σ -phase precipitates are described in Fig. 2.20. The formation and growth of Cr rich precipitates in Cu2Mg phase in case of AlFeCuCrMg$_x$ (x = 0.5, 1 & 1.7) HEA is reasoned to be the effect of high positive enthalpy between the binary elements. A peak hardness value has been achieved for the AlFeCuCrMg0.5 HEA due to a combined effect of solid solution hardening, grain boundary hardening and the precipitation hardening. Mg was found to decrease the thermal stability from above 1000 ^{o}C for the AlFeCuCr alloy to 800 ^{o}C for AlFeCuCrMgx (x = 0, 0.5 & 1) and 450 ^{o}C for AlFeCuCrMg1.7.

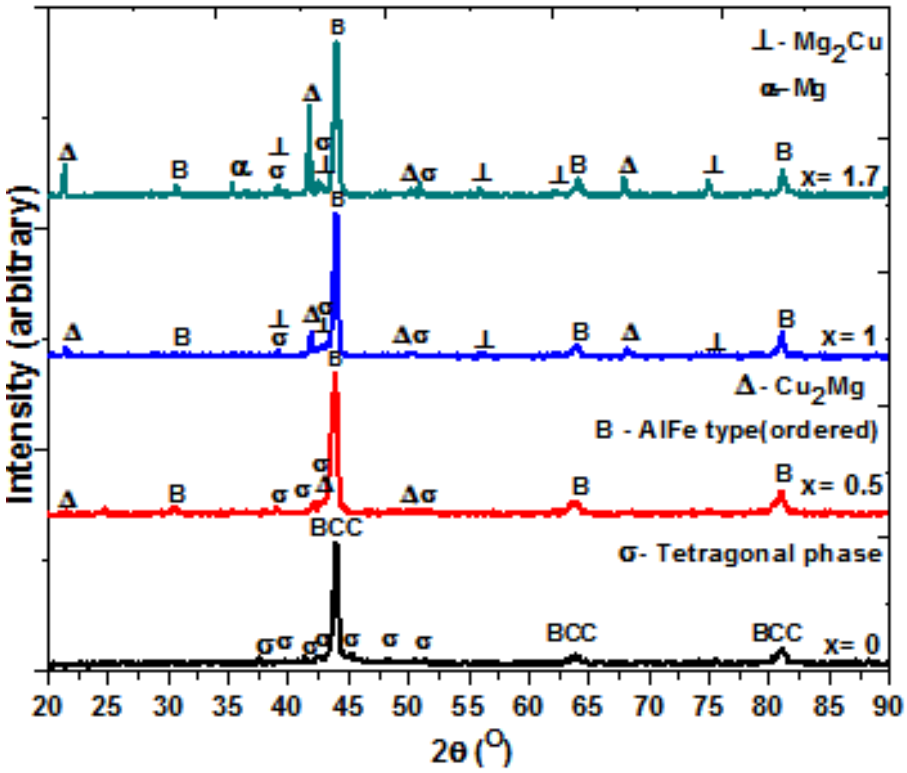

Fig. 2.19: XRD Pattern of spark plasma sintered AlFeCuCrMg$_x$ alloys [80]

It was suggested that the higher value of hardness in these alloys are majorly due to solid solution strengthening and grain size strengthening and the order of the strengthening increases with increase in Al content. The effect of grain size strengthening was consider by the Eq. 2.11

$$\sigma_P = \sum_{i=1}^{5} \sigma_{0,i}\, C_{iP} + \sum_{i=1}^{5} k_i\, C_{iP} d^{-1/2} \qquad (2.11)$$

Where C_i is the composition of ith element in a particular phase, σ_o and k are materials constant for friction stress for dislocation movement and strengthening coefficient respectively, σ_P is the yield strength of a particular phase, and d is the crystallite size.

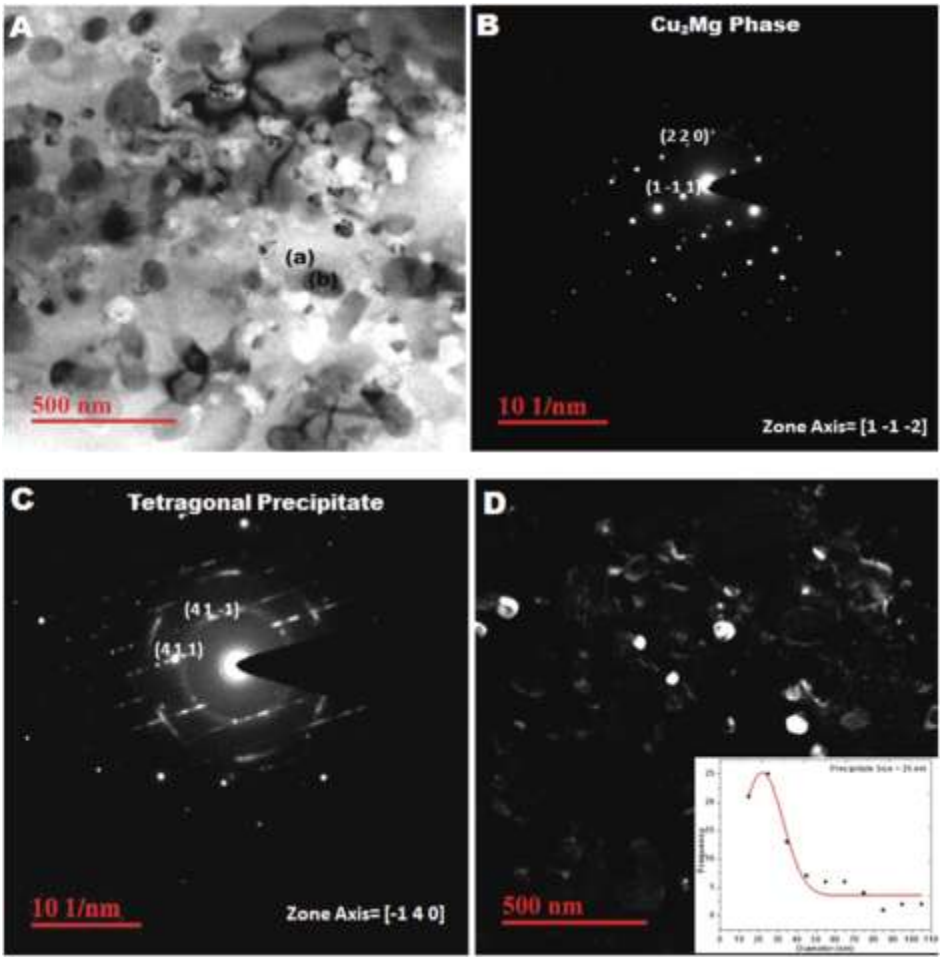

Fig. 2.20: (A) TEM bright field image showing different morphology (B) SAED pattern corresponding to regiona in TEM image (C) SAED pattern corresponding to region b in TEM image , (D) TEM dark field image of SPSed AlFeCuCrMg (x=1) HEA [80].

Studies showed that grain growth at high temperatures in nanocrystalline CoCrFeNi alloys is controlled by mainly three factors i.e. zener pinning effect, long range diffusion of carbide phase, and cooperative diffusion of elements. Micro hardness test was performed on CoCrFeNi alloy was determined to be 570 HVN. Liu et al. [81] synthesized equimolar FeCoCrNi alloy by powder extrusion method. Phase studies show formation of single phase solid solution having a FCC structure peaks with lattice parameter of 359 pm in Fig 2.21. Yield strength of the FeCoCrNi alloy was revealed to be 359MPa. The improvement in the mechanical properties is found to be due to combined effect of solid solution strengthening and grain boundary strengthening.

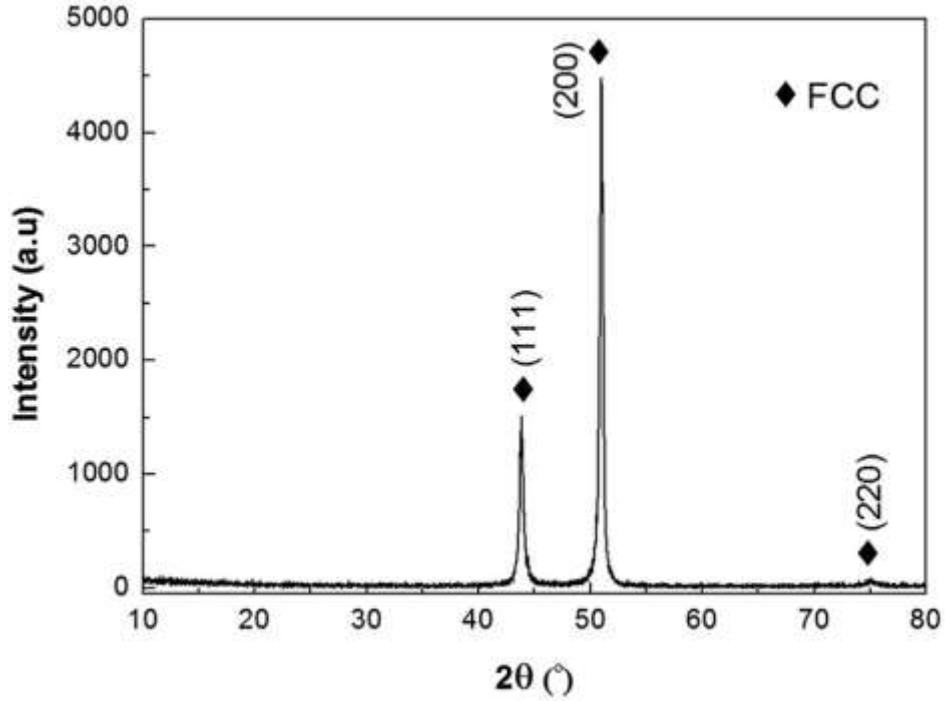

Fig. 2.21: XRD pattern of FeCoCrNi alloy [81].

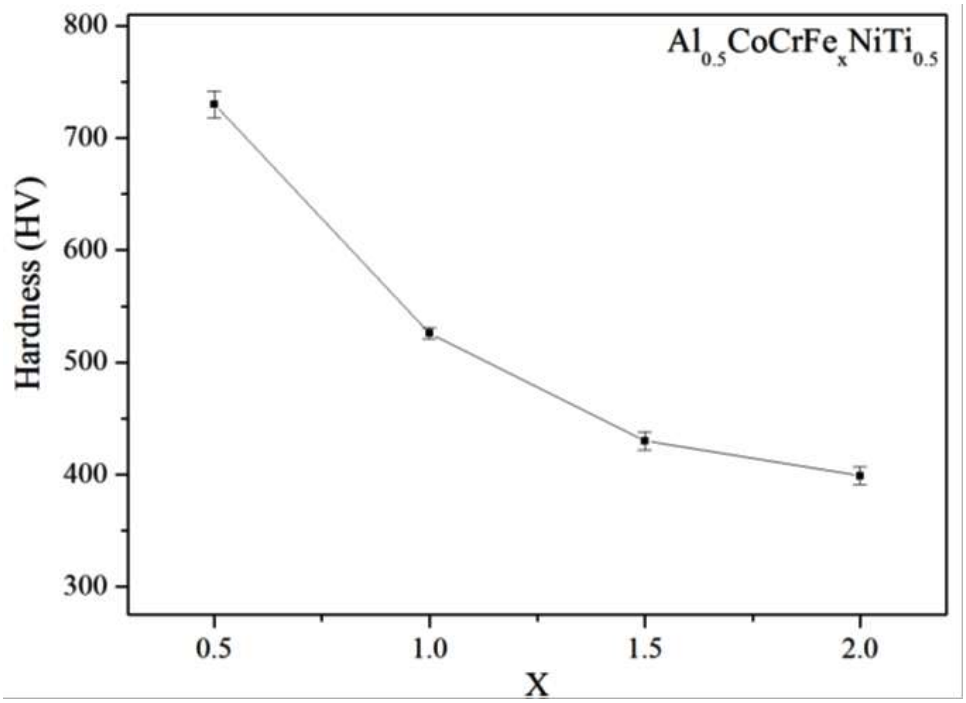

Fig. 2.22: Hardness of $Al_{0.5}CoCrFe_xNiTi_{0.5}$ (x = 0.5, 1.0, 1.5, &2.0) high-entropy alloys [82].

Effect of Fe on near equi atomic $Al_{0.5}CoCrFe_xNiTi_{0.5}$ (x= 0.5, 1, 1.5 & 2) synthesized by vacuum arc melting has been studied [82]. The resulting microstructure for $Al_{0.5}CoCrFe_{0.5}NiTi_{0.5}$ and $Al_{0.5}CoCrFe_1NiTi_{0.5}$ shows the formation of BCC, FCC, σ phase, and ordered BCC phases. For $Al_{0.5}CoCrFe_{1.5}NiTi_{0.5}$ and $Al_{0.5}CoCrFe_2NiTi_{0.5}$ alloys, the microstructure consists of the FCC, BCC, and ordered phases. Fig 2.22 shows the hardness of the $Al_{0.5}CoCrFe_xNiTi_{0.5}$ (x= 0.5, 1, 1.5 & 2) alloys. It was observed that hardness decreases from 748 HVN to 399 HVN with increasing Fe content. It can be suggested from these results that Fe element addition hinders the formation of σ phase and Fe elements act as a FCC stabilizer in case of these alloys.

Effect of Cr addition in $AlCoCr_xFeMo_{0.5}Ni$ (x= 0, 0.5, 1, 1.5 & 2) alloys have been studied by Hsu et al. [83] Phase evolution studies suggested the formation of majorly ordered B2 phase and tetragonal σ phase. It was observed that phase fraction of σ phase increases with the increase in Cr concentration for $AlCoCr_xFeMo_{0.5}Ni$ (x= 0, 0.5, 1, 1.5 & 2) alloys. Further, this σ phase mainly constitutes of multi-element such as Co-Cr, Fe-Cr, Ni-Mo, and Fe-Mo phases. The hardness values showed increase the hardness with the increase in the Cr concentration from 601 HVN (x=0) to 867 HVN (x=2). Thus it can be concluded from the result that Cr concentration enhance the probability for the formation of σ phase in HEAs. Also high Cr content had good softening resistance at elevated temperatures

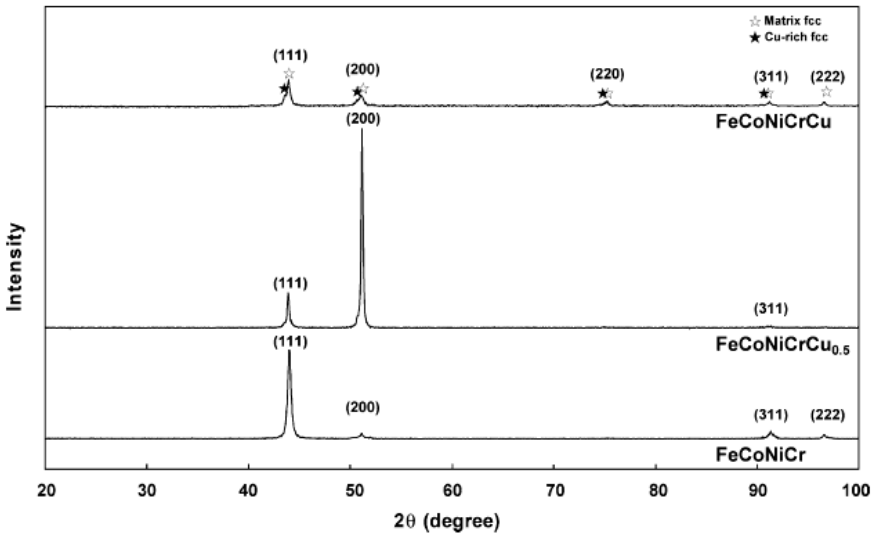

Fig. 2.23: Phase evolution in $FeCoNiCrCu_x$ (x= 0, 0.5 & 1) HEAs [84]

Effect of Cu addition in the FeCoNiCrCu$_x$(x= 0, 0.5 & 1) HEAs had been carried out by Hsu et al. [84]. Phase studies in Fig. 2.23 showed the formation of majorly FCC phase. Although with an increase in the Cu content segregation of Cu rich interdendrites was being observed. The results conclude that the addition of the Cu in the HEAs mostly enhances the Cu segregation in HEAs. Some other studies on the effect of Cu addition have also showed similar results [85].

In addition, L. Tian [86] studied the nano-indentation test using a continuous stiffness measurement technique and deliberate the deformation behavior of the high entropy AlCoCrFeNi alloy at different rates of deformation at room temperature. . The results show that the creep behavior shows a significant dependence on the strain rate, as shown in Figure 2.24. At different strain rates, the modulus of elasticity remains essentially unchanged and because of the size effect of the indentation, the hardness decreases as the depth of the indentation increases. In addition, the modulus and hardness of the AlCoCrFeNi HEA are larger than those of AlxCoCrFeNi (x = 0.3 and 0.5). At a deformation rate of 0.2 s^{-1}, the negative mixed enthalpy and the solids associated with the atomic bond are respectively caused by distortion, caused by the strengthening of the solution.

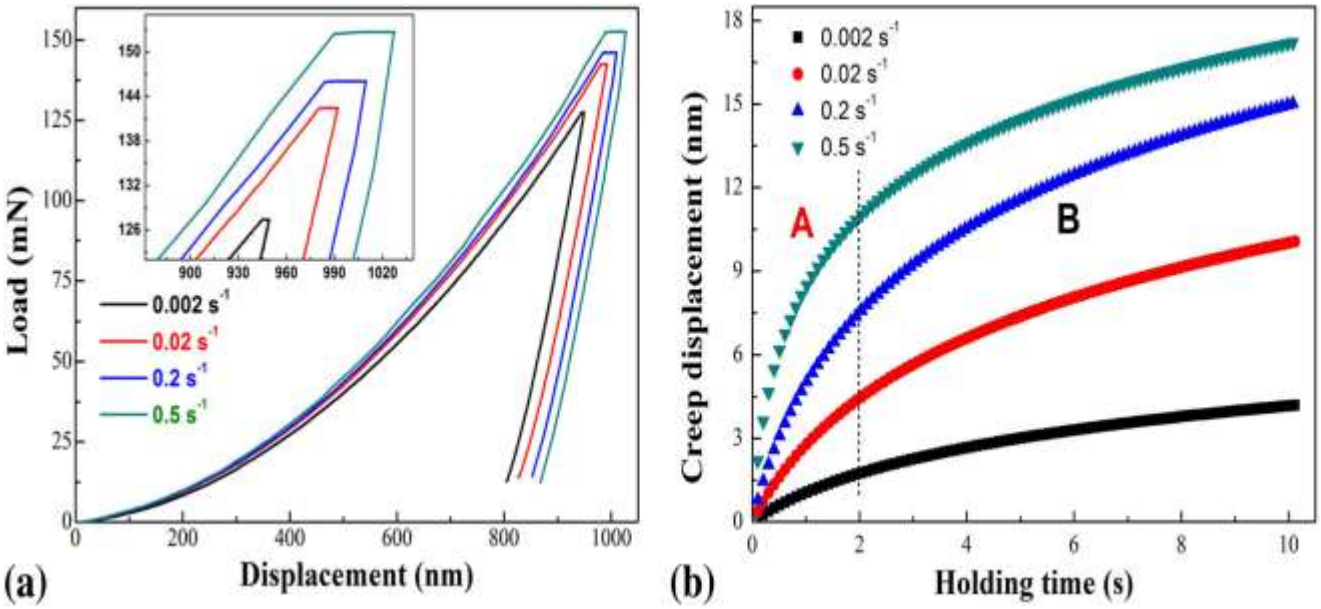

Fig. 2.24: Representative load-displacement curves (a) and creep displacements during the holding stage (10 s) obtained at four different indentation strain rates (b) for the present alloy with a depth limit of 1000 nm. The inset in (a) is the magnified portion at the approximate indentation depth of 900 nm [86]

Table 2.2 summarizes the phase evolved, properties and density of different HEAs synthesized by various methods.

Table 2.2: List of refractory HEAs with processing route, phase evolved and properties

Alloys	**Synthesis Route**	**Phases**	**Hardness (HV/GPa)**	**Yield Strength (GPa)**	**Compressive Strength (GPa)**	**[Ref].**
NbVAlTi	AM	BCC	440 HV		1.2	[87]
NbVZrTiAl	AM	BCC, Laves (C14)	540 HV	1.08	1.21	[87]
$NbVZrTiAl_{1.5}$	AM	BCC, Laves (C14), AlZr2	620 HV	-	1.31	[87]
$HfNbTiVSi_{0.5}$	IM	BCC, Hexagonal silicide	490 HV	-	1.6	[88]
$Al_{0.5}CrNbTi2V_{0.5}$	AM	FCC, hexagonal close packed (hcp) C14 Laves phase.	-	1.2	-	[89]
$AlMo_{0.5}NbTa_{0.5}TiZr$	IM	Disordered BCC, Ordered B2	5.8 GPa	2.1	1.2	[90]
FeCrCoNiV	AM	FCC, Sigma phase	524 HV	0.31	1.6	[91]
FeCrCoNiMnV	AM	FCC, Sigma phase	650 HV	0.32	1.8	[91]
TixWTaVCr	MA+SPS	BCC, TaV2	714 HV	-	2.04	[92]
Ti20Zr20Hf20Nb20V20	IM	BCC, V2M Laves phases	3.8 GPa	-	1.37	[93]
$Co_2MoNi2VW_{0.8}$	AM	FCC, Co7Mo6	667 HV	1.4	2.3	[94]
$NbCrMo_{0.5}Ta_{0.5}TiZr$	AM	BCC1 ,BCC2, FCC	5.2 GPa	-	1.5	[95]
TaNbHfZrTi	AM	BCC	3.8 GPa		0.93	[96]
AlxHfNbTaTiZr	AM	BCC	3.14 GPa		1.42	[97]
AlCrxNbTiV	AM	BCC, C14 Laves phases	-	-	1.7	[98]

$HfMo_{0.5}NbTiV_{0.5}$	IM	BCC, Silicide	403 HV	-	1.26	[99]
$HfMo_{0.5}NbTiV_{0.5}Si_{0.3}$	IM	BCC, Silicide	490 HV	-	1.47	[99]
$HfMo_{0.5}NbTiV_{0.5}Si_{0.5}$	IM	BCC, Silicide	560 HV	-	1.89	[99]
$HfMo_{0.5}NbTiV_{0.5}Si_{0.7}$	IM	BCC, Silicide	603 HV		2.13	[99]
AlNbTiV	Casting	BCC	448 HV	1.02	1.318	[100]
$CrFeNiV_{0.5}W_{0.25}$	Casting	One major and two minor phase	226 HV	-	1.11	[101]
$CrFeNiV_{0.5}W_{0.50}$	AM	BCC, FCC, Sigma phase	279 HV	-	1.30	[101]
$CrFeNiV_{0.5}W_{0.75}$	AM	BCC, FCC, Sigma phase	290 HV	-	1.59	[101]
$CrFeNiV_{0.5}W$	AM	BCC, FCC, Sigma phase	350 HV	-	2.24	[101]

AM-Arc Melting, IM-Induction Melting, MA-Mechanical Alloying, SPS- Spark Plasma Sintering

Hsu et al. [102] studied corrosion behavior of FeCoNiCrCux (x = 0,0.5,1) using immersion and potentiodynamic polarization tests and found that increasing content of Cu in the HEA caused increasing corrosion rates in 3.5 wt% NaCl solution. While FeCoCrNi HEA demonstrated superior general and localized corrosion resistance compared with SS304, they deteriorated in Cu containing HEAs are shown in Fig.2.25.

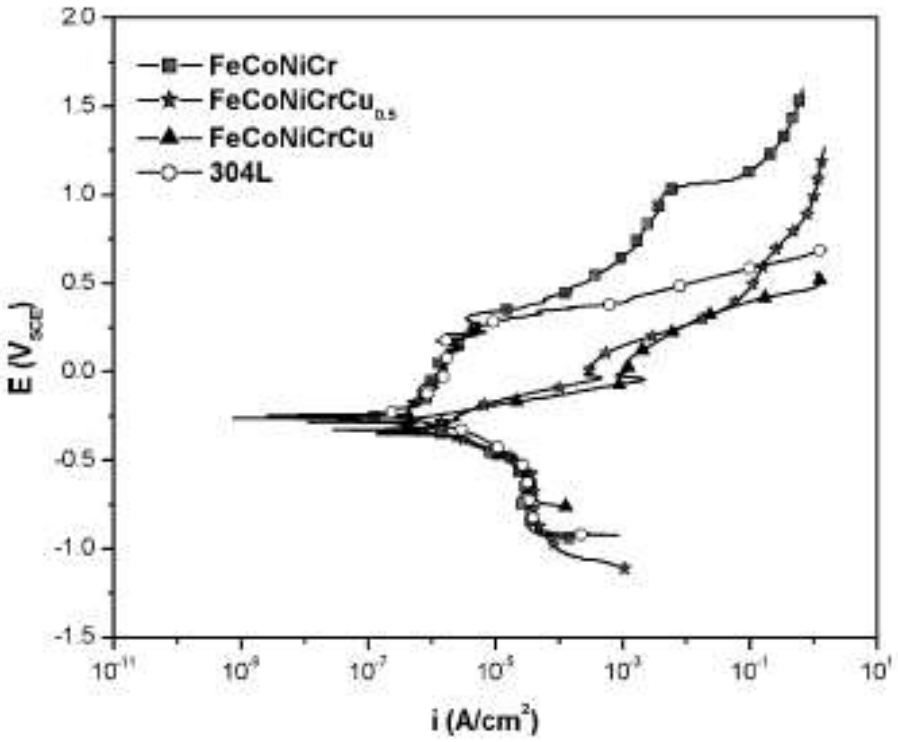

Fig. 2.25: Polarization curves for as-cast FeCoNiCrCu*x* alloys and 304L in 3.5% NaCl solution at 25 ◦C [102].

Thus the literature review concludes that the HEAs are the promising new age material with exceptional properties and can be the potential candidate for different applications. Earlier it was supposed that the simple solid solution microstructure in the HEAs is generally due to the high configurational entropy. But recent work has shown that it is the enthalpy of mixing and atomic size mismatch rather than configurational entropy which decides the formation of simple microstructure. The matter of fact is that there is no single definition has been decided by scientific community on HEA rather the definitions provided in the literature is mostly based on composition and microstructure that gives scientists the flexibility to work. Also, a large number of HEAs were synthesized by different methods including arc melting, spark plasma sintering and direct laser fabrication methods which have shown a simple solid solution microstructure and remarkable properties. High strength HEAs is one of the most promising areas of research in structural application. High strength HEAs were synthesized using the elements like W, V and Cr. The effect of element like Al has been widely studied and the microstructure varies from solid solution to solid solution plus intermetallic. Some previous studies on the effect of Ti in HEAs have also studied showing a multiphase micro structure. But the effect of varying

concentration of refractory element on HEAs has not been studied carefully to understand the phase evolution and phase transformation at different temperatures. Moreover the hardness, Creep and compressive properties in W containing HEAs have not been studied in detail so far and structure–property correlation has not been established yet. Furthermore, the effect of tungsten on corrosion is also very much essential to study to establish materials-structure-process-properties correlation of HEAs.

Thus, it is scientifically and technologically important to synthesize high strength, superior corrosion resistant and application in high temperature HEAs having simple microstructure with superior properties and cost effectiveness. Hence, the present research work focuses on attempt to synthesize bulk HEA by choosing the structural element according to their application i.e. W (Melting point ~ 3895K, Hardness ~ 2600 HV) along with other alloying elements such as Al for high ductility ($\rho \sim 2.70$ g/cc), Fe (low cost and high strength), Cu (high ductility and thermal conductivity), Cr (high corrosion resistance), Mn (enhance hardenability and wear resistance), for the potential application in high temperature and marine environment. Furthermore, the effect of variation in W content has been studied to establish the materials-structure-process–properties correlation in case of proposed high entropy alloy system. The composition of tungsten is selected on the basis of compositional definition of HEAs i.e. the constituent elements should be between 5 at. % to 35 at. %.

The **main objectives of research work can be outlined as follows:**

- To design and develop of appropriate HEA via Mechanical Alloying.
- To compare the variation in the properties of the powder compact with Spark plasma sintering.
- To understand the importance of thermodynamical parameters for the phase formation.
- Material-structure-property correlation study of proposed HEA.

In order to achieve the goal, following methodology have been adopted which is shown in Fig. 2.26. Next Chapter will discuss about the materials and experimental details to fulfill the methodology discussed in Fig. 2.26.

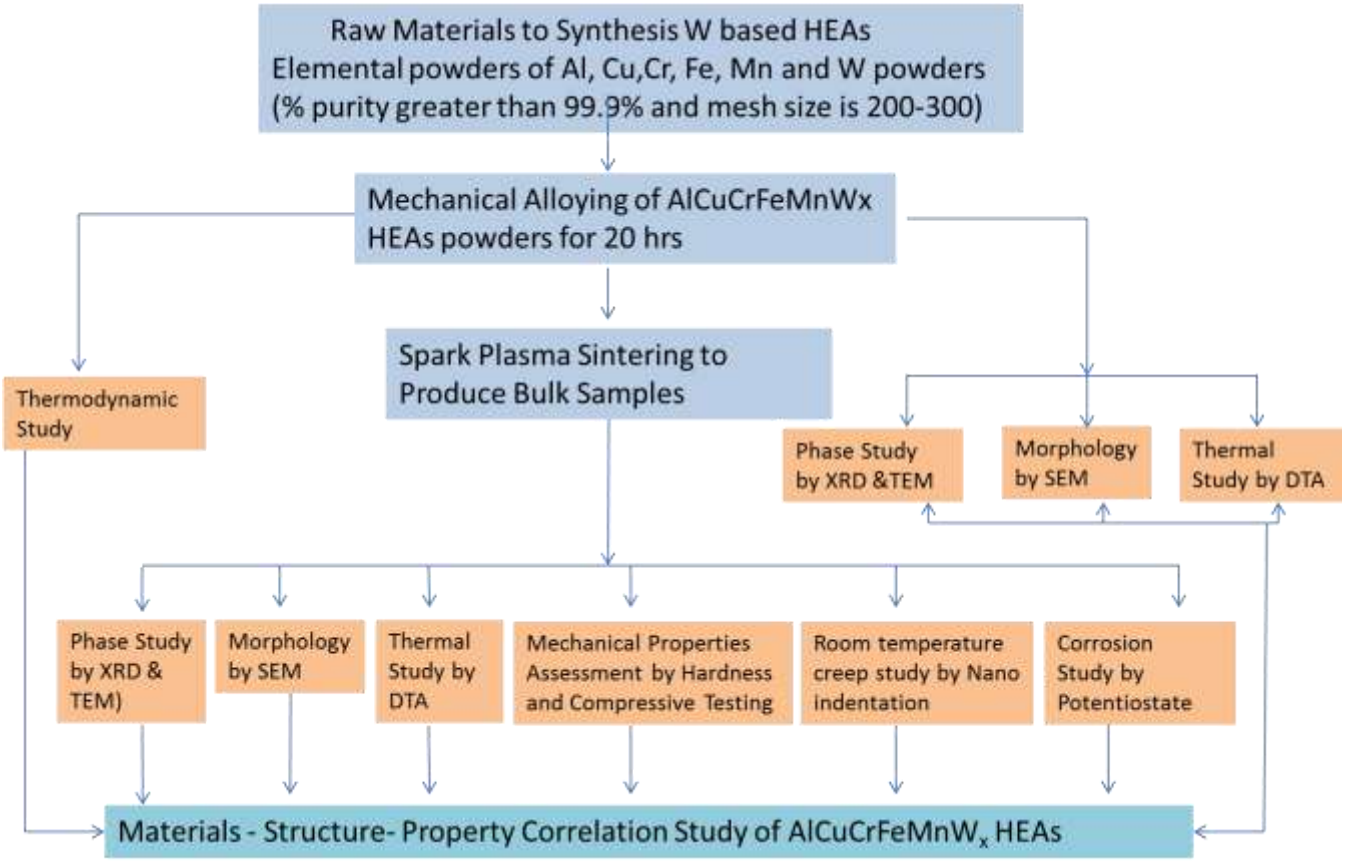

Fig. 2.26: Flow diagram showing methodology for development and characterization of W containing HEAs

Chapter 3

MATERIALS AND METHODS

This chapter discusses about the materials and methods implemented for the preparation HEAs.

3.1 Materials Preparation

3.1.1 Preparation of $AlCuCrFeMnW_x$ (x= 0, 0.05, 0.1, 0.5 and 1 mol) HEA powders

Elemental high purity powders of Al, Fe, Cu, Cr, Mn and W of purity greater than 99.9% and mesh size of 200-300 were mechanically alloyed using Pulverisette-P7 high energy planetary ball mill (Fritsch, Germany) using a vial and balls of tungsten carbide. Ball to powder weight ratio was maintained to be around 10:1. Toluene is used as a process controlling agent (PCA) to prevent excessive cold welding on the surface of the ball and vial and also provide reducing media during the milling. The milling was carried out up to 20 hours in a planetary ball mill at 300 rpm. The as-milled powders were collected after 10 min and then after every 5 hours of milling to study the phase evolution, and dissolution sequence of each element with respect to the milling time.

3.1.2 Spark plasma sintering of $AlCuCrFeMnW_x$ (x= 0, 0.05, 0.1, 0.5 and 1 mol) alloys powders

As-milled powders of AlCuCrFeMnWx (x= 0, 0.05 ,0.1, 0.5 and 1mol) alloy are mechanically alloyed for 20 hr were spark plasma sintered by using Dr. Sinter (Model- S625) at 900^{o}C using a graphite die. Graphite dies was purchased from Nikunj Eximp. Entp. P Ltd., Mumbai with the dimension Dia 50 X ID 20.4 X 40mm long. Graphite pinches are had a dimension of Dia 20 X 20mm. The as milled alloy powders were filled in a die cavity having diameter of 20 mm. Graphite foil was used to prevent the sticking of alloy powders from the die walls.

At first as milled AlCuCrFeMnWx (x= 0, 0.05, 0.1, 0.5 and 1mol) alloys were SPSed at 900^{o}C. The holding time at sintering temperature, the heating rate and applied load were 10 min, 100^{o}C/min and 50 MPa, respectively.

3.2 Characterization of AlCuCrFeMnW$_x$ (x= 0, 0.05, 0.1, 0.5 and 1 mol HEAs

Different characterization techniques were used to analyze the phase evolution in AlCuCrFeMnW$_x$ alloys. The methods were discussed in subsequent paragraphs.

3.2.1 Density measurement

Theoretical density has been calculated by the rule of mixture given by Eq. 3.1 [3]:

$$\rho_{th} = \rho_m . (1-V_f) + \rho_f . V_f \quad (3.1)$$

where ρ_m and ρ_f are the densities of matrix and filler and V_f is the volume fraction respectively. The densities of sintered samples were determined by the Archimedes principle using a density measurement apparatus and precise weighing balance (Mettler Toledo) with the accuracy of 0.1mg. Ethanol as a media was used to determine the bulk density of the alloys. The density was calculated by Eq. 3.2 [3]:

$$\rho_{exp.} = [W_{air}/(W_{air} - W_{med})] \text{ X } \rho_{med} \quad (3.2)$$

where W_{air} and W_{med} are the weight of the sample in air and medium respectively. The ρ_{med} is the density of the medium.

3.2.2 Phase evolution studies using XRD

Phase changes from the sintering process were characterized by X-Ray Diffraction **(**XRD) using an X'pert Pro (Panalytical, USA) X-ray diffractometer unit with a CuKα (λ=0.1540598 nm) source. The scan step size and scan time was fixed to be 0.02^o and 0.7sec respectively. XRD have been performed to study the phase evolution both after MA and sintering. Also, lattice parameter, crystallite size and lattice strain is calculated by using the XRD data. The deconvolution of the overlapped peak is performed by the Lorentzian function and instrumental broadening was corrected using single crystal Si wafer. The crystallite size was calculated is calculated by the Scherrer equation given by [3]:

$$D = \frac{K\lambda}{\beta cos\theta} \quad (3.3)$$

Where D is the crystallite size, K is the shape factor (~ 1), λ is the X-Ray wavelength, β is the line broadening, θ is the Bragg angle.

3.2.3 Microstructure by scanning electron microscopy (SEM)

Microstructure of the as milled alloy powders and sintered alloys were characterized by using FE-SEM (Nova Nano 450SEM, FEI, North America) operated at 30 kV. The sample of as milled alloy powders was prepared by dispersing and sticking the powder on carbon tape and analyzed under SEM. The samples of sintered bulk alloys were prepared by grinding on a series of bonded abrasive paper (SiC) up to 1200 grit size. Mirror finish of the alloy surface was obtained by velvet cloth polishing using mixture of alumina powder (particle size, 1μm) and kerosene. Local phase composition was characterized by energy dispersive X-ray spectroscopy (EDS) detector (Bruker, Germany).The EDS data were obtained from at least 5 points, and the atomic percentage of each element has been averaged out.

3.2.4 Microstructure and phase study by transmission electron microscopy (TEM)

Investigation of the microstructure at the sub-micron scale conducted by transmission electron microscopy (TECHNAI 20, FEI, North America) operated at 200 kV. High resolution-TEM, dark field TEM and selected area electron diffraction (SAED) patterns of as milled alloy powders were analyzed to confirm the crystallite size and phases present. TEM samples for as milled alloy powders were prepared by ultra sonicating the milled powders in ethanol for 30 min. Agglomerated particles were allowed to settle down for 10 min. Then the sample from upper part of the solution was collected using micropipette and spread onto the carbon coated copper grid. TEM samples for the bulk alloys were prepared by thinning by mechanical grinding up to 80 μm followed by dimpling and ion milling. Further Scanning Transmission Electron Microscopy (STEM) was performed and the phase composition at sub-micron level is investigated by EDS (Bruker, Germany) technique.

3.3 Thermal Behavior by DSC

As-milled powder samples were analyzed up to 1000^{o}C with the heating rate of 10^{o}C/min utilizing Perkin Elmer Differential Thermal Analysis (DTA) (Model no.: STA 6000) to examine the phase stability of the HEAs with respect to temperature. Baseline was corrected before

acquiring the temperature curve for each alloy. For all the alloy samples the data were acquired repeatedly for 3 times to check the reproducibility of the results.

High-temperature stability of spark plasma sintered sample was determined up to 1000^{o}C by using Differential Thermal Analysis (DTA) (Netzsch Model no. DSC 404 F3). Activation energy of sintered alloy calculated at three different heating rates of 10 K/min, 20 K/min and 30 K/min respectively. Furthermore, according to the peak temperatures of DSC curves at different heating rates, the apparent activation energies of crystallisation can be obtained using the Kissinger relation.

3.4 Mechanical Testing

3.4.1 Microhardness

Vickers hardness measurements were performed by UHL VMHT (Walteruhl GmBH, Germany) on bulk AlCuCrFeMnWx (x= 0, 0.05 , 0.1, 0.5 and 1mol) HEAs. The load of 200 gf and dwell time of 15 sec was applied to take the hardness of the bulk alloys. The hardness is given by the Eq. 3.5 [80]:

$$HV = 0.1891\ \frac{F}{d^2}\left[\frac{kgf}{mm^2}\right] \tag{3.4}$$

Where F is the load applied and d is the diagonal of the indentation

Hardness test was performed at 5 different positions in the same alloy to check the reproducibility.

3.4.2 Compressive strength

Compressive properties were tested using Instron UTM 5500 machine at loading rate of 0.5 mm/min. The samples were cylindrical, Φ3mm×5 mm and three tests were done to attain the average value of compressive strength. Microstructure of fracture surface of the alloys was characterized by using FE-SEM (Nova Nano 450SEM, FEI, North America) operated at 15 kV.

3.4.3 Room temperature nanoindentataion creep

The nanoindentation experiments were performed at room temperature, using an Anton Paar, nanoindenter (Ttx nht2) with a Berkovich diamond tip (include the angle 142.3^{o}). The displacement and load resolutions of the machine are 0.01 nm and 50mN, respectively. In For the polished AlCuCrFeMnW$_x$ (x= 0, 0.05, 0.1, 0.5 and 1mol) alloys,, creep properties were characterized by a constant loading rate of 0.5 mN / s. The indenter was held for 200 seconds in a series of loading-unloading cycles with different maximum loads 50, 100, 150 and 200 mN. The indantation locations on the sample were chosen to be at the middle of each grain and the hardness was studied using the maximum loads 50, 100, 150 and 200 mN by Oliver-Pharr maximum loads 50, 100, 150 and 200 mN [103]. The creep tests were conceded out until the thermal drift was less than 0.03 nm / s.

3.5 Electrochemical Experiments for Corrosion Study

3.5.1 Test materials

As-milled powders of AlCuCrFeMnW$_x$ (x= 0, 0.05, 0.1, 0.5 & 1 mol) alloys are mechanically alloyed for 20 hr were spark plasma sintered by using Dr. Sinter (Model- S625) at 900^{o}C. The high entropy alloy cylinder used for electrochemical measurements has a thickness of 3 mm and a diameter of 20 mm. The epoxy resin is then cold-installed each test sample, to obtain an exposed surface area of high entropy alloy of 3.14 cm^2. Prior to each electrochemical experiment, all samples were mechanically polished using a series of 240-600 carbide of silicon sandpaper (SiC) and washed with acetone and distilled water.

3.5.2 Electrochemical measurements

Potentiodynamic polarization measurements of bulk AlCuCrFeMnW$_x$ (x= 0, 0.05, 0.1, 0.5 & 1 mol) alloys was carried out in a typical three-electrode cell setup with the specimen as a working electrode, a saturated calomel reference electrode (SCE), and a platinum counter electrode. The potential of the working electrode was measured through the Luggin probe with respect to the reference electrode which was placed as close as possible to the specimen. The electrochemical polarization measurements were conducted in aerated 3.5% NaCl solution at 25^{o}C under atmospheric pressure. The specimen was scanned potentiodynamically at a rate of 1mVs^{-1} from

the initial potential of −250mV versus open circuit potential to the final potential of 1.6 V_{SCE}. The EIS was carried out in a range of frequency from 10^4 to 10^{-3} Hz.

Potential polarization measurements of AlCuCrFeMnWx (x = 0, 0.05, 0.1, 0.5 and 1 mol) bulk alloys performed in a typical three-electrode device with sample as working electrode, calomel reference electrode Saturated (SCE) and Platinum counter electrode. The potential of the working electrode is tested by the Luggin probe relative to the reference electrode, and the reference electrode is placed as close as possible to the sample. The electrochemical polarization measurements were performed in a 3.5% NaCl solution aerated at 25 ° C. and under atmospheric pressure. The sample was potentiodynamically scanned from an initial potential of -250 mV to an open circuit potential of 1.6 VSCE at a rate of 1 mVs-1. The frequency of implementation EIS varies from 10^4 to 10^{-3} Hz.

3.5.3 Phase, surface morphology and infrared spectroscopy of corroded surface

Phase changes after corrosion processes were characterized by XRD using an X'pert Pro (Panalytical, USA) X-ray diffractometer unit with a Cu_Kα (λ=0.1540598 nm) source. Instrumental broadening was corrected using single crystal Si wafer. After the polarization experiment, the sample was cleaned with distilled water. Then, the morphology of the corrosion surface of the high entropy alloy was studied using FE-SEM (Nova Nano 450SEM, FEI, North America) operated at 30 kV Immediately after the corrosion test . Infrared (IR) spectroscopy was employed to characterize the corrosion product after polarization measurement. FTIR spectrometer (Perkin Elmer, Spectrum Two, L160000A) was used for this purpose. The IR spectrum was acquired from the range of 400 cm^{-1} to 4000cm^{-1}.

Chapter 4

SYNTHESIS AND CHARACTERIZATION OF $AlCuCrFeMnW_x$ HEAs BY MECHANICAL ALLOYING:

Novel $AlCuCrFeMnW_x$ (x=0, 0.05, 0.1, 0.5 and 1 mol) alloys were synthesized by mechanical alloying (MA). The effect of W content on the phase evolution of HEAs was investigated using X-Ray diffractometry (XRD), scanning electron microscopy (SEM), transmission electron microscopy (TEM) and selected area electron diffraction (SAED) pattern analysis.

4.1 Phase Analysis of $AlCuCrFeMnW_x$ HEAs

XRD pattern of AlCuCrFeMnWx (x=0, 0.05, 0.1, 0.5 and 1 mol) HEAs powders is shown in Fig. 4.1, which is that successively collected after the predefined interval. Figure 4.1a shows the phase evolution of AlCuCrFeMn. As the staring in milling time (after 10 min.) peaks of the individual elements are present, it shows solid solution is not formed. As the milling time increases up to 5 hr peaks of Al and Mn is partially disappear and after the 10 hr peaks of Al and Mn is disappear, and intensity of peaks is decreased it means crystallite size decreases and lattice strain increases after increasing of milling time.

Even after 10 hr of milling, an FCC peak of some undissolved Cu was observed which is due to its high positive enthalpy of mixing with the other elements. As shown, solid solution formation started after 10 hr and completed after 20 hr of milling. After 20 hr of milling, it was observed that AlCuCrFeMn powder consists of BCC as the major phase with minor FCC phase. The Neilson–Riley method gives precise lattice parameter as 287.78 pm. Based on the XRD pattern of Fig.4.1a and the precise lattice parameter of Table 4.1, the elemental alloying sequence of this HEA to milling time is Al followed by Mn then Fe and then a fraction of Cu into Cr matrix.

Figure 4.1b and 4.1c illustrate the phase evolution of $AlCuCrFeMnW_{0.05}$ and $AlCuCrFeMnW_{0.1}$ HEA to milling time. The lattice parameter as calculated for BCC 2 phase (Cr type) and BCC 1 phase (W type) to be 288.5 pm and 307.12 pm respectively in case of $AlCuCrFeMnW_{0.05.}$ Further, the lattice parameter as calculated for BCC 2 phase (Cr type) and BCC 1 phase (W type) to be 288.3 pm and 308.21 pm respectively for $AlCuCrFeMnW_{0.1}$ According to this XRD pattern and analysis of lattice parameter are shown in Table 4.2, it is clear that the alloying sequence in

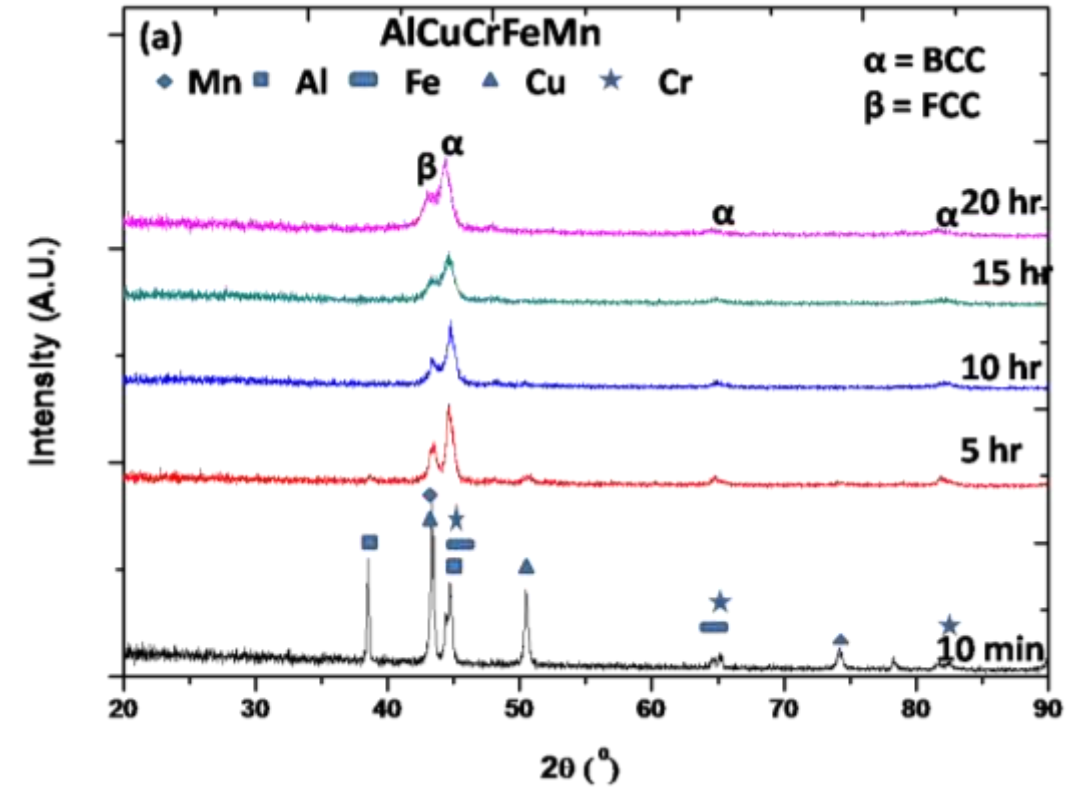
(a)
AlCuCrFeMn
Mn Al Fe Cu Cr
α = BCC
β = FCC
β
α
α
α
20 hr
15 hr
10 hr
5 hr
10 min
Intensity (A.U.)
20
30
40
50
60
70
80
90
2θ (°)

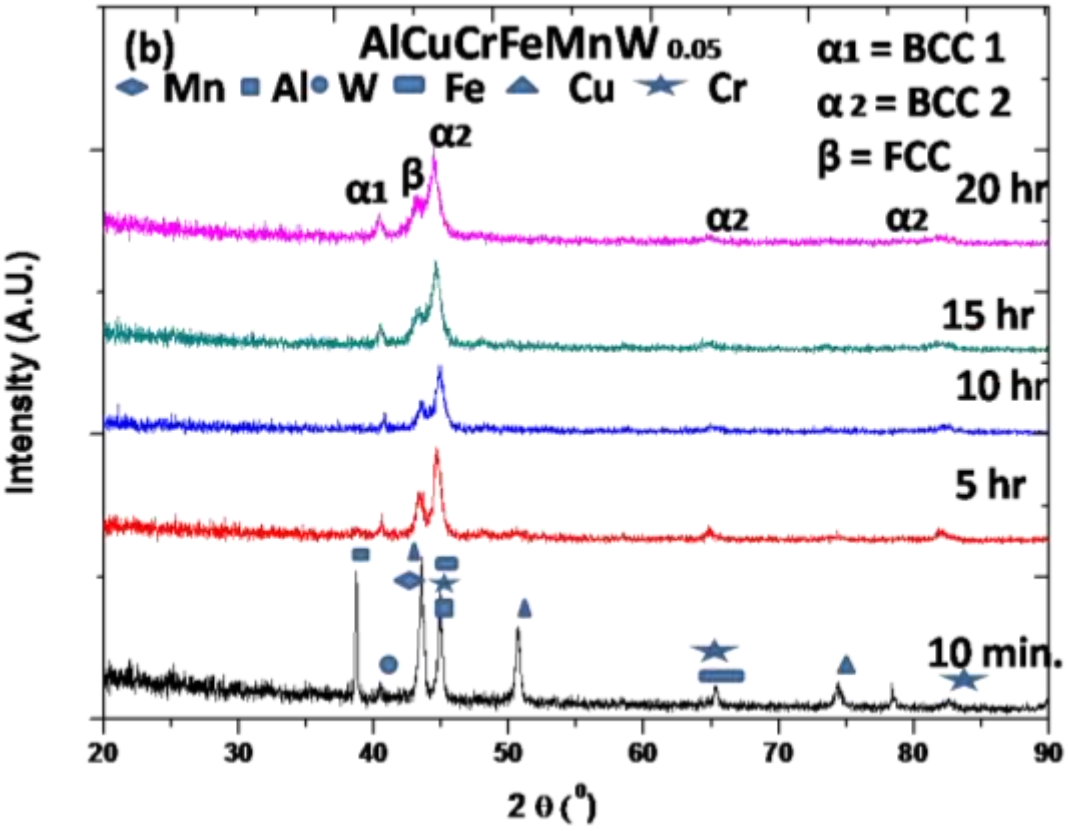
(b)
AlCuCrFeMnW 0.05
Mn Al W Fe Cu Cr
α1 = BCC 1
α 2 = BCC 2
β = FCC
α1
β
α2
α2
α2
20 hr
15 hr
10 hr
5 hr
10 min.
Intensity (A.U.)
20
30
40
50
60
70
80
90
2 θ (°)

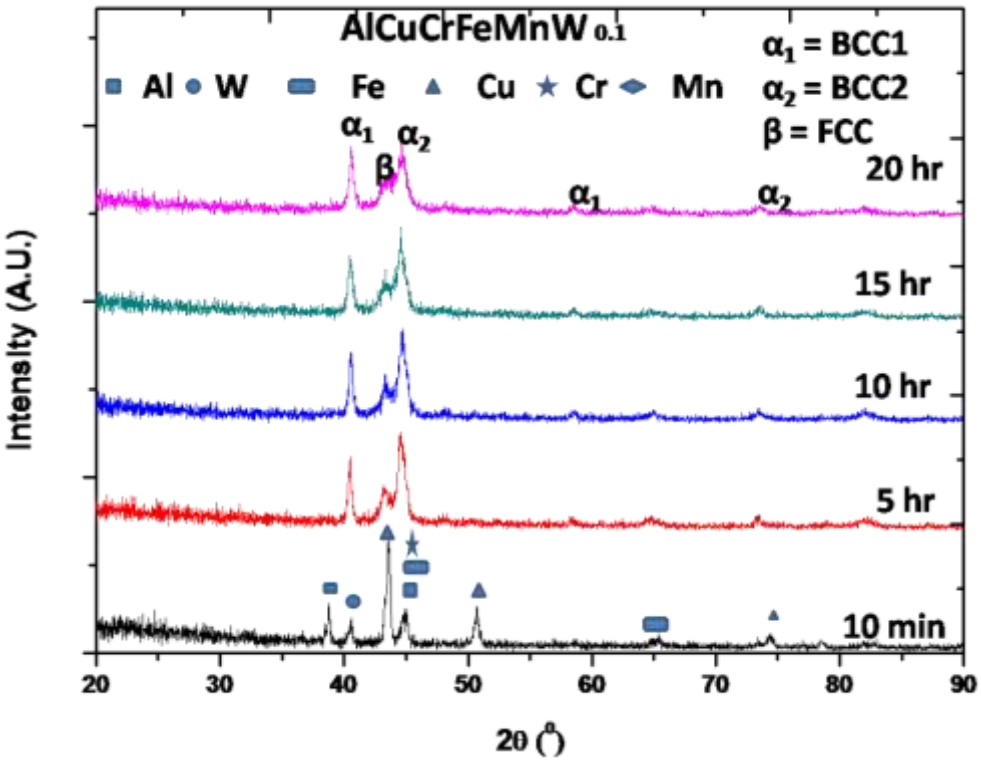
AlCuCrFeMnW 0.1
Al W Fe Cu Cr Mn
α1 = BCC1
α2 = BCC2
β = FCC
α1 α2
β
α1
α2
20 hr
15 hr
10 hr
5 hr
10 min
Intensity (A.U.)
20 30 40 50 60 70 80 90
2θ (°)

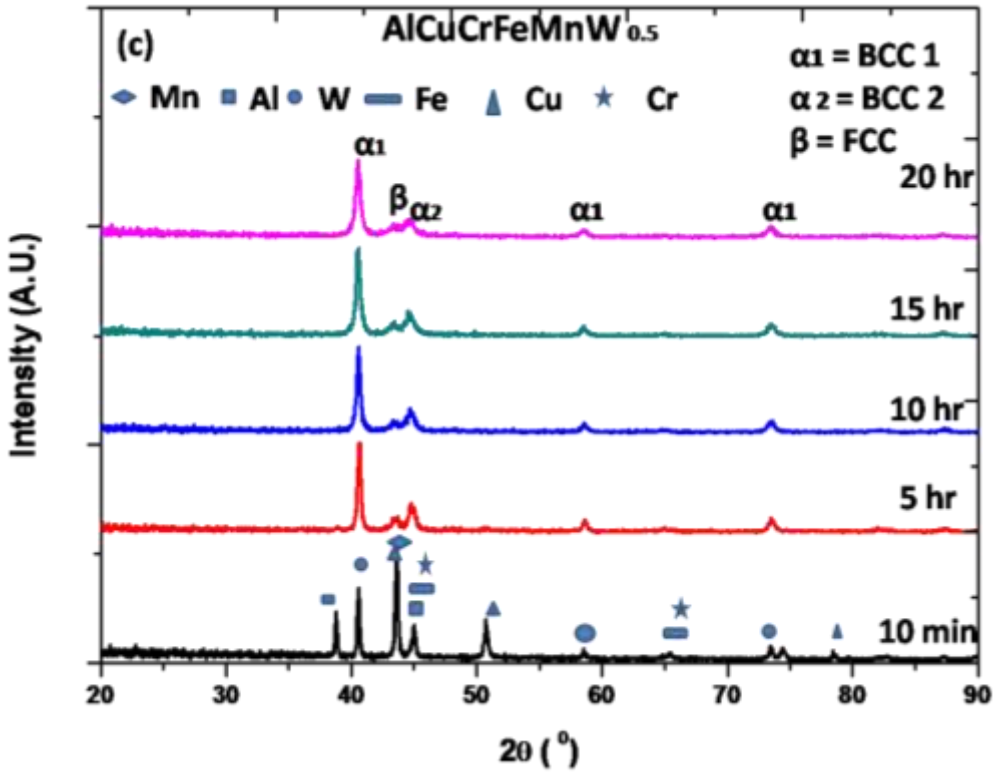
(c)
AlCuCrFeMnW 0.5
Mn Al W Fe Cu Cr
α1 = BCC 1
α 2 = BCC 2
β = FCC
α1
β α2
α1
α1
20 hr
15 hr
10 hr
5 hr
10 min
Intensity (A.U.)
20 30 40 50 60 70 80 90
2θ (°)

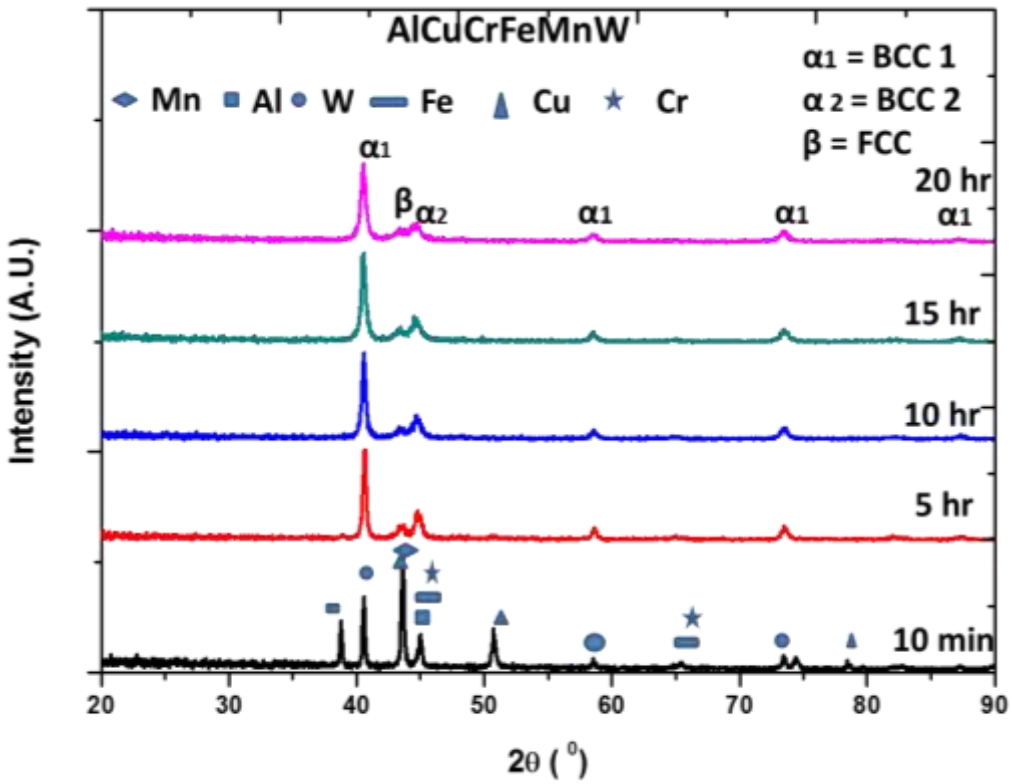

Figure 4.1 (a): XRD pattern of as a function of milling time. (a) AlCuCrFeMn (b) $AlCuCrFeMnW_{0.05}$ (c) $AlCuCrFeMnW_{0.1}$ (d) $AlCuCrFeMnW_{0.5}$ (e) AlCuCrFeMnW

multi-component $AlCuCrFeMnW_{0.05}$ and $AlCuCrFeMnW_{0.1}$ high entropy alloys may be following the trend as first Al dissolves followed by Mn then Fe and then a fraction of Cu into Cr/W matrix.

Table 4.1: Atomic size, melting point, crystal structure and lattice parameter (JCPDS) of individual elements.

	Al	**Cu**	**Cr**	**Fe**	**Mn**	**W**
Atomic size (pm)	143	128	128	127	127	139
Melting Point (^{o}C)	660	1083	1857	1538	1246	3422
Crystal Structure	FCC	FCC	BCC	BCC	BCC	BCC
Standard lattice parameter a (pm)	404.94	361.5	288.6	286.6	889	316.4

The XRD pattern of the highest tungsten content, i.e., $AlCuCrFeMnW_{0.5}$ and AlCuCrFeMnW, with varying milling time is shown in Fig. 4.1d and 4.1e. It can be seen that $AlCuCrFeMnW_{0.5}$ and AlCuCrFeMnW HEAs have a similar pattern as that of $AlCuCrFeMnW_{0.1}$ HEA. A Lattice parameter of BCC 2 phase (Cr type) calculated to be 288.6 pm and 288.89 pm, and for BCC 1 phase (W type) was calculated to be 309.12 pm and 307.18 pm. The alloying pattern for this HEA follows the similar trend as observed in case of $AlCuCrFeMnW_{0.1}$ HEA. Chen et al.[104] suggested the correlation between the melting point and the alloying rate of an individual component. It was recommended that element has more melting point has high bonding capacity and it has lower alloying rate because of lower self-diffusion coefficient of individual components. In general, different factors such as atomic size, melting point, and self-diffusion coefficient decide the mechanical alloying rate of high entropy alloy which is given in Table 4.1. In cases of AlCuCrFeMn and $AlCuCrFeMnW_{0.05}$ HEAs, all the elements after 20 hr of milling are predominantly dissolving in Cr matrix, and minor FCC phase is formed due to the high positive enthalpy of mixing between Cu and other elements and hence remaining of some undissolved Cu present in the system [105]. In contrast, higher W content HEAs such as $AlCuCrFeMnW_{0.1}$ to AlCuCrFeMnW it seems that most of the elements are diffuse mostly in W lattice and minor in Cr lattice which can be suggested by theory of Chen et al. due to high melting point of W (3422°C) and Cr (1857 °C).

Table 4.2 : Experimentally and N–R method predicted lattice parameter of $AlCuCrFeMnW_x$ (x=0, 0.05, 0.1, 0.5 and 1mol).

Composition	**Lattice Parameter** $a = d\sqrt{h2 + k2 + l2}$ **(pm)**			**Lattice parameter N–R method (pm)**
	BCC1	**BCC2**	**FCC**	
AlCuCrFeMn	---	287.18	359.90	287.78
$AlCuCrFeMnW_{0.05}$	307.12	288.5	360.12	288.5
$AlCuCrFeMnW_{0.01}$	308.21	288.3	360.45	308.21
$AlCuCrFeMnW_{0.5}$	309.12	288.6	360.45	309.12
AlCuCrFeMnW	307.18	288.5	360.90	307.78

It is observed that peak angle is slightly shifting towards the higher side of 2θ angle for AlCuCrFeMnW HEA as compared to AlCuCrFeMn HEA. Therefore, confirmation of the residual compressive stresses may be because of adding of tungsten in the lattice which in turn increases the lattice distortion. In $AlCuCrFeMnW_x$ (x=0, 0.05, 0.1, 0.5 and 1mol) HEAs, BCC structure remains the major phase after 20 hr of mechanical alloying which is due to the difference in atomic radii between the individual elements which are more than 10%. Thus, the formation of BCC structure is most favorable because it contains a higher percentage of atomic volume without much distortion and shows less packing efficiency [3].

Detailed deconvolute XRD study of $AlCuCrFeMnW_x$ (x=0, 0.05, 0.1, 0.5 and 1 mol) revealed that there is three BCC phases (FCC, BCC 1 and BCC 2) present as shown in Fig. 4.2 (a,b,c and d)

The reference intensity ratio (RIR) of the FCC phase in AlCuCrFeMn has been calculated by eq. 4.1:

$$FCC\ (RIR) = I_{FCC} / I_{FCC} + I_{BCC} \qquad (4.1)$$

Where I_{FCC} is the peak intensity of the FCC phase and I_{BCC} is the peak intensity of BCC phase.

The RIR of the FCC phase in AlCuCrFeMnWx (x=0.05, 0.1, 0.5 and 1) has been calculated by eq 4.2:

$$FCC\ (RIR) = I_{FCC} / I_{FCC} + I_{BCC1} + I_{BCC2} \qquad (4.2)$$

Where I_{FCC} is the peak intensity of the FCC phase and I_{BCC1} is the peak intensity of BCC 1 phase and I_{BCC2} is the peak intensity of BCC 2.

The % FCC phase in case of AlCuCrFeMn, $AlCuCrFeMnW_{0.05,}$ $AlCuCrFeMnW_{0.1,}$ $AlCuCrFeMnW_{0.5}$ and AlCuCrFeMnW HEAs were determined as 29%, 26%, 19%, 9% and 7% respectively. It is interesting to note that the increases of W concentration decrease the % FCC phase in proposed HEAs. This confirms that tungsten/chromium because of its high melting point effect and BCC crystal structure promoting the final BCC structure of powder sample which is in fact W and/or Cr- type BCC.

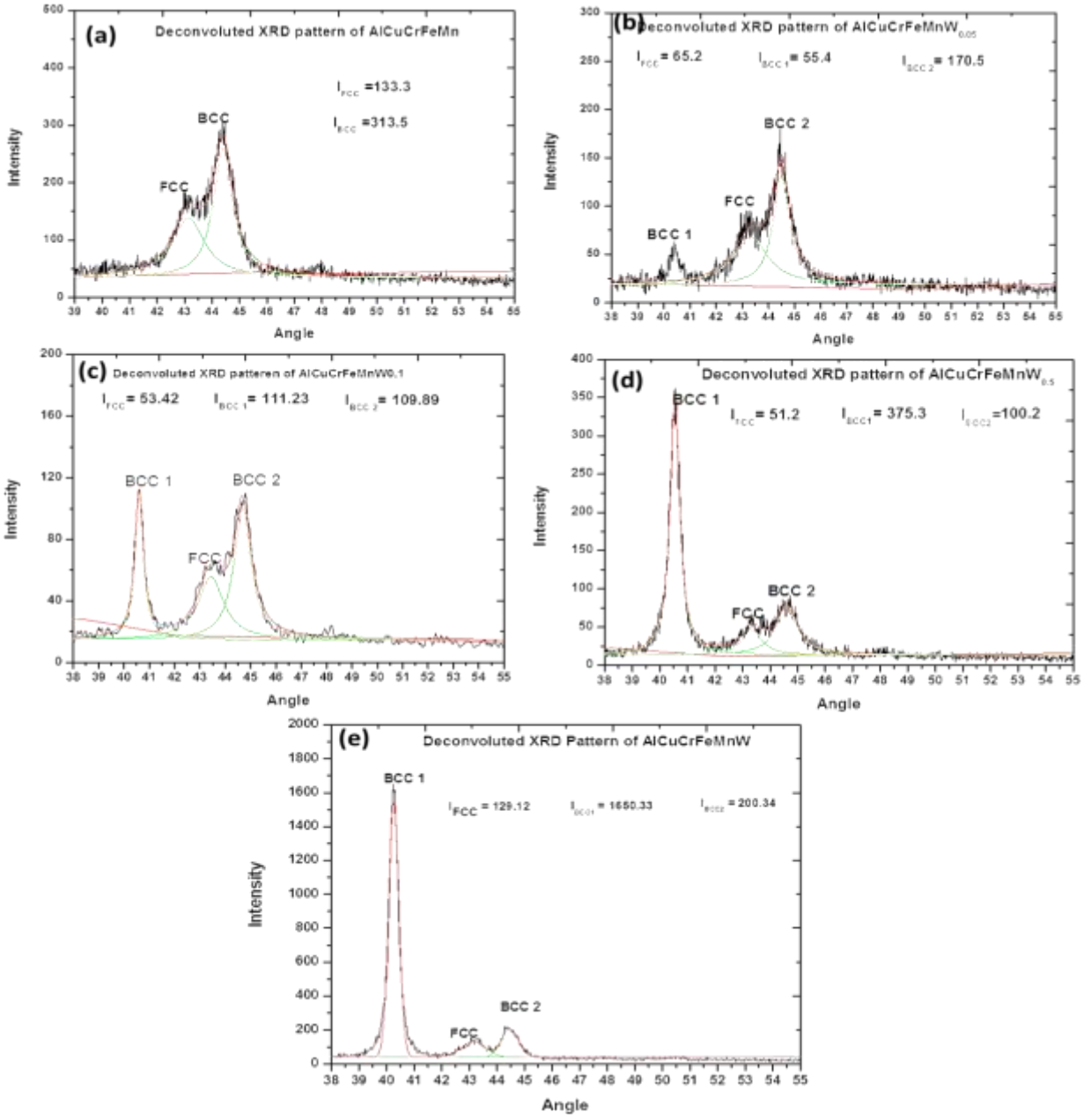

Fig. 4.2: Detailed deconvolute XRD study of AlCuCrFeMnW$_x$ (x=0, 0.05, 0.1, 0.5 and 1 mol) powders

Figure 4.3 to 4.7 shows the TEM bright field, dark field, HR-TEM and SAED patterns for AlCuCrFeMnW$_x$ (x=0, 0.05, 0.1, 0.5 and 1mol) HEAs. The interplanar spacing calculated with the help of HR-TEM and SAED pattern which is in support with the XRD results and confirms the nano-crystalline nature of present HEAs. SAED also confirmed the formation of BCC as a major phase along with a small fraction of FCC phase. Thus, it can be observed by TEM analysis

that higher W content results in dissolution of all elements in W lattice lead to the formation of major BCC phase.

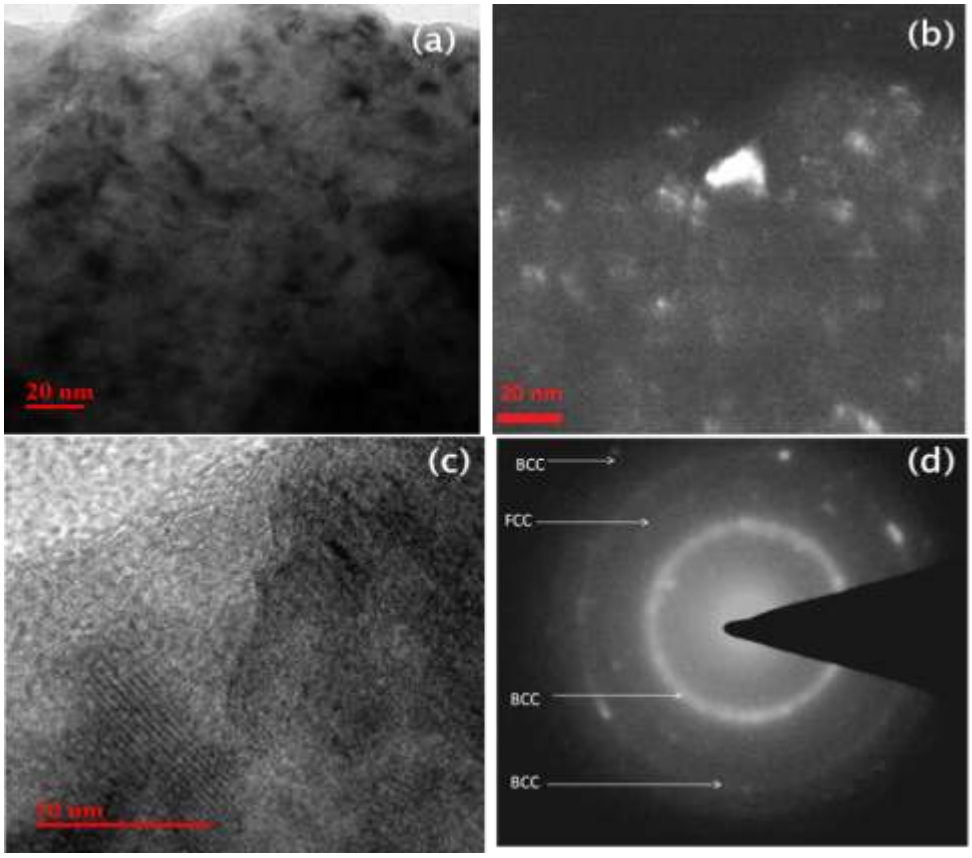

Fig. 4.3: TEM images of AlCuCrFeMn HEA powder (a) bright field (b) dark field (c) HR-TEM, (d) SAED pattern

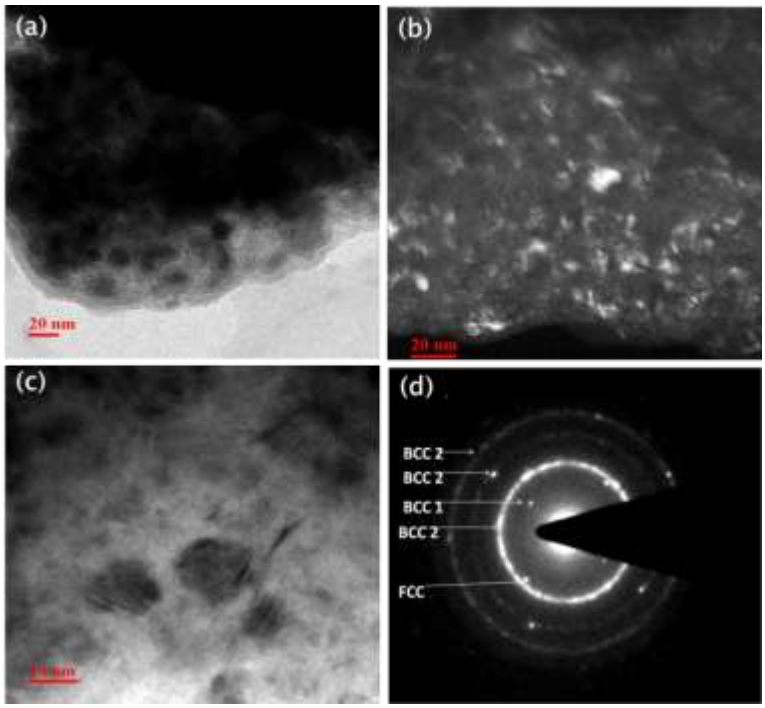

Fig. 4.4: TEM images of $AlCuCrFeMnW_{0.05}$ HEA (a) bright field (b) dark field (c) HR-TEM, (d) SAED pattern

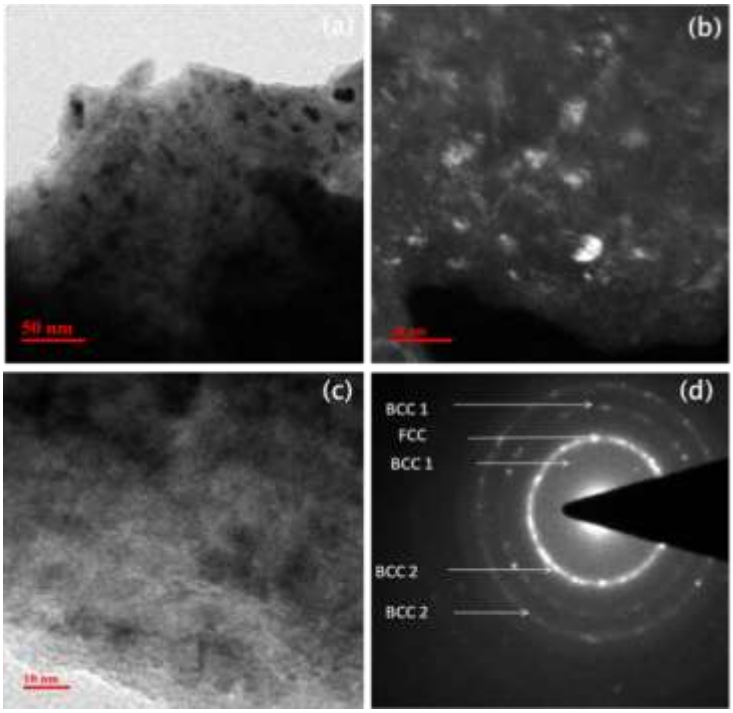

Fig. 4.5: TEM images of $AlCuCrFeMnW_{0.1}$ HEA (a) bright field (b) dark field (c) HR-TEM, (d) SAED pattern

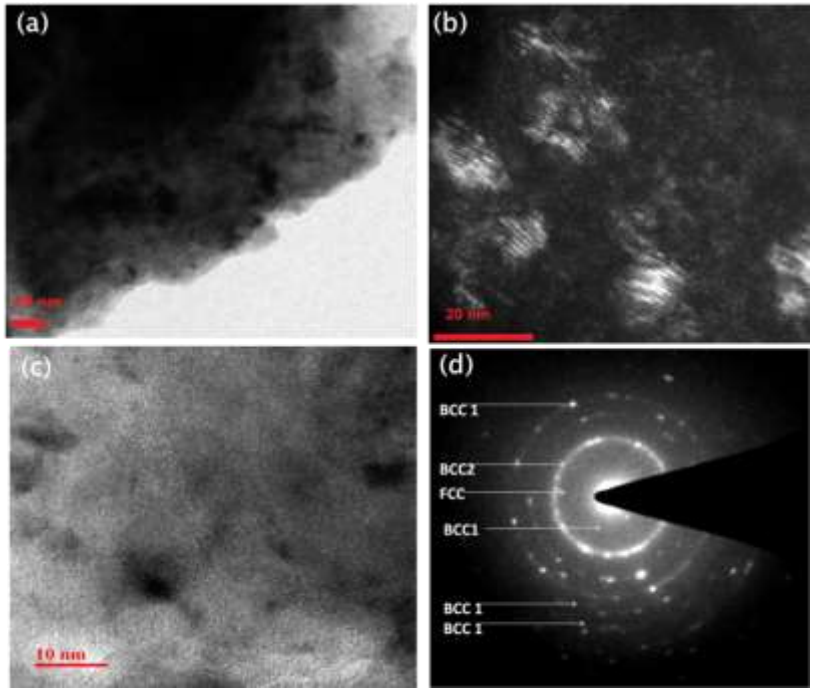

Fig. 4.6: TEM images of $AlCuCrFeMnW_{0.5}$ HEA (a) bright field (b) dark field (c) HR-TEM, (d) SAED pattern

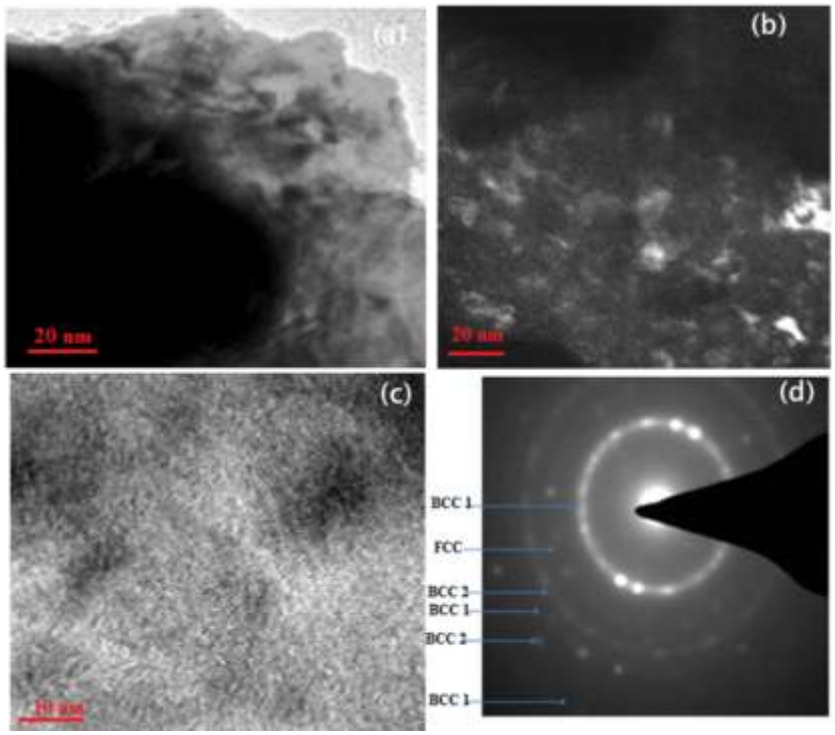

Fig. 4.7: TEM images of AlCuCrFeMnW HEA (a) bright field (b) dark field (c) HR-TEM, (d) SAED pattern

The presence of undissolved Cu as minor FCC phase is due to its high positive enthalpy of mixing with other alloying elements. Thus, it is concluded that tungsten being the highest melting point element among Cr, Fe, Al, Mn, and Cu act as a solvent element for AlCuCrFeMnW HEA alloy, whereas others behave like solute elements.

4.2 Crystallite Size and Lattice Strain:

Comparison between the crystallite size and lattice strain of $AlCuCrFeMnW_x$ (x=0, 0.05, 0.1, 0.5 and 1mol), calculated by Scherrer formula, Williamson Hall method (W–H method) and HR-TEM images, is shown in Table 4.3. It can be seen that for $AlCuCrFeMnW_x$ HEAs, the high value of crystallite size due to the presence of anisotropic variation in the residual strain. Variation in the micro-strain in AlCuCrFeMnWx (x=0, 0.05, 0.1, 0.5 and 1mol) HEAs measured by the following formula:

$$\varepsilon = \beta_{hkl}/4\tan\theta \qquad (4.3)$$

where β_{hkl} is the full-width at half maximum (FWHM).

Table 4.3 : Crystalline size by Scherer method and Williamson Hall method, HR-TEM image and the lattice strain of $AlCuCrFeMnW_x$ (x=0, 0.05, 0.1,0.5 and 1 mol).

Composition	Crystallite size (nm) Scherrer's formula	Crystallite size (nm) W-H Method	Crystallite size (nm) HR-TEM	Lattice strain (%) $\varepsilon = \beta hkl/4\tan\theta$	Lattice strain (%) W-H method
AlCuCrFeMn	11	31±4	10±3	1.63	1.43
$AlCuCrFeMnW_{0.05}$	13	37±5	11±3	1.43	1.23
$AlCuCrFeMnW_{0.01}$	15	38±5	11±2	1.11	1.09
$AlCuCrFeMnW_{0.5}$	19	39±6	12±2	0.77	0.71
AlCuCrFeMnW	17	40±5	12±3	0.53	0.51

It is interesting to note that micro-strain decreases with increase in W content of $AlCuCrFeMnW_x$ (x=0, 0.05, 0.1, 0.5 and 1mol), which may be attributed due to the decreasing atomic size mismatch [106].

4.3 Morphology and Mechanism of Alloy Formation

Figure 4.8a, b, c, d and e shows microstructures of the 10 min., 10 hr and 20 hr milled powders of AlCuCrFeMn, $AlCuCrFeMnW_{0.05}$, $AlCuCrFeMnW_{0.1,}$ $AlCuCrFeMnW_{0.5}$ and AlCucrFeMnW respectively. In present HEAs, fracturing starts during the early period of milling (10 min) may be due of the presence of high wt.% of elements having BCC structure. Subsequently, milling time increases up to 10 hr fracturing process starts dominates over cold welding resulting in smaller size particles.

Finally, after 20 h of milling, the crystallite sizes become very small this, in turn, facilitates the diffusion of different elements in a BCC phase. Mechanism of development of solid solution can be understood by two methods (1) repetitive cold welding, and fracturing, (2) diffusion. In the starting hours of milling (less than 5 hr.) all the soft elements are combined (ductile) by the cold welding and interlamellar spacing of crystal is decreased [68]. As the milling time progresses, work hardening plays the significant role in increasing the brittleness and initiates fracturing [107,108].

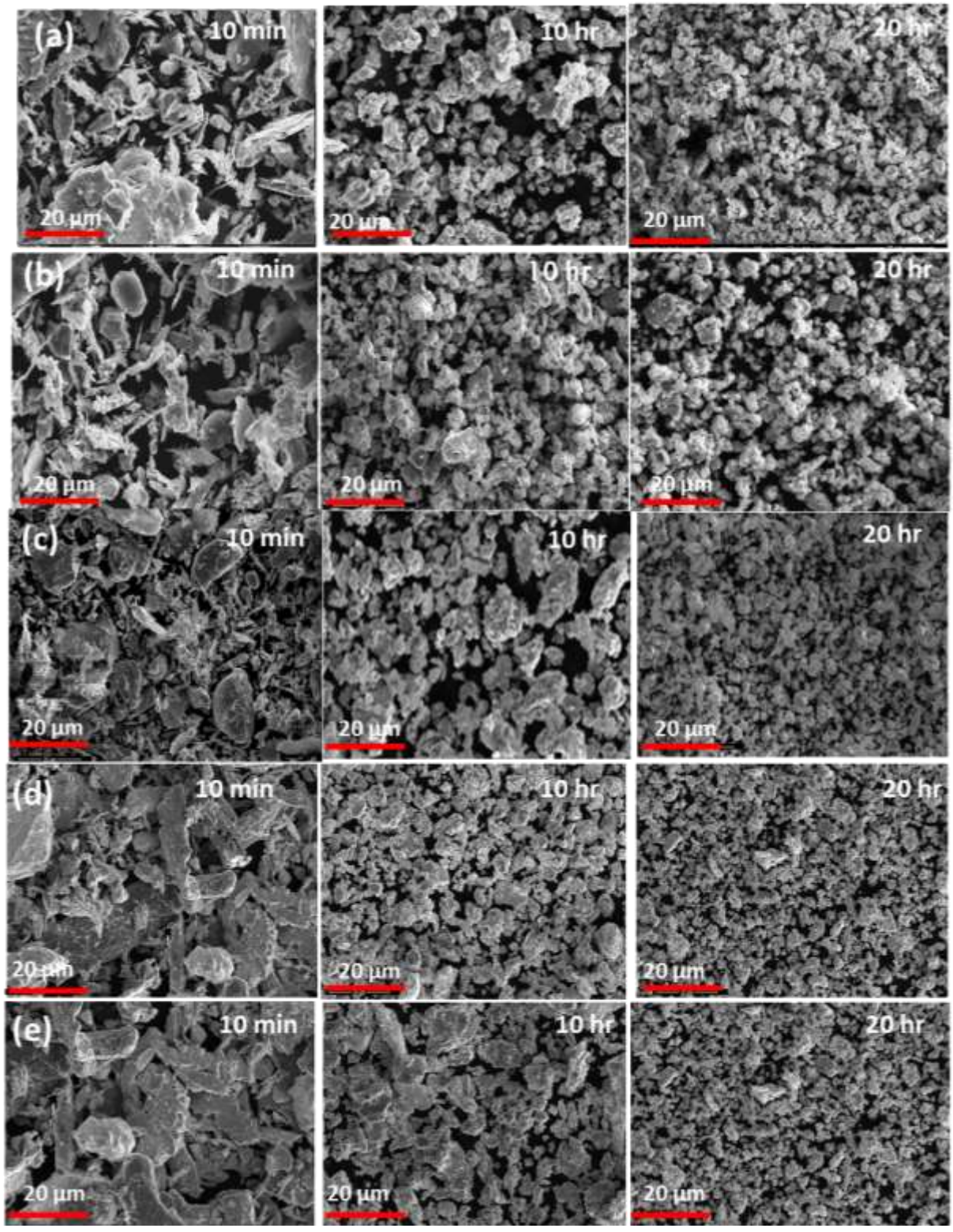

Fig. 4.8: Morphology of (a) AlCuCrFeMn, (b) $AlCuCrFeMnW_{0.05}$, (c) $AlCuCrFeMnW_{0.1}$ and (d) $AlCuCrFeMnW_{0.5}$ (e) AlCuCrFeMnW HEAs after 10 min, 10 hr and 20 hr

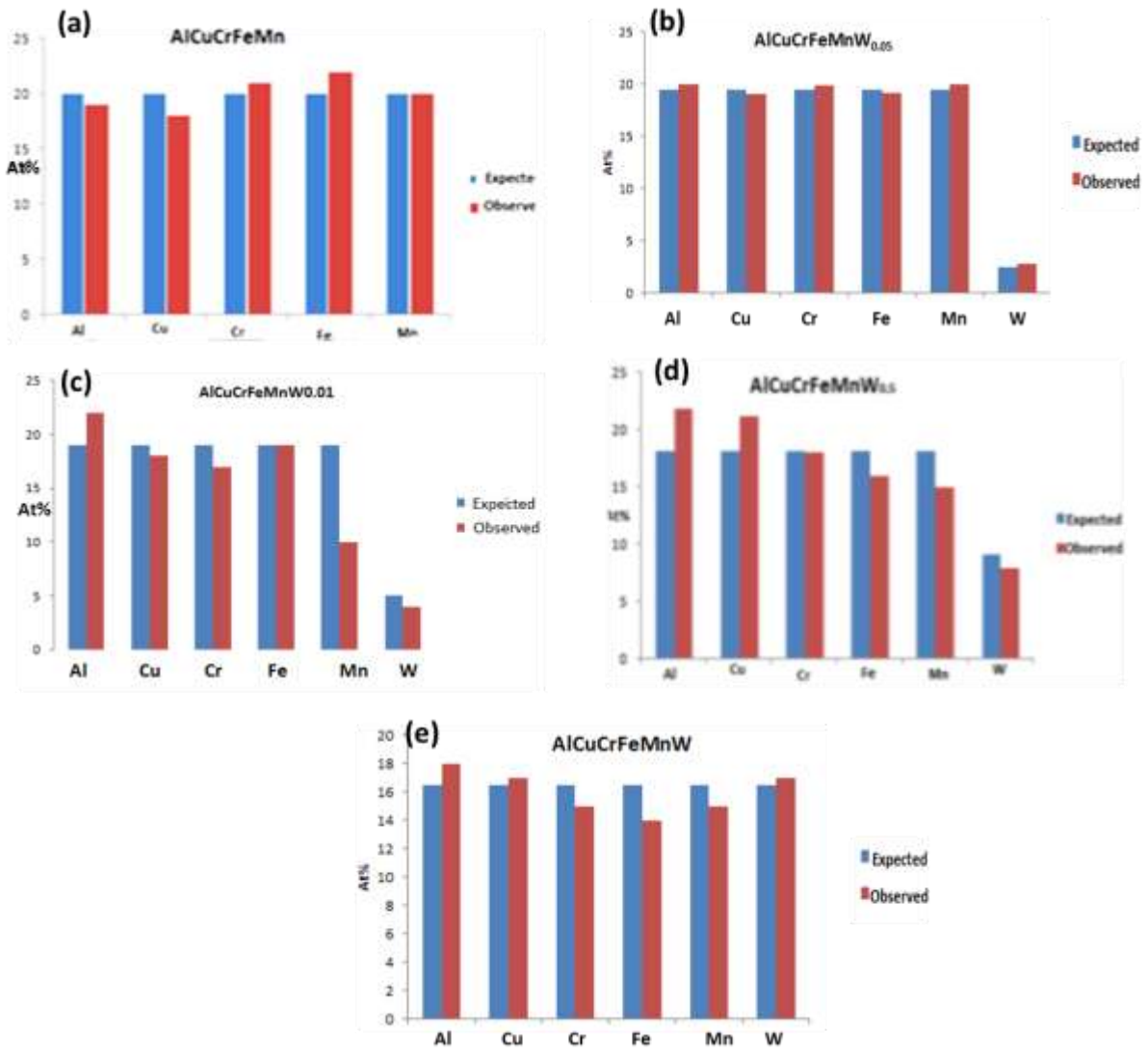

Fig. 4.9: EDS of (a) AlCuCrFeMn, (b) $AlCuCrFeMnW_{0.05}$, (c) $AlCuCrFeMnW_{0.1}$ and (d) $AlCuCrFeMnW_{0.5}$ (e) AlCuCrFeMnW HEAs

EDS mapping results of the as-milled powders are shown in the Fig. 4.9. Chemical composition by EDS data is nearly similar to theoretically chemical composition and it shows good homogeneity after mechanical alloying. In the present study also it is found that there is a homogeneous mixture of elements in BCC 1 and BCC 2 which can be seen in the EDS point analysis of the alloy powder. However, there is segregation of Cu element which corresponds to the FCC structure in an alloy.

4.4 Thermodynamic Criteria for Formation of Solid Solution

The criterion of the creation of saturated solid solution is proposed by Hume-Rothery rules for the binary alloy system which states limitations on atomic sizes difference (if possible ≤ 15%), crystal structure, valency and electronegativity. High entropy alloys form simple solid solution crystal structure of either BCC or FCC or mixtures of BCC+FCC and some cases HCP structure are also reported.

The mixing enthalpy for a multi-component alloys calculated for n element using the equation 4.4 [3]:

Table 4.4: The chemical mixing enthalpy ($\Delta Hmix_{ij}$; kJ/mol) of binary equiatomic alloys calculated by Miedema's approach [109].

Element	Al	Cu	Cr	Fe	Mn	W
Al	0	-1	-10	-11	-19	-2
Cu		0	12	13	4	22
Cr			0	-1	2	1
Fe				0	-2.9	0
Mn					0	6
W						0

$$\Delta H_{mix} = \sum_{i=1}^{n} \Omega_{ij} C_i C_j \qquad (4.4)$$

where $\Omega ij = 4\ \Delta H_{mix}^{AB}$ C_i or C_j is the atomic % of the i^{th} or j^{th} component, and $\Delta Hmix^{(AB)}$ (kJ/mol) is the mixing enthalpy formulated by Miedema's model is given in Table 4.4 for binary pairs [109].

The mixing entropy (ΔS_{mix}) of an n-element usual solution calculated as [3]:

$$\Delta S_{mix} = -R \sum_{i=1}^{n} (C_i \ln C_i) \qquad (4.5)$$

$\sum_{i=1}^{n}(C_i) = 1$, and R is the gas constant. Ω is an important parameter for predicting high entropy alloy for solid solution formation defined as [4]:

$$\Omega=\frac{T_m\,\Delta S_{mix}}{\Delta H_{mix}} \quad (4.6)$$

The melting temperature (T_m) is calculating by the rule of mixtures:

$$T_m=\sum_{i=1}^{n} C_i(\,T_m)_i \quad (4.7)$$

A parameter δ, which describes the compressive effect of the atomic size or atomic size mismatch in the n-element alloy, was calculated as [4]:

$$\delta=100\sqrt{\sum_{i=1}^{n} C_i(1-r_i/\bar{r})^2} \quad (4.8)$$

Where C_i is the atomic percentage (%) of the *i*th element and $\bar{r} = \sum_{i=1}^{n} C_i r_i$ is the average atomic radius and r_i, the atomic radius, was taken from reference [4].

Zhang et al. [4] summarized δ, ΔH_{mix} and Ω in analyzed alloys, they concluded the quantitative values for forming the solid solution by -15 kJ/mol ≤ ΔH_{mix} ≤ 5kJ/mol, Ω≥1 and 1≤δ≤6. The effect of valence electron concentration can determine the structure of the solid solution. It can be concluded that higher value of VEC stabilized FCC phases (VEC ≥ 7.8) and lower value of VEC stabilized BCC phases (VEC < 6.87). In the range 6.87 ≤ VEC < 7.8 mixed phases of BCC and FCC will exist [3].

For HEAs, VEC was followed as [3]:

$$VEC=\sum_{i=1}^{n} C_i(\,VEC)_i \quad (4.9)$$

Table 4.5 shows the theoretical value of ΔH, δ, and ΔS_{conf} for AlCuCrFeMnW$_x$ (x=0, 0.05, 0.1, 0.5 and 1mol) HEAs. It was observed that the enthalpy of mixing (ΔH) is more positive with higher W concentration due to high positive enthalpies of W-Cu and W-Mn systems. ΔS_{conf} increases with an increase in W content and it is highest for AlCuCrFeMnW HEA. ΔS_{conf} supports the successfully formation criteria of the solid solution because of its typical value, i.e., 11.5 J/mol·K.

Table 4.5: Thermodynamic parameters of $AlCuCrFeMnW_x$ (x= 0, 0.05, 0.1, 0.5 & 1.0 mol) alloys

Composition	ΔH_{mix} (KJ/mol)	ΔS_{mix} ($JK^{-1}mol^{-1}$)	Tm (K)	Ω	δ (A^o)	VEC
AlCuCrFeMn	-1.76	13.38	1561	11.48	5.55	7
$AlCuCrFeMnW_{0.05}$	-1.51	13.67	1582	14.48	5.50	6.98
$AlCuCrFeMnW_{0.1}$	-1.28	14.16	1600	17.63	5.40	6.97
$AlCuCrFeMnW_{0.5}$	0.31	14.65	1746	82.51	5.24	6.88
AlCuCrFeMnW	-1.54	14.79	1909	18.20	4.98	6.87

It is concluded that thermodynamical parameters of $AlCuCrFeMnW_x$ support the formation of the solid solution [2]. Fig. 4.10 shows the variation between W content and VEC for $AlCuCrFeMnW_x$ HEAs. It is clear from Fig. 4.10 that as the increasing of W concentration in $AlCuCrFeMnW_x$ HEAs decreasing the VEC from 7 to 6.88. Hence, it is important to note that due to the higher W content, the crystal structure of the final powder rearranges itself in BCC form (W-type). Also, VEC of $AlCuCrFeMnW_x$ HEAs supports the criteria given by Guo et al. [58] for the formation BCC, BCC + FCC and FCC. It is also be noted that some FCC phase fraction present in AlCuCrFeMn, $AlCuCrFeMnW_{0.05}$, $AlCuCrFeMnW_{0.1}$, $AlCuCrFeMnW_{0.5}$ and AlCuCrFeMnW is due to the fact that VEC of these HEAs are very near to the boundary level of BCC, i.e., VEC = 6.87.

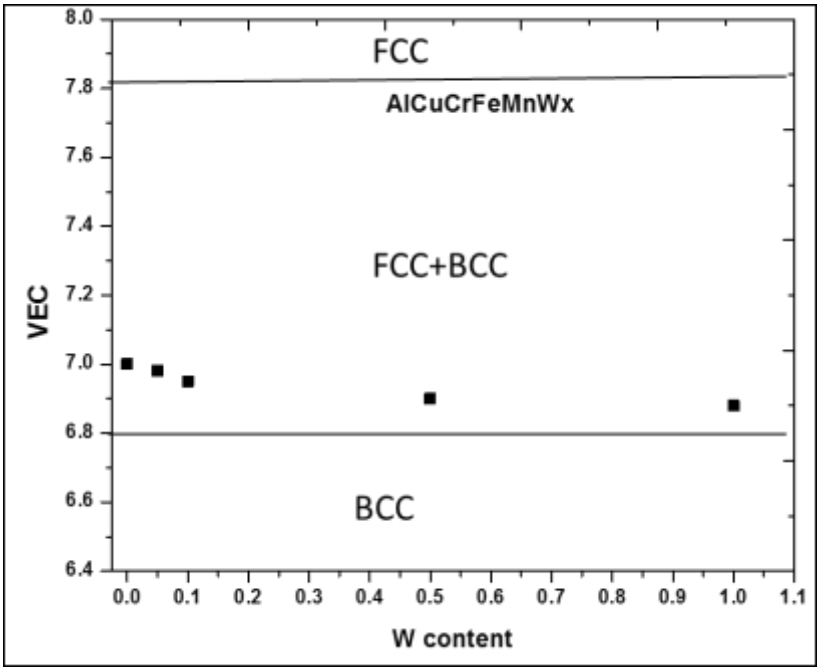

Fig. 4.10: Variation between W content and VEC.

The presence of copper in HEA contributed in shifting the VEC value near to defined boundary level value of BCC which leads to the existence of the small fraction of FCC phase in case of $AlCuCrFeMnW_x$ (x=0, 0.05, 0.1, 0.5 and 1mol) HEAs.

4.5 Thermal Behavior of Powder Samples

Thermal analysis was performed using DSC to study the thermal stability of the phases present in powder samples of AlCuCrFeMnWx HEAs. Figure 4.11 shows the thermal analysis of AlCuCrFeMn, $AlCuCrFeMnW_{0.05}$, $AlCuCrFeMnW_{0.1}$, $AlCuCrFeMnW_{0.5}$ and AlCuCrFeMnW HEAs. It is shown in the figure that all HEAs are thermally stable till 1000 °C, and there are no significant phase changes in this temperature range. The nature of DSC curve traces in the range of room temperature (RT) to 1000 °C for AlCuCrFeMn, $AlCuCrFeMnW_{0.05}$, $AlCuCrFeMnW_{0.1}$, $AlCuCrFeMnW_{0.5}$ and AlCuCrFeMnW which may be the cause of relaxation of internal residual stress and lattice strain caused due to severe deformation during mechanical alloying. However, there was no phase transformation observed till 1000^oC.

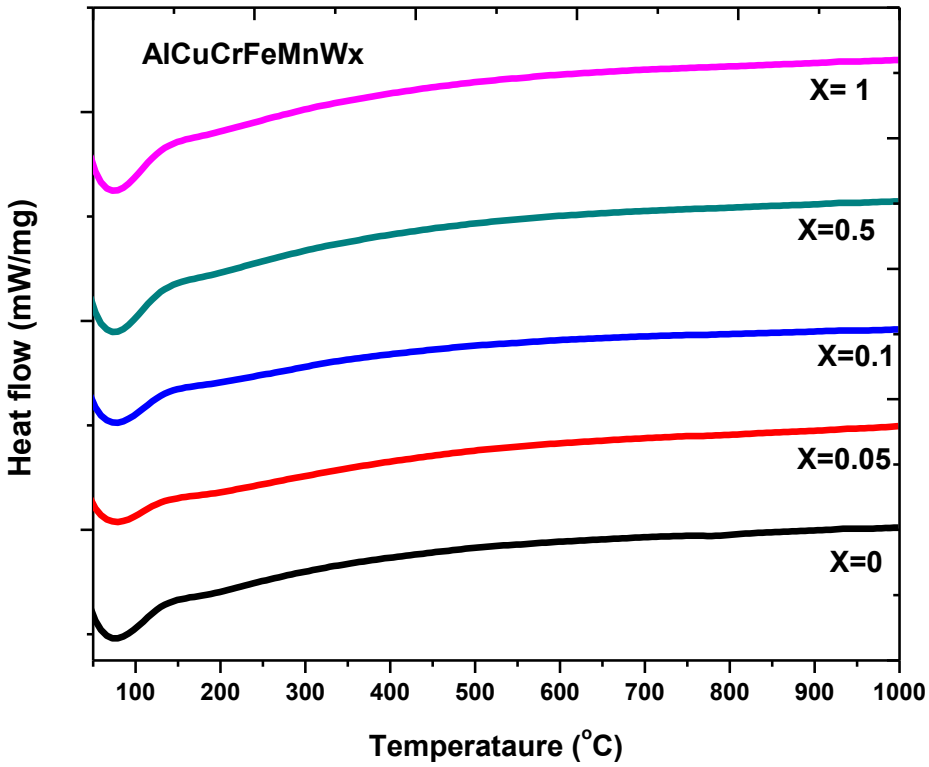

Fig. 4.11: DSC scan of AlCuCrFeMnW$_x$ (x=0, 0.05, 0.1, 0.5 and 1 mol) HEAs

Based on the present study, it can conclude that proposed HEAs, i.e., AlCuCrFeMnW$_x$ were stable up to 1000 °C thus could be considered as a potential candidate for high temperature applications. Further studies on high-temperature oxidation behavior will provide a complete understanding for defining the suitability of the proposed HEAs.

Novel AlCuCrFeMnW$_x$ (x=0, 0.05, 0.1, 0.5 and 1 mol) HEAs prepared by mechanical alloying. XRD analysis indicates the formation major BCC phase with minor FCC fraction in these HEAs. Although AlCuCrFeMnW$_x$ (x= 0.05, 0.1, 0.5 and 1 mol) have two BCC phases i.e. BCC 1and BCC 2 as confirmed by XRD. The % FCC phase in case of AlCuCrFeMn, AlCuCrFeMnW$_{0.05,}$ AlCuCrFeMnW$_{0.1,}$ AlCuCrFeMnW$_{0.5}$ and AlCuCrFeMnW HEAs were determined as 29%, 26%, 19%, 9% and 7% respectively. Also, calculated thermodynamical parameters suggest that present HEAs follow criterions given for the formation of a single phase solid solution. Moreover, phase evolution results shows that the addition of W enhances the probability of formation of BCC structure.

Further studies on the bulk HEAs have been performed to understand the phase formation and the properties of the sintered $AlCuCrFeMnW_x$ (x=0, 0.05, 0.1, 0.5 and 1 mol) alloys, which are discussed in the next chapter.

Chapter 5

SPARK PLASMA SINTERING OF AS-MILLED $AlCuCrFeMnW_x$ (0, 0.05, 0.1, 0.5 & 1 mol) HEAs

The as milled $AlCuCrFeMnW_x$ (0, 0.05, 0.1, 0.5 & 1 mol) alloys were spark plasma sintered at 900^oC. The structure-property relationship has also been proposed by conventional strengthening mechanisms.

5.1 Bulk Density Measurements

In general the sintering temperature may be defined as to be around 0.5-0.7 T_m where T_m is absolute melting temperature in Kelvin. Although due to an absence of melting point of these alloys the sintering temperature was approximated with respect to the theoretical melting point. Most of the literature suggests that the sintering temperature for nano crystalline powders, to be kept at the range of 0.5 - 0.7 T_m. Moreover, high surface to volume ratio of nanoparticles also provides a substantial sintering dynamic force by which the sintering temperature can be correctly reduced.

Table 5.1: Experimental bulk density and calculated relative density of $AlCuCrFeMnW_x$ (x= 0, 0.05, 0.1, 0.5 & 1.0 mol) HEAs

Composition	Theoretical Density (g/cm^3)	Experimental Bulk Density (g/cm^3)	Relative Density (%)
AlCuCrFeMn	6.84	6.56	96
$AlCuCrFeMnW_{0.05}$	6.90	6.58	95.5
$AlCuCrFeMnW_{0.1}$	7.09	6.68	94.3
$AlCuCrFeMnW_{0.5}$	7.92	7.45	94.1
AlCuCrFeMnW	8.92	8.34	93.5

The theoretical density of the spark plasma sintered alloy was calculated using the rule of mixtures. The experimental density of the sintered alloys was measured by Archimedes's Principle and relative density was calculated by using image analysis. It is noted that for each alloy system the relative density ranges from 93-96%. Thus, confirming low fraction of porosity in the sintered alloy are shown in Table 5.1.

5.2 Structural Evolution of AlCuCrFeMnWx HEAs After Sintering

In this section phase evolution, microstructure and phase transformation study of the sintered $AlCuCrFeMnW_x$ alloy were investigated by X-ray diffraction (XRD), scanning electron microscopy (SEM), transmission electron microscopy (TEM) and differential scanning calorimetry (DSC).

5.2.1 Phase analysis by X-ray diffraction (XRD)

Phase evolution studies by X-Ray diffraction suggest that as-milled $AlCuCrFeMnW_x$ (x= 0, 0.05, 0.1, 0.5 & 1 mol) HEA has been consolidated by spark plasma sintering at 900°C are shown in Fig. 5.1.

The microstructure of sintered $AlCuCrFeMnW_x$ (x=0.05, 0.1, 0.5 & 1 mol) HEAs contained of major AlFe type ordered phase (JCPDS: 00-033-0020), BCC phase and FeMn phase (JCPDS: 01-071-8284) with some minor peaks of σ phase (JCPDS: 01-071-7530) having a tetragonal structure and microstructure of AlCuCrFeMn is AlFe type ordered structure, FeMn phase with metastable Cr rich σ-phase precipitates. The development and progress of Cr rich precipitates in FeMn phase in $AlCuCrFeMnW_x$ HEA are due to high positive enthalpy between the binary elements.

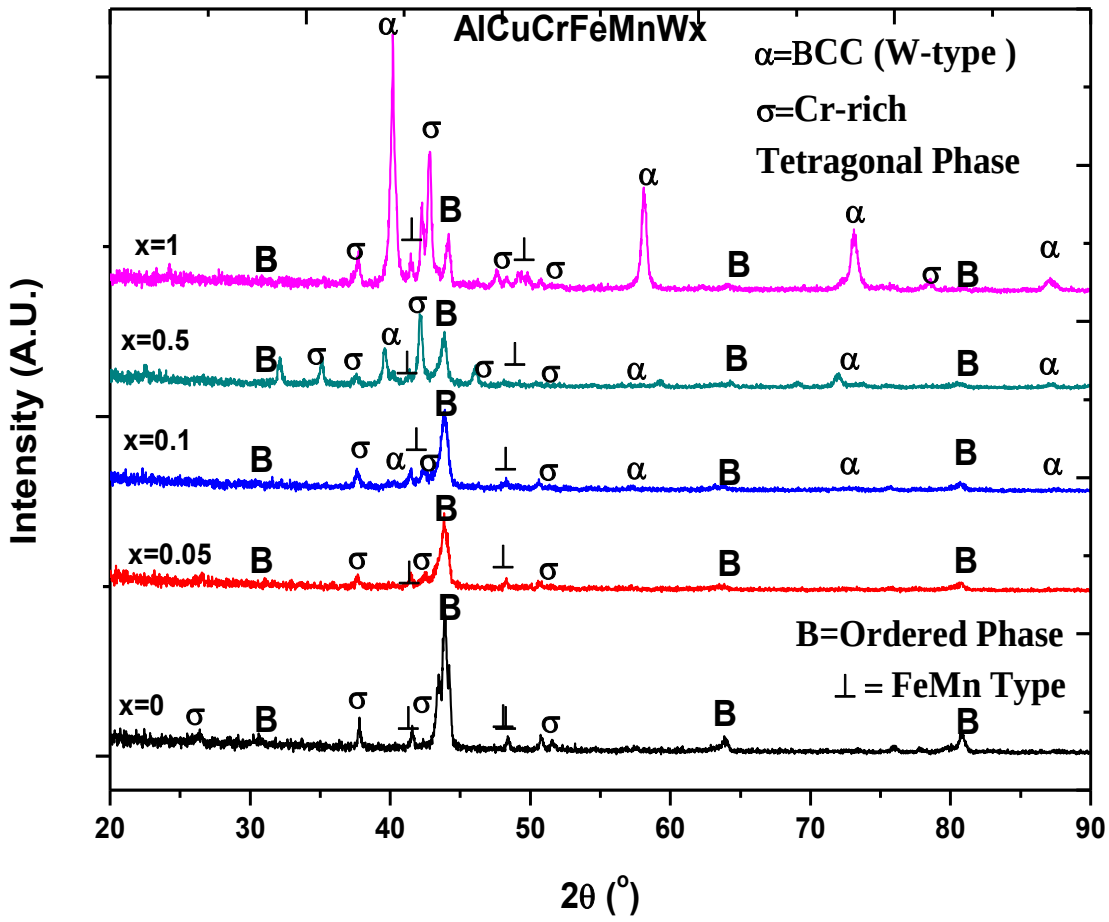

Fig. 5.1: XRD patterns of AlCuCrFeMnW$_x$ (x= 0, 0.05, 0.1, 0.5 & 1.0 mol) HEAs after SPS

Table 5.2 summarizes XRD analysis conducted including the lattice parameter and phase fraction of constituent phases, crystallite size and lattice strain in the sintered AlCuCrFeMnW$_x$ (x= 0, 0.05, 0.1, 0.5 & 1 mol) HEAs. Instrumental broadening was corrected using a single crystalline Si substrate. Lattice strain ε, was determined by the Eq. 5.1, where β_{hkl} is the full-width half maximum (FWHM) of the spectra peaks.

$$\varepsilon = \beta_{hkl}/4\tan\theta \qquad (5.1)$$

Table 5.2: Lattice parameter, crystallite size, lattice strain and reference intensity ratio (RIR) of $AlCuCrFeMnW_x$ HEAs

Composition	Phases	Phase fraction (RIR)	Lattice Parameter (pm)	Crystallite Size (nm)	Lattice Strain (%)
AlCuCrFeMnW	BCC	0.305	318.14	26.02	0.41
	Sigma	0.422	a=879.66, c=455.82	24.89	0.41
	Ordered	0.198	290.37	19.77	0.50
	FeMn Type	0.083	366.80	25.67	0.40
$AlCuCrFeMnW_{0.5}$	BCC	0.222	317.12	50.12	0.32
	Sigma	0.404	a=879.62, c=456.82	34.98	0.31
	Ordered	0.335	289.12	63.78	0.27
	FeMn Type	0.101	370.88	78.98	0.30
$AlCuCrFeMnW_{0.1}$	BCC	0.212	317.92	58.12	0.30
	Sigma	0.298	a=878.62, c=456.98	64.98	0.29
	Ordered	0.501	287.12	93.78	0.25
	FeMn Type	0.121	368.88	68.98	0.31
$AlCuCrFeMnW_{0.05}$	BCC	0.089	317.92	78.12	0.30
	Sigma	0.283	a=878.62, c=456.98	94.98	0.29
	Ordered	0.687	287.12	123.98	0.25
	FeMn Type	0.134	369.15	88.88	0.31
AlCuCrFeMn	Sigma	0.153	a=868.62, c=466.98	104.98	0.27
	Ordered	0.765	289.12	133.98	0.23
	FeMn Type	0.153	369.88	98.88	0.30

5.2.2 Microstructure characterization by SEM and EDS

Fig. 2 (a-e) illustrates the back scattered electron (BSE) images of AlCuCrFeMnWx (x= 0, 0.05, 0.1, 0.5, 1 mol) HEAs. Although the atomic numbers of the alloying elements are very close, the BSE contrast exposes the existence of four phases.

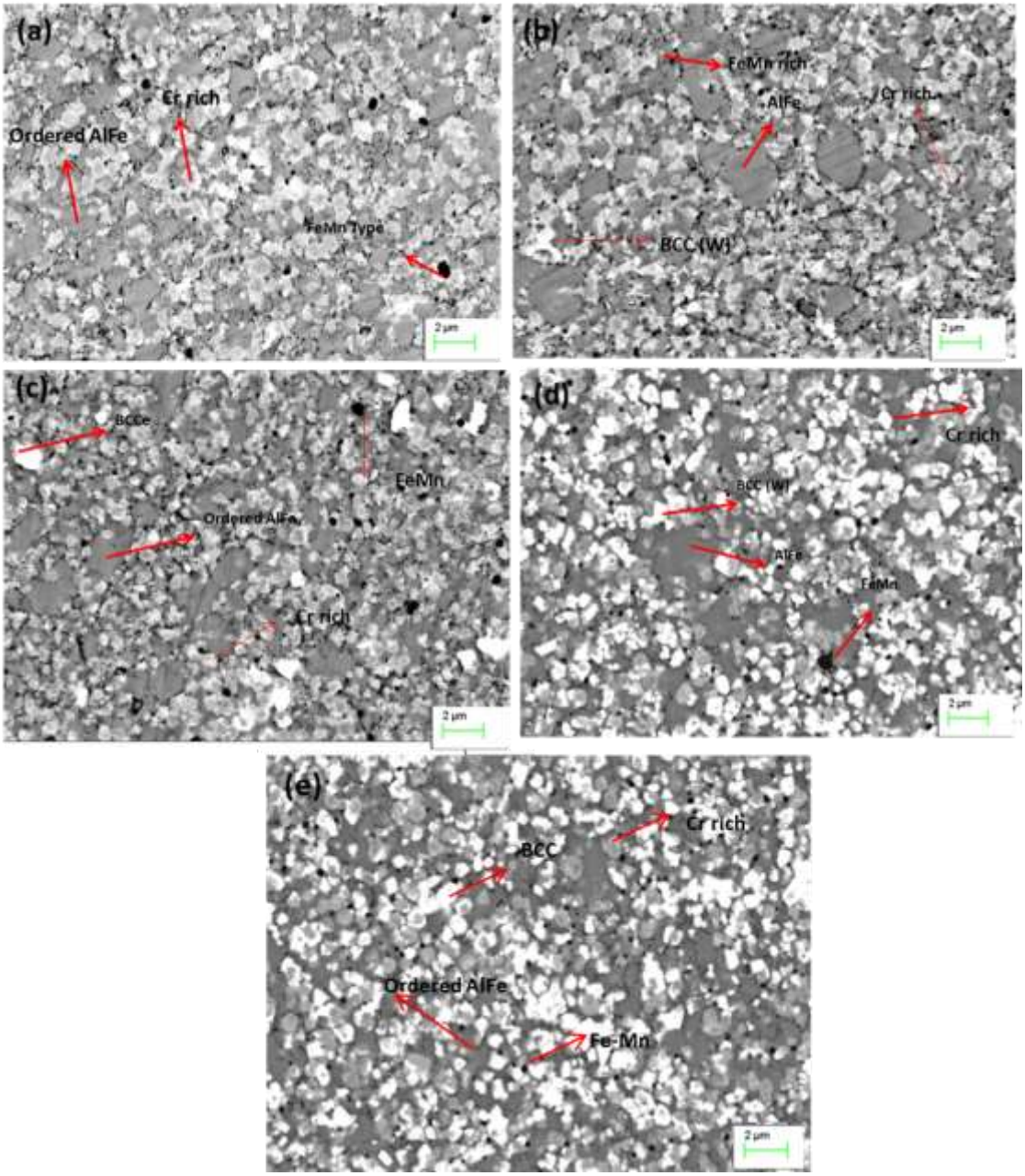

Fig.5.2: SEM back scattered images of AlCuCrFeMnW_x (x=0, 0.05, 0.1, 0.5 and 1mol) HEAs after SPS

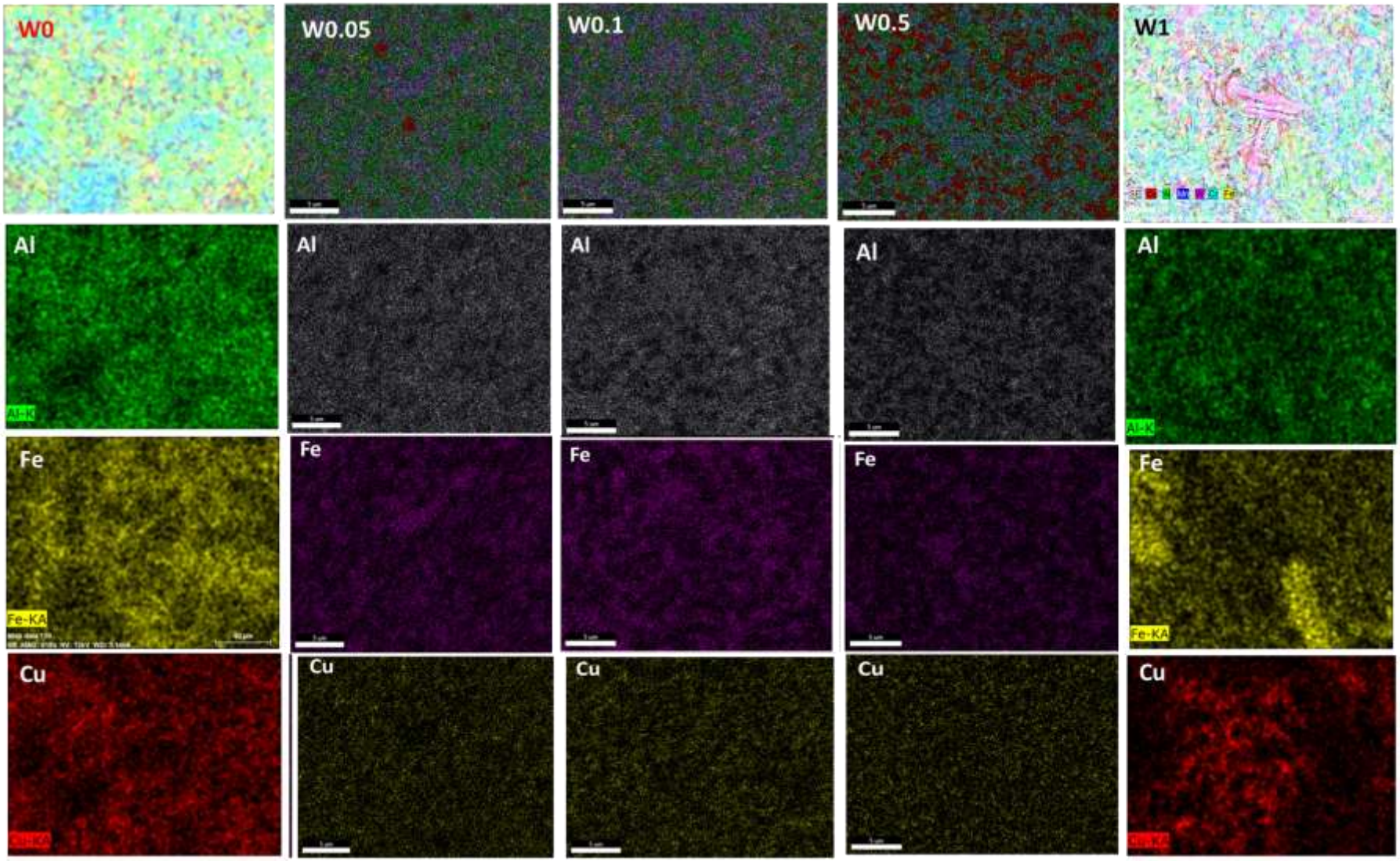
W0
W0.05
W0.1
W0.5
W1
Al
Al-K
Fe
Fe-KA
Cu

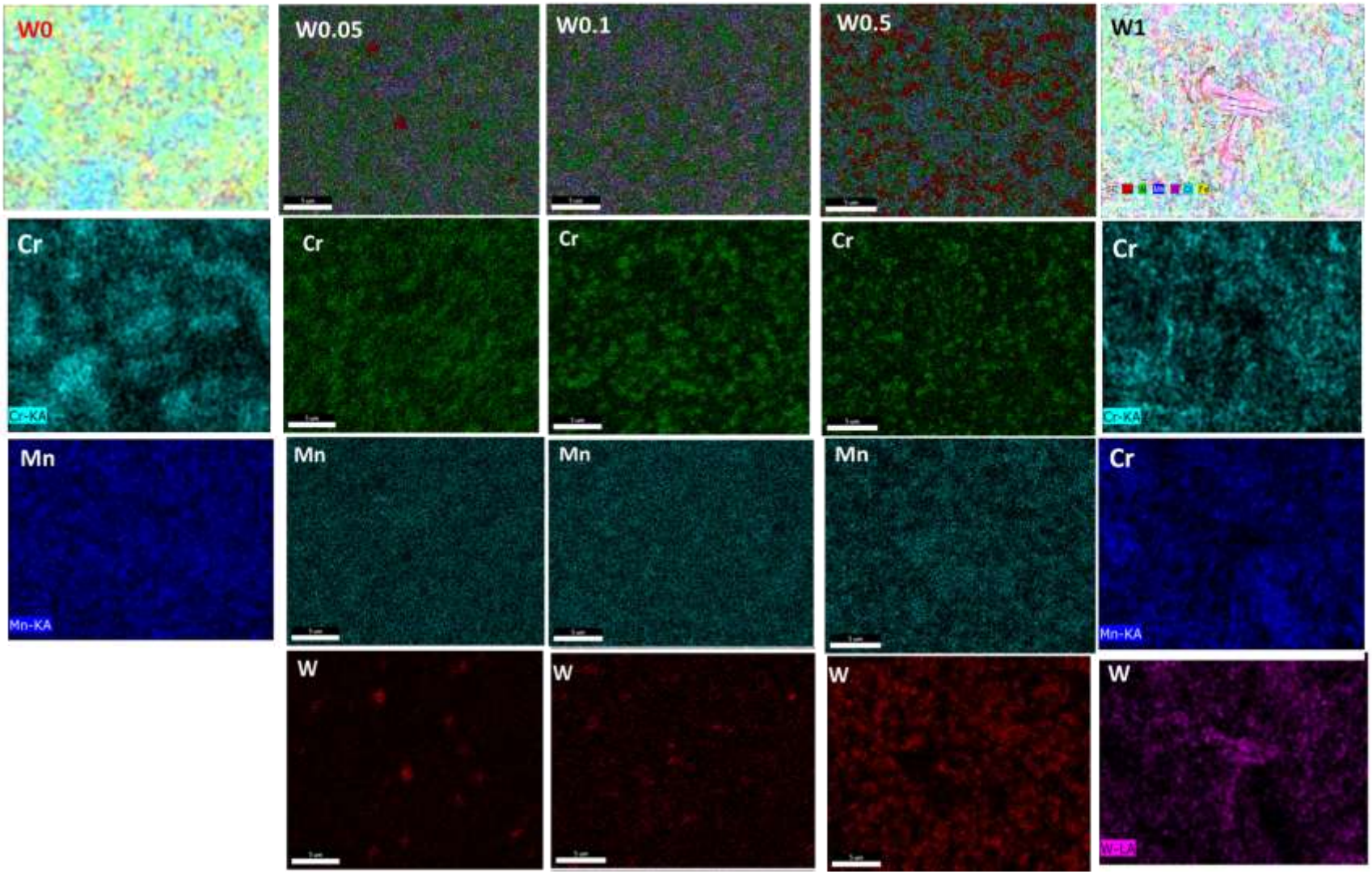

Fig. 5.3 : EDS mapping of AlCuCrFeMnW_x (x=0,0.05,0.1,0.5 and 1 mol) HEA

Based on compositional analysis the coarse grains observed may correspond to AlFe-type ordered BCC phase, the FeMn phase appears to be a distributed network surrounding the ordered phase, Cr-rich grains are possibly Tetragonal closed packed (TCP) phase with small amount of σ phase and a white particle grain with BCC phase is observed. In backscatter images, the heavier metal elements (higher atomic number ***Z***) have a brighter color. In this case, the order of brightness is W first, followed by Cr, Fe, Mn , Cu and Al last.

Figure 5.3 is EDS plot of the elemental distribution of an AlCuCrFeMnW$_x$ (x= 0, 0.05, 0.1, 0.5 & 1 mol) sintered sample. It clearly shows that the Fe-Mn, Fe-Cr and Al-Fe regions form alternately at the grain boundaries, indicating that it continues to penetrate the grains, giving the complex arrangement discussed above. EDS line scans are used to quantify the level of elemental separation between different regions.

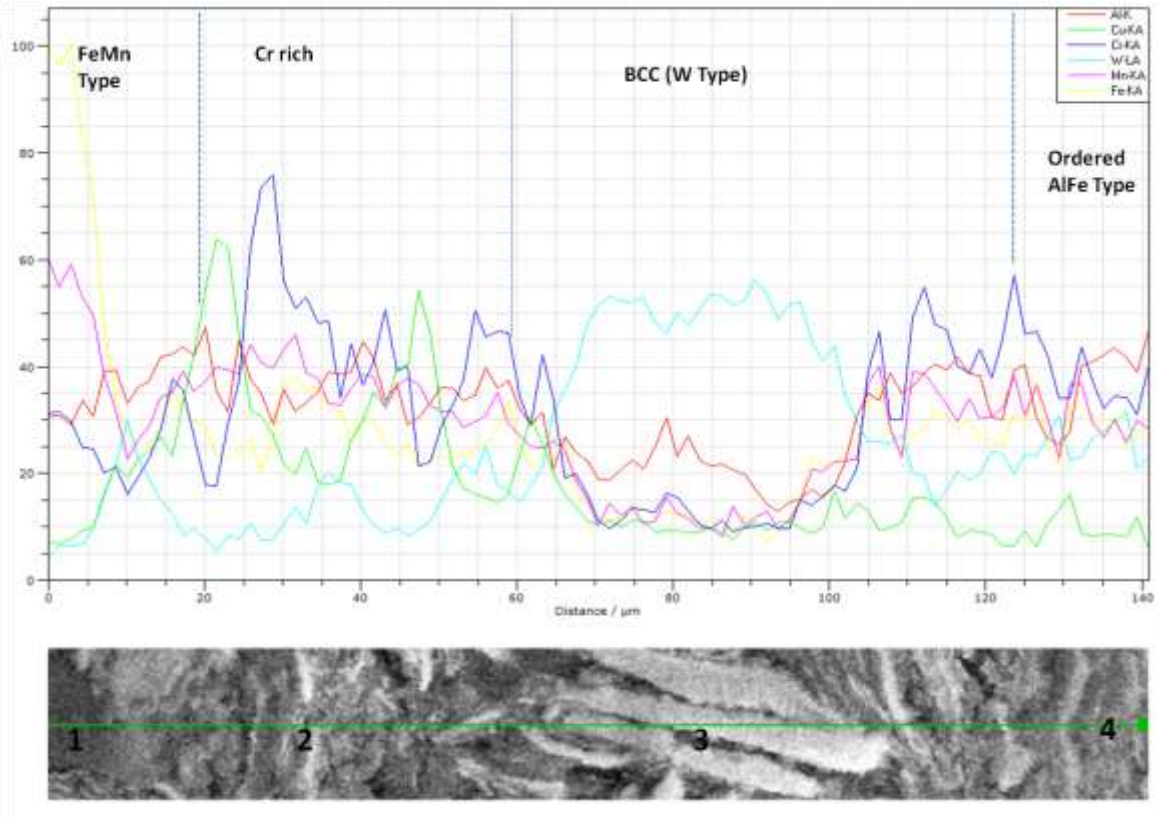

Fig.5.4: EDS line scan of AlCuCrFeMnW HEA

The EDS line scan was used to quantify the level of element segregation between the different regions. The compositional homogeneity of the sample was measured by EDS with line scans

inside a grain and across a grain boundary, respectively, as shown in Fig 5.4. An EDS line scan analysis in confirmed that the darker regions are rich in Fe-Mn (‘1’) and the lighter regions were rich in W (‘3’). The Intermetallics on the modulated structures are the Tetragonal phase which is rich in Cr (‘2’) and the B2 type ordered structure (‘4’).

5.2.3 Transmission electron microscopy

Fig. 5.5(a) shows bright field micrograph of AlCuCrFeMn sintered at 900^{o}C and associated SAED patterns for AlCuCrFeMn HEA which are characterised by irregular shaped tetragonal phase precipitates, a Fe-Mn type phase and ordered BCC phase (SAED, Fig. 5.5(b-c)). Fig.5. 6(a) shows bright field microstructure of AlCuCrFeMn$W_{0.05}$ and associated SAED patterns for AlCuCrFeMn$W_{0.05}$ HEA which are characterized by irregular shaped tetragonal phase precipitates, a Fe-Mn type phase, BCC phase and ordered BCC phase (SAED, Fig. 5.6(b-c)). Fig. 5.7(a) and Fig. 5.8(a) show bright field micrograph of AlCuCrFeMn$W_{0.1}$ and AlCuCrFeMn$W_{0.5}$ sintered at 900^{o}C. SAED pattern are irregular shaped tetragonal phase precipitates, a Fe-Mn type phase for AlCuCrFeMn$W_{0.5}$ HEA and ordered BCC phase for AlCuCrFeMn$W_{0.5}$ HEA (SAED, Fig. 5-8(b-c)). Fig. 5.9(a) shows bright field micrograph of AlCuCrFeMnW sintered at 900^{o}C and associated SAED patterns for AlCuCrFeMnW HEA which are characterised by irregular shaped tetragonal phase precipitates and a Fe-Mn type phase (SAED, Fig. 5.9(b-c)) An absence of an orientational relationship between the FeMn phase and precipitates indicates that the precipitates are incoherent in nature.

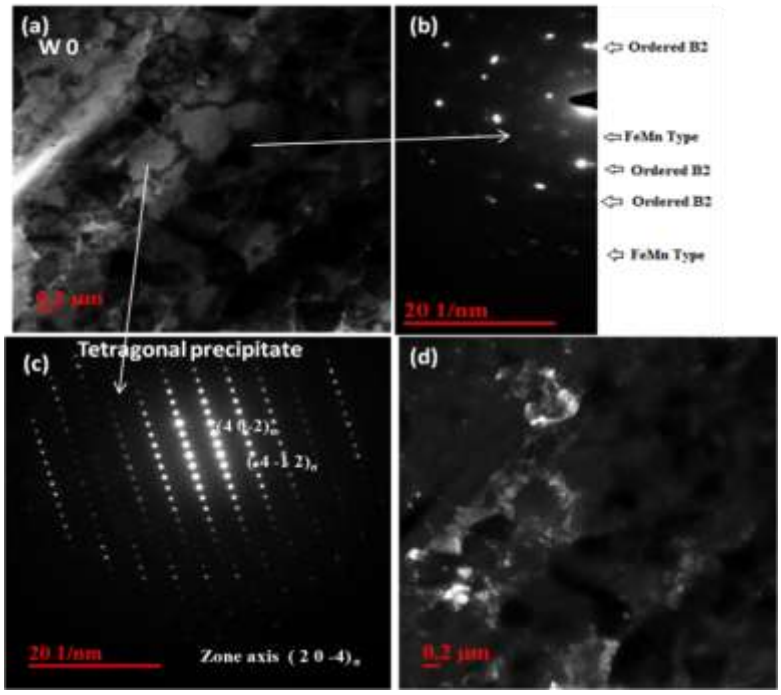

Fig. 5.5: (a) TEM bright field image showing different morphology (b) SAED pattern of FeMn and B2 type phases in TEM image (c) SAED pattern tetragonal phase in TEM image and (d) TEM dark field image of AlCuCrFeMn HEA.

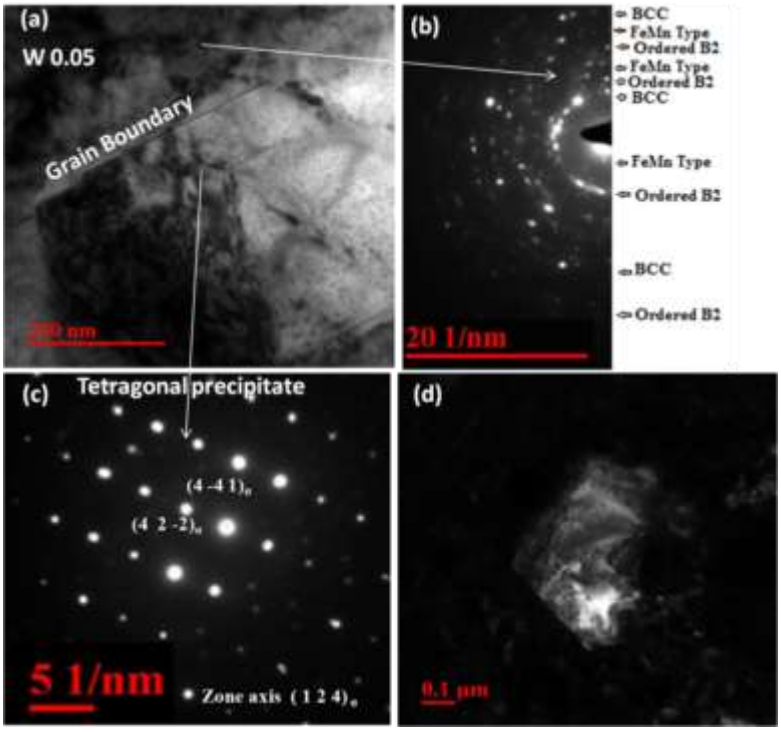

Fig. 5.6: (a) TEM bright field image showing different morphology (b) SAED pattern of FeMn type, BCC and B2 type phases in TEM image (c) SAED pattern tetragonal phase in TEM image and (d) TEM dark field image of AlCuCrFeMn$W_{0.05}$ HEA

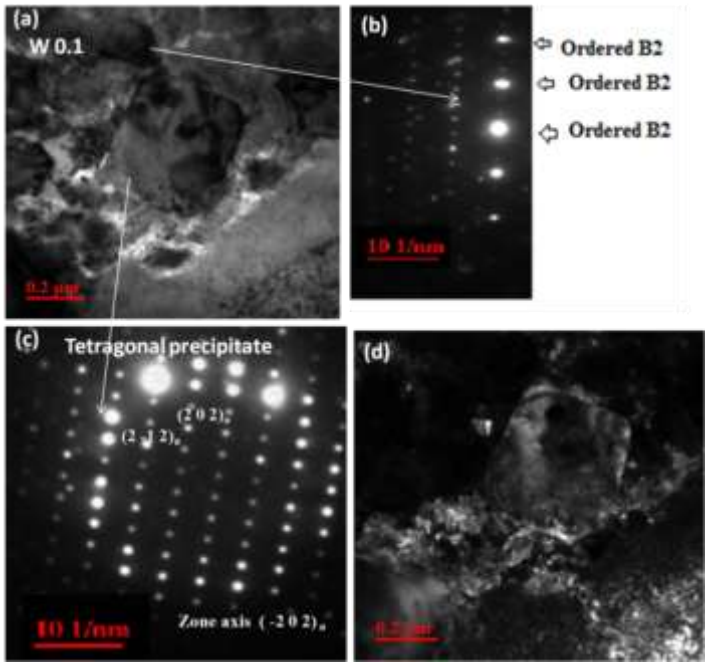

Fig. 5.7: (a) TEM bright field image showing different morphology (b) SAED pattern of FeMn type and B2 type phases in TEM image (c) SAED pattern tetragonal phase in TEM image and (d) TEM dark field image of $AlCuCrFeMnW_{0.1}$ HEA

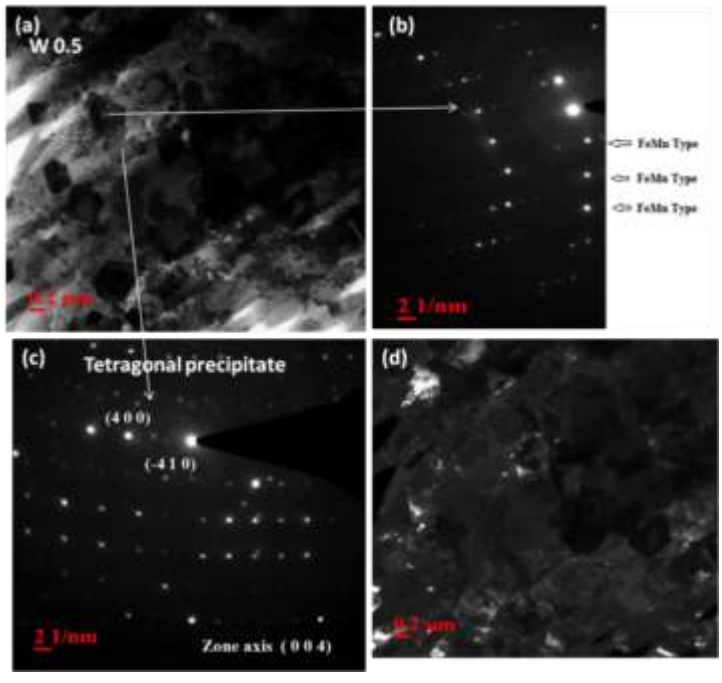

Fig. 5.8: (a) TEM bright field image showing different morphology (b) SAED pattern of FeMn type phase in TEM image (c) SAED pattern tetragonal phase in TEM image and (d) TEM dark field image of $AlCuCrFeMnW_{0.5}$ HEA

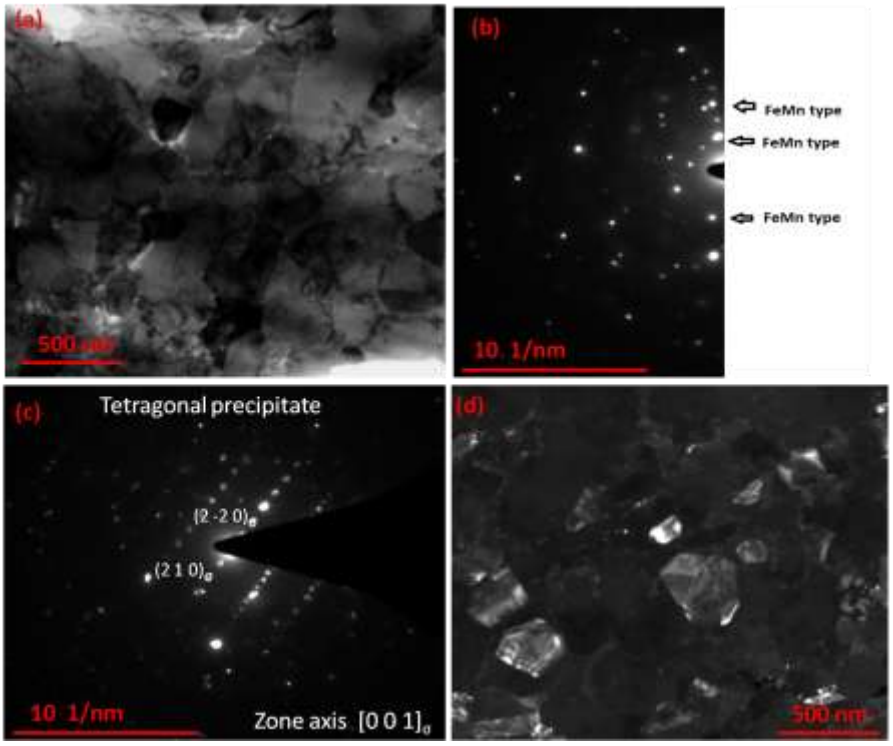

Fig. 5.9: (a) TEM bright field image showing different morphology (b) SAED pattern of FeMn type phase in TEM image (c) SAED pattern tetragonal phase in TEM image and (d) TEM dark field image of AlCuCrFeMnW HEA

The average crystallite size is 30-100 nm, which is comparable to that obtained by the Scherrer formula Determining the discrete crystallite sizes of the BCC, B2, FeMn and σ phases from the dark field image (Fig. 5.5d to Fig. 5.9d) were not possible due to the close proximity of the diffraction rings of these phases.

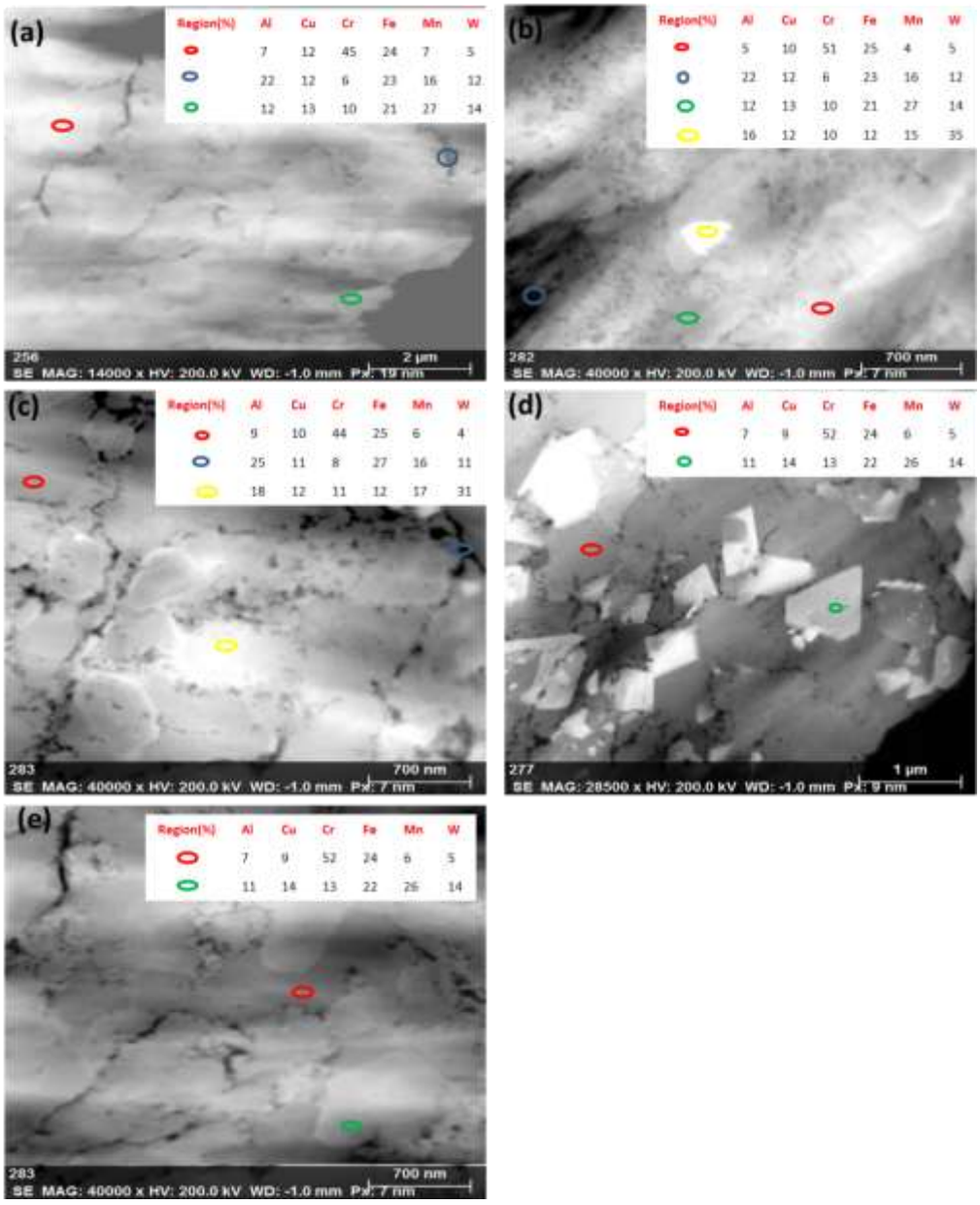

Fig.5.10: STEM image and multipoint EDS analysis of SPSed of (a) AlCuCrFeMn (b) $AlCuCrFeMnW_{0.05}$ (c) $AlCuCrFeMnW_{0.1}$ (d) $AlCuCrFeMnW_{0.5}$ (e) AlCuCrFeMnW HEAs.

Fig. 5.10(a-e) shows the STEM image and multipoint EDS analysis of $AlCuCrFeMnW_x$ (x= 0, 0.05, 0.1, 0.5 & 1 mol) HEAs, which confirm the formation of tetragonal σ type precipitates having high Cr content, FeMn type, BCC and ordered AlFe phases.

5.3 Thermodynamic Considerations in Phase Formation

The microstructural evolution for $AlCuCrFeMnW_x$ (x=0, 0.05, 0.1, 0.5 and 1 mol) HEAs can be described on the basis of thermodynamics parameters. The enthalpy of mixing (ΔH_{mix}) of binary alloy systems of the constituent elements is shown in Table 4.4. Due to the negative enthalpy of mixing between binary elements such as Fe-Mn (-2.9 kJ/mol) and Al-Fe (-11 kJ/mol) the formation of compounds between these elements is thermodynamically more favourable [109]. Thus, major fraction of the microstructure consists of Fe-Mn and Al-Fe ordered phase (Fig 5.2) in low tungsten containing $AlCuCrFeMnW_x$ (x=0, 0.05 & 0.1) HEAs and major fraction of BCC phase (W type) in $AlCuCrFeMnW_{0.5}$ and AlCuCrFeMnW HEAs. In addition to that Table 4.5 shows that AlCuCrFeMnWx HEAs partially fulfills the Zhang's criterion [4] for the formation of simple solid solution; -10kJ/mol<ΔHmix< 5kJ/mol, and $\delta < 4\%$. Thus the large atomic size difference (δ) leads to solid solution as well as intermetallics in $AlCuCrFeMnW_x$ HEAs.

Electronegativity is a tendency of an atom to attract an electron and according to the Hume-Rothery rules and high electronegativity of a solute tends to form intermetallic compounds [58]. In, HEAs the electronegativity difference (ΔX) is calculated by the composition of the HEA and not by lattice type, and is given by Eq. 5.2.

$$\Delta X = \sqrt{\sum_{i=1}^{N} c_i \, (X_i - X_{avg})^2} \qquad (5.2)$$

Where, X_i is the Pauling electronegativity for the i_{th} element and $X_{avg} = \sum_{i=1}^{N} c_i \, X_i$.

Table 5.3: Thermodynamic parameters of $AlCuCrFeMnW_x$ (x= 0, 0.05, 0.1, 0.5 & 1.0 mol) alloys

Composition	**ΔH_{mix} (KJ/mol)**	**ΔS_{mix} ($JK^{-1}mol^{-1}$)**	**Tm (K)**	**Ω**	**δ (A^o)**	**Electronegativity (ΔX)**
AlCuCrFeMn	-1.76	13.38	1561	11.48	5.55	0.252
$AlCuCrFeMnW_{0.05}$	-1.51	13.67	1582	14.48	5.50	0.256
$AlCuCrFeMnW_{0.1}$	-1.28	14.16	1600	17.63	5.40	0.262
$AlCuCrFeMnW_{0.5}$	0.31	14.65	1746	82.51	5.24	0.269
AlCuCrFeMnW	-1.54	14.79	1909	18.20	4.98	0.275

The role of electronegativity on the phase stability of HEAs was described by Dong et al. [57] showing that a topologically closed packed (TCP) structure is stable in HEAs where $\Delta X > 0.133$. Table 5.3 summarizes the values of ΔX for alloys in these studies, $AlCuCrFeMnW_x$ alloys having a range of ΔX is 0.252 to 0.275. Thus, it is clear from the results that electro-negativity difference plays an important role in stabilization of TCP phases (see in Fig. 5.5 to Fig 5.9).

It is believed that ΔH_{mix} and δ are important parameters for the stability of solid solution, which has been reflected in most of the criteria used. Valance electron concentration (VEC) seems to correlate well with the crystalline structure of HEA, FCC structure consistently associated with high VEC value and the low VEC value provides a BCC structure [79]. Tsai et al. [59] have used VEC alongside compositional considerations to predict σ formation in HEAs, while others have compared instances of ordered phase formation (including topologically close-packed phases, TCPs) against the average value of the d-orbital energy level and ΔX. It has been proposed that ΔX is also a sign of elementary segregation in casting and sintering.

5.4. Thermal Behavior of Bulk Samples

Fig 5.11 shows the DSC curves over a temperature range of ambient to 1000^{o}C for the HEAs $AlCuCrFeMnW_x$ (x=0, 0.05, 0.1, 0.5 and 1 mol) HEAs. In contrast, the low W-containing and AlCuCrFeMn HEA show to be having two endothermic peaks at 812^{o}C, 849^{o}C and $AlCuCrFeMnW_{0.05}$ HEA show at 970^{o}C, 968^{o}C, respectively. $AlCuCrFeMnW_x$ (x= 0.1, 0.5 and 1 mol) HEAs appears to be having endothermic peaks at 919^{o}C, 968^{o}C and 918^{o}C respectively.
With reference to the binary phase diagrams for Fe-Cr [110] it is noted that the σ phase decomposes at 830^{o}C and the AlFe phase melting point is 1080 ^{o}C. It is likely that the endothermic peaks in the heat flow curves for AlCuCrFeMnWx HEAs is a combined effect of the melting of AlFe phase and decomposition of σ phase.

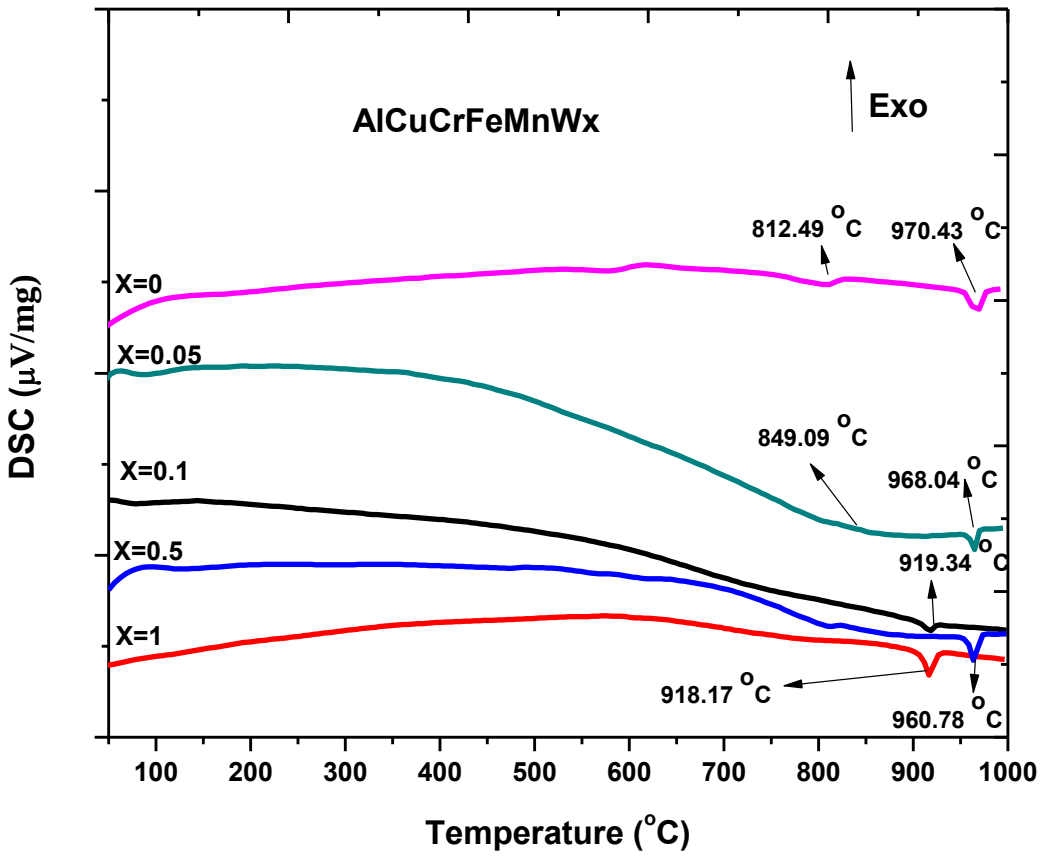

Fig 5.11: DSC scan of SPSed $AlCuCrFeMnW_x$ (x=0, 0.05, 0.1, 0.5 and 1 mol) HEAs at scan rate of 10°C

Fig. 5.12 (a) shows the DSC curves over a temperature range of ambient to 1000°C for the equimolar AlCuCrFeMnW HEA. This HEA appears to behaving endothermic peaks at 918.17°C, 925.23°C and 936.11°C with three different heating rates of 10 K/min, 20 K/min and 30 K/min respectively. In order to evaluate the thermal stability (crystallisation behaviour) of HEA, the DSC tests are carried out. Figure 5.12 (a) shows a typical DSC curve for sintered AlCuCrFeMnW HEA with different heating rates. It can be seen that the crystallization temperature (T) increases to a higher value as the heating rate increases due to the impact of the dynamic heating factor. In addition, depending on the maximum peak temperatures of the DSC curve at different heating rates, the apparent activation energy of the crystallisations can be obtained using the Kissinger relationship. In addition, the Kissinger equation is:

$$\ln(\beta/T^2) = -E/RT + \text{constant} \quad (5.2)$$

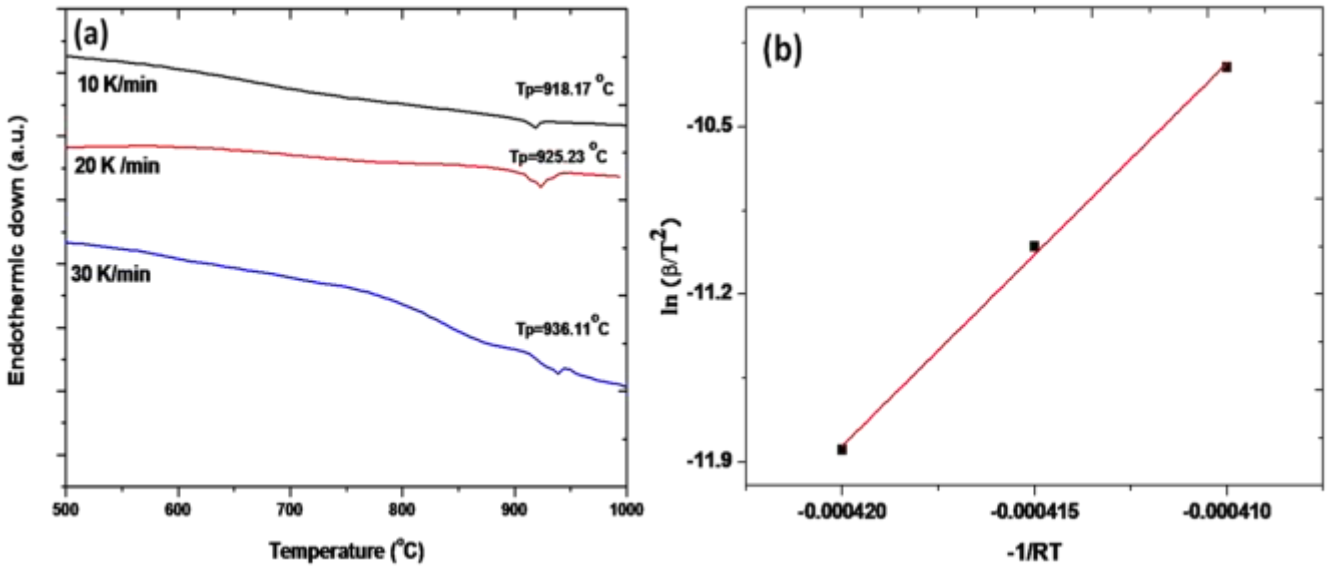

Fig. 5.12: (a) DSC curves of AlCuCrFeMnW HEA with different heating rates (b) Kissinger plots of $\ln(\beta/T^2)$ versus (-1/RT) obtained from continuously heating DSC scans

where β is the heating rate, E is the apparent activation energy for the process, R is the gas constant and T is a specific absolute temperature such as crystallisation temperature or peak temperature, which can be measured at selected heating rates β. By plotting $\ln(\beta/T^2)$ versus -1/(RT), a linear relationship with the slope of E will be obtained, in which E is the apparent activation energy of the whole reaction. Based on these, the Kissinger plots are shown in Fig. 5.12(b). The above mentioned activation energy E for AlCuCrFeMnW HEA in this work is 160.2 kJ mol^{-1}, which indicates that the synthesised sintered alloy have considerable crystallisation resistance.

Thus to summarized that bulk $AlCuCrFeMnW_x$ HEAs is successfully synthesized by spark plasma sintering. Microstructure of present HEAs consists of major AlFe type ordered phase, BCC phase and FeMn phase with some minor peaks of σ phase. Mechanical properties of these HEAs such as hardness, compressive strength and room temperature creep are discussed in next chapter.

.**Chapter 6**

MECHANICAL PROPERTIES AND ROOM TEMPERATURE CREEP BEHAVIOR OF AlCuCrFeMnW_x (x=0, 0.05, 0.1, 0.5 and 1mol) HEAs

This chapter discusses the Mechanical properties, room temperature creep and structure property correlation of AlCuCrFeMnW_x (x=0, 0.05, 0.1, 0.5 and 1mol) HEAs.

6.1 Mechanical Properties of AlCuCrFeMnW_x HEAs

6.1.1 Microhardness

Microhardness is calculated using Vickers micro-hardness tester on AlCuCrFeMnW_x HEAs with indentation load of 200gf and dwell time as 15 sec and the Vickers microhardness value is repeated at least five times across the polished sample surface. Microhardness value was calculated using Vickers micro-hardness tester on AlCuCrFeMnWx HEAs and Vickers microhardness test was repeated five times across the polished sample surface. The hardness of AlCuCrFeMnWx (x= 0, 0.05, 0.1, 0.5 mol) were determined to be 633.5±11.5 HV to 780±12 HV as the tungsten content are increases. (Fig. 6.1)

The hardness shows is nearly linear increase with increases tungsten content and it can be expressed as:

$$Y\ (HV) = 281.91\ X + 629.67 \qquad (6.1a)$$

where Y is the micro-hardness value in HV, and X is the W content in mol.

An experiential relationship between the yield strength (σ_Y) and hardness value is: (Table 6.1)

$$\sigma_Y\ (MPa) = 3\ X\ H_V(HVN) \qquad (6.1b)$$

Engineering stress-strain curves under compression mode for the present HEAs having different amount of the refractory element (W) are shown in Fig. 6.2 and the results of fracture strength under compression are shown in Table 6.1. It is noticed that fracture strength of present alloy system has a noticeable effect with increasing tungsten content. The tungsten free alloy (W_0) has low yield strength of 1010 MPa. The $W_{0.05}$ alloy shows very similar behavior, however its fracture strength under compression value (1120 MPa) is greater than the W_0 alloy. Fracture strength under compression of the $W_{0.1}$ alloy is 1250 MPa, but increase rapidly to 1510 MPa for $W_{0.5}$ alloy. The development of the disordered BCC phases and tetragonal phases expressively

improves the hardness and strength of the present HEAs. Generally, energy absorbed before fracture in compression is called toughness. So according to Fig. 6.2 toughness of present HEAs are increases with increases of tungsten content.

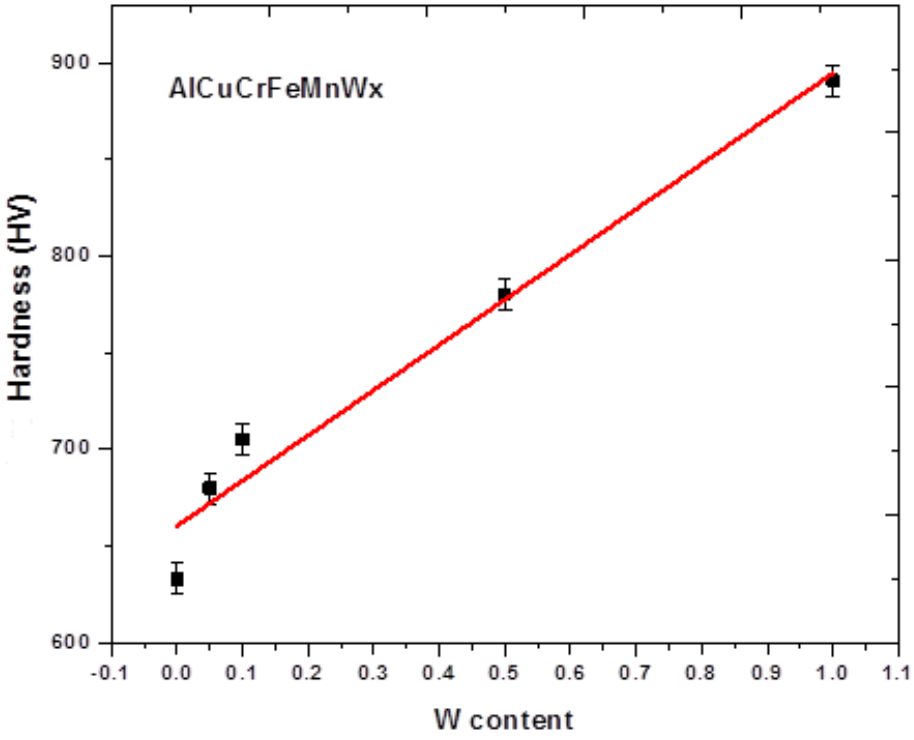

Fig. 6.1: Microhardness variation as a tungsten content in $AlCuCrFeMnW_x$ (x=0, 0.05, 0.1, 0.5 & 1 mol) HEAs

6.1.2 Compressive strength

Engineering compressive engineering stress-strain curves for the $AlCuCrFeMnW_x$ (x= 0, 0.05, 0.1, 0.5 and 1 mol) HEAs having varying content of the refractory element (W) are shown in Fig. 6.2. The fracture strength under compression (σ_f) are summarized in Table 6.1. It is observed that compressive behavior of current alloy system has a noticeable effect by increasing W content. The tungsten free alloy (W_0) has low yield strength of 1010 MPa. The $W_{0.05}$ alloy shows very comparable behavior, however its yield strength value (1120 MPa) is marginally higher than the W_0 alloy. Furthermore, increase in the W content results in substantial strengthening: the fracture strength under compression of the $W_{0.1}$ alloy are 1250 MPa, but increase rapidly to 1510 MPa, in the case of $W_{0.5}$ alloy.

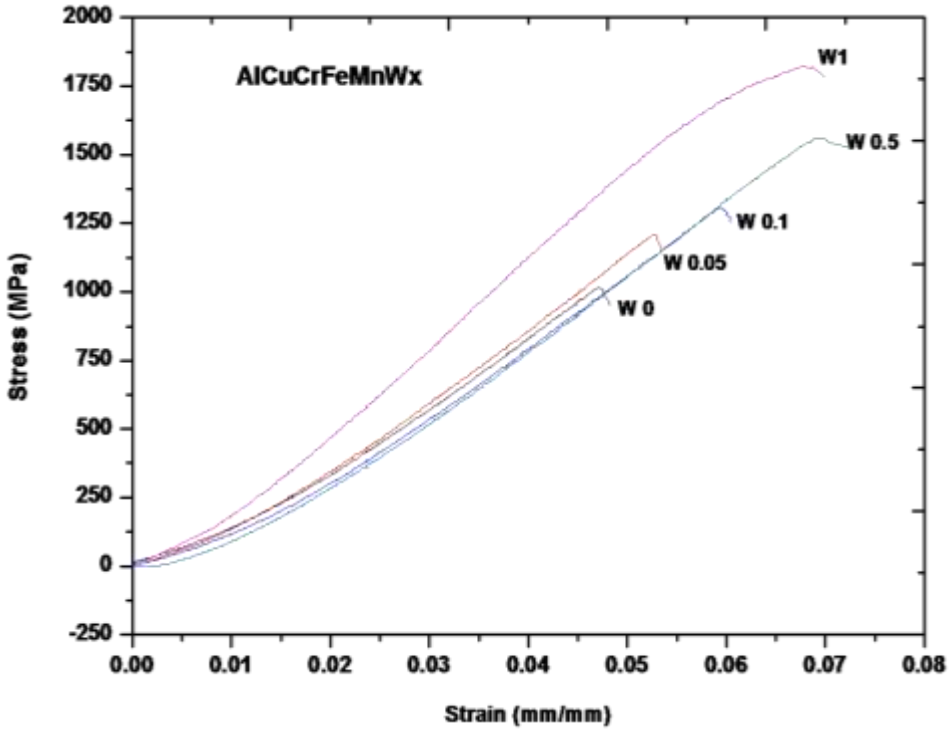

Fig. 6.2: Engineering stress-strain curve of AlCuCrFeMnWx (x=0, 0.05, 0.1, 0.5 & 1mol) HEAs

Table 6.1: Microhardness (HV), microhardness (GPa), yield strength (GPa) and elastic modulus (GPa) of AlCuCrFeMnWx (x= 0, 0.05, 0.1, 0.5 & 1mol) HEAs

Composition	Micro-hardness (HV)	Micro-hardness (GPa)	yield strength (σ_y) (GPa)	Compressive strength (σ_f) (GPa)
AlCuCrFeMn	633	6.178	2.059	1.010
AlCuCrFeMn$W_{0.05}$	680	6.669	2.223	1.120
AlCuCrFeMn$W_{0.1}$	705	6.914	2.304	1.250
AlCuCrFeMn$W_{0.5}$	780	7.649	2.549	1.510
AlCuCrFeMnW	891	8.781	2.90	1.820

And last at the highest tungsten content i.e. AlCuCrFeMnW fracture strength under compression is 1820 MPa. With the increase amount of the W, the development of the disordered BCC phase expressively improves the hardness and strength of the present HEAs.

6.2 Strengthening Mechanism

As discussed in the previous chapters, the $AlCuCrFeMnW_x$ powder contains a relatively small amount of FCC phase compare to BCC phase. After sintering, a minor volume fraction of the BCC phase is converted into a BCC phase and other complex phases developed. This is due to the over-saturation of all the elements in a single BCC phase in the mechanically alloyed powder which determines the formation of a complex phase after sintering. Interestingly, the $AlCuCrFeMnW_x$ alloys form nanocrystalline bulk products due to the high heating rate of 100^oC / min inherent in SPS processes. The high heating speed prevents the formation of coarse grain and high density.

The excellent compressibility of present HEAs is due to the second stage hardening (tetragonal phase) and to the strengthening of the solution (W rich). As presented in Figure 6.2, the alloys W_0 and $W_{0.05}$ show good plasticity due to existing of ordered phases, but in the case of the $W_{0.1}$, $W_{0.5}$ and W1 alloys, its shows excellent compressive strength due to the formation of brittle phases. For an HEA, each atom is considered to be a solute atom that occupies random points of the lattice. The differences in size and other properties of these solute atoms lead to severe distortion of the lattice. The interaction between different atoms leads to the formation of a local elastic stress field that prevents the movement of dislocations, with a consequent increase in strength. In the $AlCuCrFeMnW_x$ alloys, the hardness increases with increasing W content is shown in Figure 6.1.

Subsequently, fracture mechanism of $AlCuCrFeMnW_x$ alloy is investigated in Figure 6.3. As shown in figure 6.3a and 6.3b for the alloys W_0 and $W_{0.05}$, the ordered phases are produced almost simultaneously during the deformation. The formation of large amounts of dislocation and slip deformation will leads due to good plasticity are shown in Figure 6.3a and 6.3b. For the $W_{0.1}$, $W_{0.5}$ and W1 alloys, the rigid and hard tetragonal phase is still elastically deformed and hinders the movement of dislocations when the BCC phase yields just in the initial deformation phase. When further compression deformation occurs, the tetragonal phases produce cracks and

crack propagation in the sample occurs rapidly, resulting in a brittle fracture are shown in Fig.6.3c, 6.3d and 6.3e. These results are show that there is not any plastic deformation, but a brittle fracture directly for the tetragonal phase. As a consequence, the tetragonal phase interruptions determine the formation of fine particles rather than dimples.

The Vickers micro-hardness value of equimolar AlCuCrFeMnW alloy shows maximum hardness of 891 ± 12 HV, then the hardness value decreases and lowest hardness of AlCuCrFeMn HEA was 633 ± 11.50 HV. The high hardness value is due to the combined effect of grain size strengthening, solid solution strengthening and strengthening by precipitation. Using the Tabor equation [111], $H = 3\sigma_{flow}$, where H is the hardness and σ_{flow} is the slip/yield flow of the material. For AlCuCrFeMn, $AlCuCrFeMnW_{0.05}$, $AlCuCrFeMnW_{0.1}$, $AlCuCrFeMnW_{0.5}$ and AlCuCrFeMnW, σ_{flow} is calculated as 2.059, 2.223, 2.304, 2.549 and 2.90 GPa respectively. Obviously, the microstructure of the sintered samples contains larger ultrafine grains and smaller nanocrystalline grains. Furthermore, it is a four-phase structure composed of two solid solutions (BCC and B2). Thus, the complete flow stress is calculated by combination of lattice stress friction mobile dislocations, strengthening due to intersecting dislocations (Taylor reinforcement), grain refinement (Hall-Petch strengthening) and strengthening of the solid solution. It is suggested that the following equations can be used to determine the different mechanism contributing to the flow stress is [112]:

$$\sigma_{flow} = \sigma_{i+} \Delta\sigma_{SH} + \Delta\sigma_{HP} + \Delta\sigma_{SS} \quad (6.2)$$

σ_i is the frictional stress and it is present in the lattice of all elements. Because these HEAs have recently issued new classes of alloys, as per the authors' knowledge, their friction stress data are not available in the literature. Frictional stresses calculated by rule of mixture shown in Table 6.2 [59].

$\Delta\sigma_{SH}$ (strain hardening) is the strengthening of relatively large grains due to the intersection of dislocations during deformation [112].

$$\Delta\sigma_{SH} = M\alpha Gb\rho^{1/2} \quad (6.3)$$

Table 6.2: Frictional stress (σi), strain hardening ($\Delta\sigma_{SH}$), grain size strengthening ($\Delta\sigma_{HP}$), solid solution strengthening ($\Delta\sigma_{SS}$) and yield strength of $AlCuCrFeMnW_x$ (x= 0, 0.05, 0.1, 0.5 and 1 mol) HEAs

	Frictional stress (σ_i) MPa	Strain hardening ($\Delta\sigma_{SH}$) MPa	Grain size strengthening ($\Delta\sigma_{HP}$) MPa	Solid solution strengthening ($\Delta\sigma_{SS}$) MPa	Yield Strength Total (MPa)
AlCuCrFeMn	180	1090	502	267	2039
$AlCuCrFeMnW_{0.05}$	195	1170	591	284	2240
$AlCuCrFeMnW_{0.1}$	198	1201	609	290	2298
$AlCuCrFeMnW_{0.5}$	209	1291	659	301	2460
AlCuCrFeMnW	230	1408	724	329	2810

M is the Taylor factor (both FCC and BCC materials are 3.06) and α is the material-specific correction factor. It is assumed that α is unity because of novelty of HEAs. G is the shear module, b is the Burger vector and ρ is the dislocation density. The elastic modules (E) of these alloys (calculated from the rule of mixture shown in Table 6.1) are based on the following assumptions that the alloy in the current study is Isotropic. Shear modulus (G) is determined by G = E / 2 (1 + ν), where ν is the Poisson ratio (0.33). The Burgers vector for a BCC-based lattice is calculated as, b = (a / 2) ⟨110⟩. Dislocation density (ρ) is calculated by [146]:

$$\rho = \frac{2\sqrt{3}\varepsilon}{db} \tag{6.4}$$

In this Eq. (6.4), ε is lattice strain, d is grain size (nm) calculating by XRD, b is the Burgers vector (nm). With all the above parameters, $\Delta\sigma_{SH}$ for strain hardening (Taylor hardening) arising from large dislocation densities present in this material is estimated in Table 6.2 using Eq. (6.3).

$\Delta\sigma_{HP}$ is the Hall-Petch strengthening or grain size dependent strengthening [113].

$$\Delta\sigma_{HP} = K_{HP}d^{-0.5} \tag{6.5}$$

K_{HP} is the Hall-Petch constant and 'd' is the average particle size measuring from SEM images (Fig. 5.2) and table 6.2 estimates the Hall-Petch strengthening involvement.

$\Delta\sigma_{SS}$ is the contribution of the solid strengthening of the solution. Since both phases (BCC and B2) are basically solid solutions made up of all the participating elements, this component is also important. In the conventional binary solid solution, the elastic interaction between the dislocations and the stress field caused by the solute atoms determines the appropriate strengthening mechanism, and all models of strengthening mechanism of the solid solution are effective for the binary solid solution [113-114]. Because HEA is a complex concentrated alloy, Senkov et al. [91] proposed the following formula to estimate the strengthening of the solid solution of a concentrated system:

$$\Delta\sigma_{SS} = AG\epsilon^{4/3}C^{2/3} \quad (6.6)$$

In this equation 6.6, A is a dimensionless number of about 0.1. C is the atomic concentration of the solute (0.16), G is the shear module of the alloy, and ε is the strain of the lattice caused by the solute calculating using XRD value. Based on the calculation and formula above (eq. 6.2), the total contribution of various reasonable mechanisms to the flow σ_{flow} is from 2.039 to 2.460 GPa to increase the content of W. The Vickers hardness (H) of these HEAs was calculated for increase the W content from 6.178 GPa to 7.469 GPa were given in Table 6.1. Thus, the ratio of these alloys (H / σ_{flow}) is 3.02-3.04. As per Tabor analysis, the ratio between these traditional materials varies from 2.8 and 3.2. Therefore, for these HEAs, the calculated ratio of 3 with respect to the conventional polycrystalline material is approximately the same, indicating that it is reasonable that the mechanisms described above are responsible for achieving the total flow stress. From Table 6.3 it is clear that the Taylor hardening and the strengthening of the grain size are the main strengthening mechanisms of these alloys, which represent almost 80% of the stress of the flow.

It can be seen that $AlCuCrFeMnW_x$ alloys have better hardness and high compressive strength and therefore it can be considered potential candidates for structural application.

6.3 Room Temperature Creep Characteristics of AlCuCrFeMnW$_x$ HEAs

In the previous section, mechanical properties of AlCuCrFeMnWx (x= 0, 0.05, 0.1, 0.5 and 1 mol) HEAs were discussed. Here, we study the creep behavior of HEA at room temperature under different holding loads. In addition, the effect of the strain rate sensitivity on creep is also analyzed.

6.3.1 Creep behavior

Figures 6.3a, b, c, d, e show the typical P-h curves of creep tests for AlCuCrFeMnW$_x$ (x = 0, 0.05, 0.1, 0.5 and 1 mol) HEAs at different peak loads, respectively. To minimize the viscoelastic deformation during the loading segment, high loading rate of 0.5 mN/s were selected.

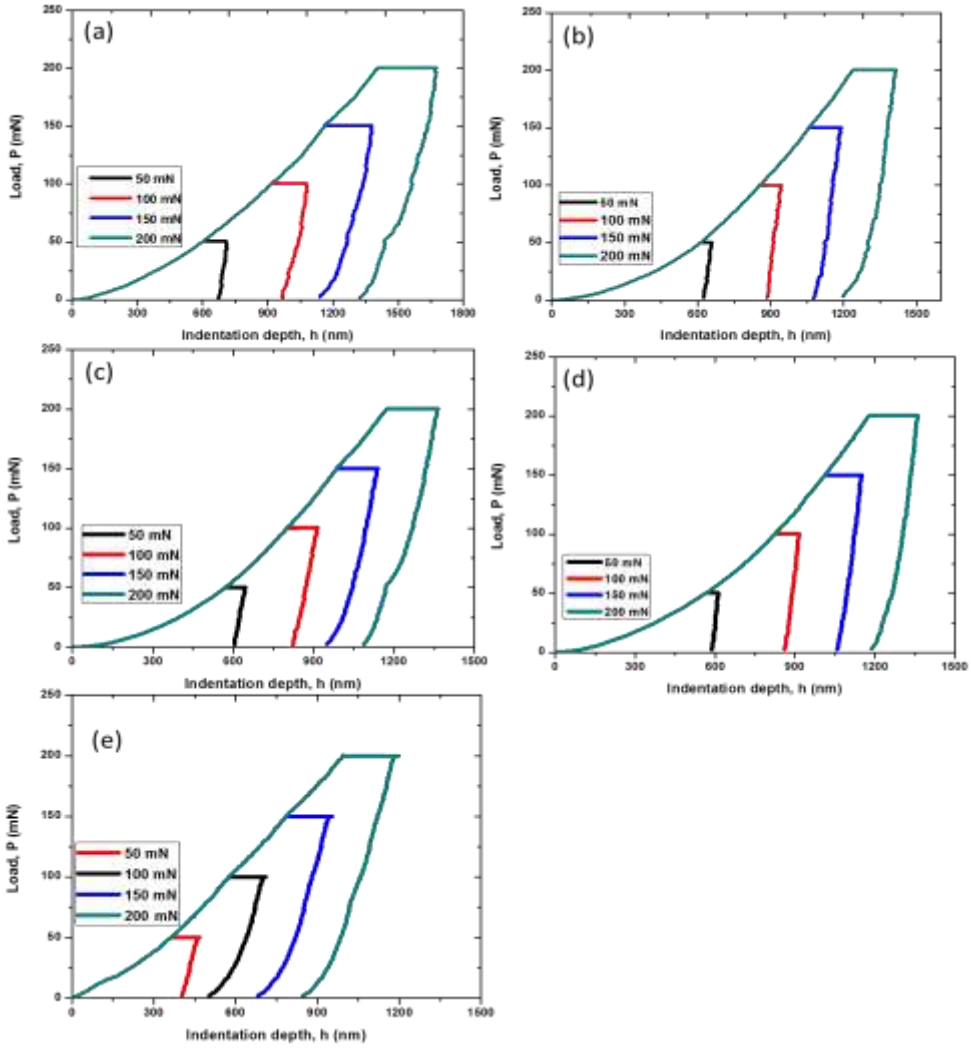

Fig. 6.3: Representative load-displacement curves during the holding stage obtained at four different maximum loads for AlCuCrFeMnWx (x= 0, 0.05, 0.1, 0.5 and 1mol) respectively.

Pop-in events were imperceptible during the loading stage. It is found that for every creep experiment, there is a rapid increase of displacement at the beginning of the holding period followed by a steady-state state at the end of the curves. First, it must be taken into account that the maximum depth of indentation x = 0 before the holding stage is greater than x = 1 HEA under the same load. This shows that AlCuCrFeMn causes the softness of HEA and also reports an increase in hardness as the W content in HEA of $AlCuCrFeMnW_x$ increases (x = 0, 0.05, 0.1, 0.5 and 1mol).

All HEA creep phenomena can even be observed in a holding test of 50 mN at room temperature. Compared to the uniaxial stress / compression test, the stress distribution in nanoindentation is much more complicated even with the diamond indenter, and the maximum shear stress can exceed the yield strength of the sample at extremely shallow displacement. This is essentially the reason why creep occurs in many high-melting materials at room temperature by nanoindentation [115], while in conventional tests the material creeps until the test temperature approaches the melting point of the sample.

The creep behavior of all the samples shows strong load dependence, as shown in Figure 6.4a, b, c, d, and e the relationship between the creep displacement and the holding time can be understood more clearly. It can be found directly that the creep displacement and the creep rates increase with increasing maximum load. The creep curve found here is very similar to the classical creep curve outside the third stage (accelerated creep) because the material will not be a catastrophic failure in the nanoindentation test. The creep curves can also be divided into two distinct stages: transient creep and creep at steady state. In the transient stage, the displacement of the extrusion increases rapidly, but the creep rate rapidly decreases. In the steady state phase, the creep displacement is slow and almost linearly increasing. Creep is a plastic deformation dependent on time, hardness is defined as the resistance to plastic deformation. The creep enhancement of x = 0 is understandable due to the reduced hardness. However, the inherent mechanism of HEA creep may be too complex to be resolved.

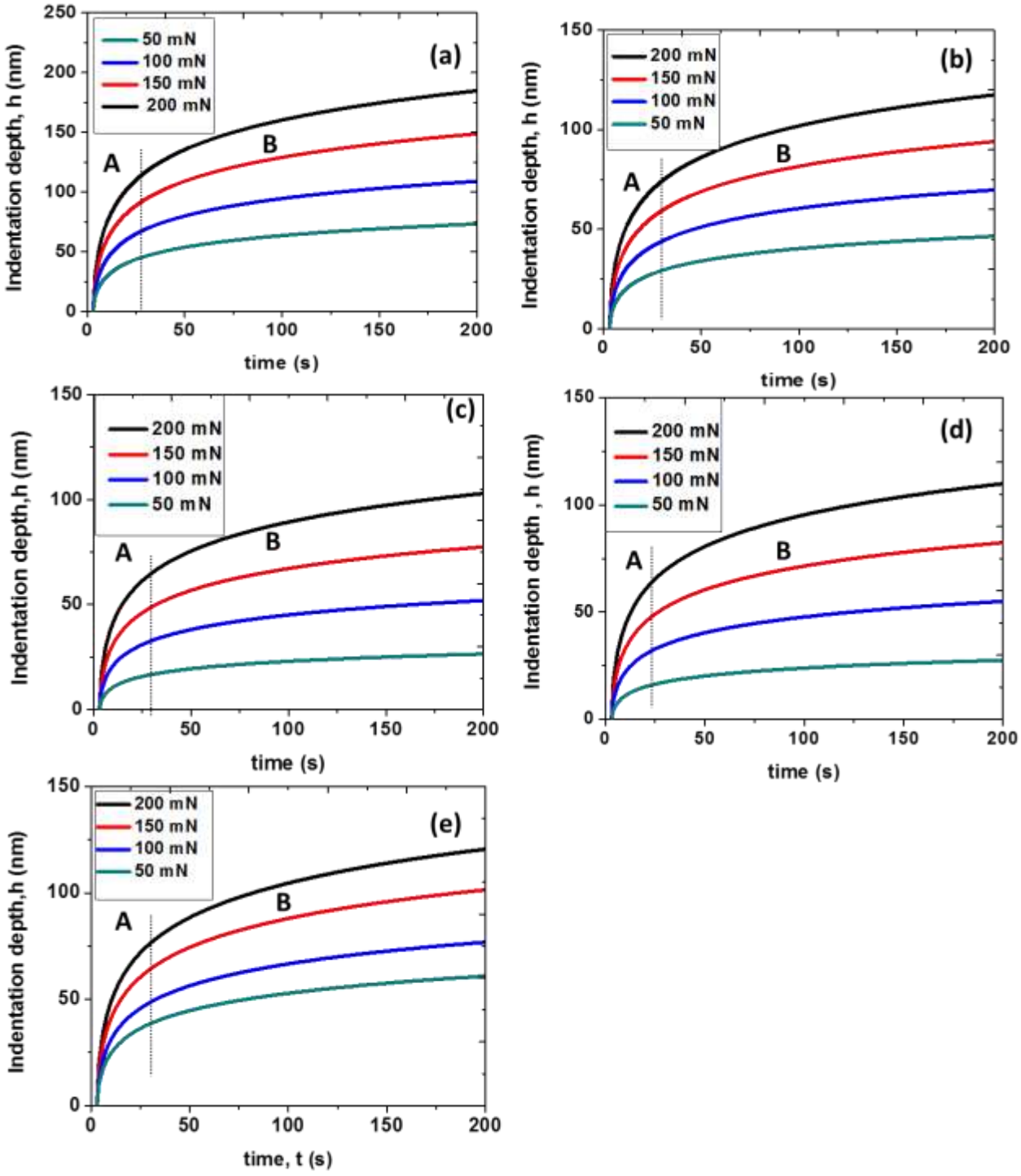

Fig. 6.4: Creep displacements during the holding stage obtained at four different maximum loads for AlCuCrFeMnWx (x= 0, 0.05, 0.1, 0.5 and 1mol) respectively.

Compared with traditional uniaxial tensile/compressive creep tests, where the stress distribution is relatively homogeneous and normally without stress concentration, the stress contribution underneath the indenter is much more complicated [116]. Unlike the traditional creep tests, the final failure of the sample does not occur during nanoindentation creep, when the maximum shear stress could surpass the yielding stress even at extremely shallow depth due to local shear deformation. That might be the intrinsic reason why the creep occurs in many high-melting point materials at room temperature by nanoindentation, whereas materials creep till the testing temperature is close to materials melting point [115-117]. Moreover, the creep behavior of the current alloy shows a strain rate dependence, which could be more clearly revealed between the creep displacement and holding time, as shown in Fig. 6.4.

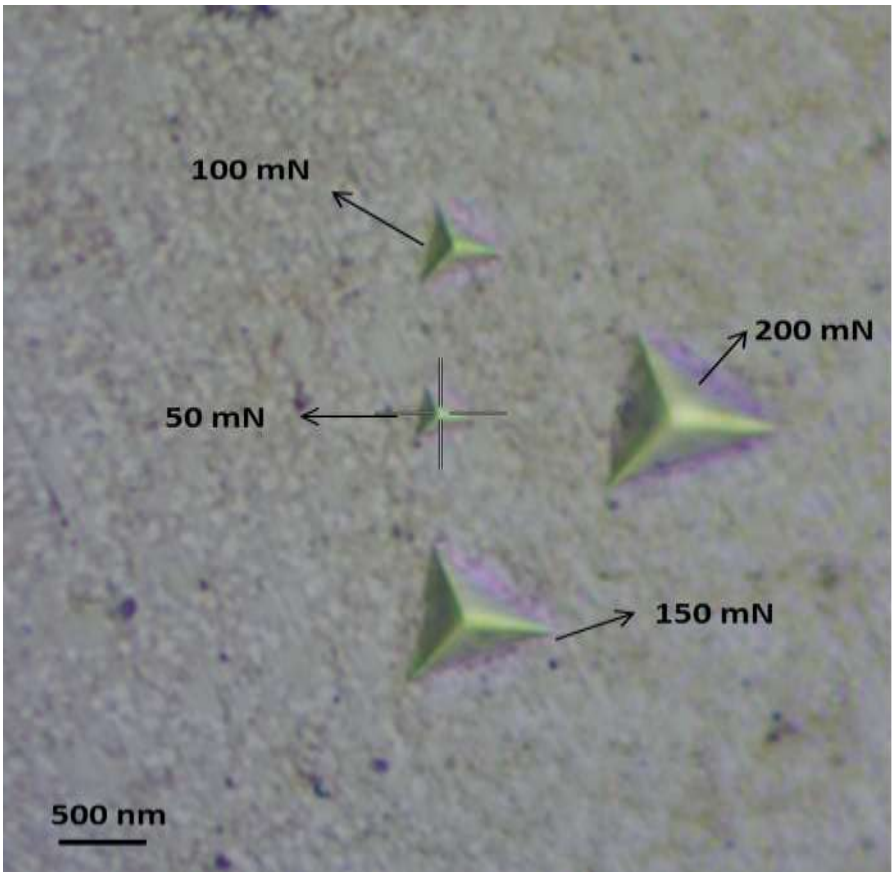

Fig.6.5: Scanning images after nanoindentation of AlCuCrFeMn HEA at an indentation loading rate of 0.5 mN / s with Berkovich indenter

It is noted that the creep displacements and creep rates increase with increasing the strain rates. The strain rate dependence that creep displacement becomes larger with the strain rates could be attributed to the accumulation of visco-plastic deformation related to the dislocation dynamics under higher strain rates [118] and the transformation into larger creep deformation during the holding time [119]. Furthermore, it can be observed that the creep curves captured during nanoindentation are very similar to the classic creep curves obtained in traditional creep tests except the failure stage, where the creep rate is accelerated and materials ultimately fail [120]. Actually, the creep curves could be divided into two different stages as the transient and steady state creeps. For simplicity, the transient creep is denoted as A, and the steady-state creep is denoted as B as exhibited in Fig. 6.4. At A stage, the creep rate declines rapidly, but the creep depth increases dramatically. Then, the creep curves almost linearly ascend with time during B stage [121].

Indeed, the creep behavior is dominated by the strain hardening at A stage and then, transits into the dislocation migration viscous stage. The strain-hardening effect dominates in a very short time, while the visco-plastic stage accounts for most of the creep stage during the holding period. For the sake of vividly elucidating the deformation mechanisms for the AlCuCrFeMn alloy after nanoindentation, in-situ scanning image of the indent at the strain rate of 0.5 mN/s with a depth limit of 2000 nm using a Berkovich tip are typically exhibited in Fig. 6.5. The sample surface uplifts owing to the material pileup, which can be clearly observed around the indent. As an important phenomenon of plastic deformation, the significant pileup of the present alloy suggests that a heavy and highly localized plastic deformation occurs during nanoindentation.

6.3.2 Strain rate sensitivity and stress component

Strain rate sensitivity (SRS) and stress components are crucial for the physical properties of the material. Indentation creep has always been the most widely studied method of SRS in traditional metals. The SRS value can indicate the mode of deformation of the material under indenter during the holding time. The SRS value can be deduced from the creep curve by calculating the strain rate ($\dot{\varepsilon}$) and the hardness (H) using eq. 6.6 [121]:

$$m = \frac{\partial\, lnH}{\partial ln\dot{\varepsilon}} \tag{6.7}$$

$$n = 1/SRS \quad (6.8)$$

where n is the stress component of material.

For Berkovich tips, the strain rate and the hardness could be described in the following equations with the depth-sensing indentation technique [121]:

$$\dot{\varepsilon} = \frac{1}{h}\frac{dh}{dt} \quad (6.9)$$

$$H = P/24.5\ h^2 \quad (6.10)$$

Where h is the instantaneous indenter displacement and P and H are the indentation load and hardness, respectively. The displacement rate, h, can be calculated by fitting the displacement–time curve during the holding time, using the empirical law [121]:

$$h = h_0 + a(t-t_0)^p + kt \quad (6.11)$$

where h_0, a, t_0, p, and k are the fitting parameters.

Figure 6.6 shows the steps for the SRS value and Figure 6.7 shows the log-logarithmic relationship between the hardness and the strain rate during the holding time. The SRS can be obtained by linearly fitting the creep portion of the stationary state of Figure 6.7. It has been observed that the SRS has the same trend as the applied load. When the maximum load of x = 0 HEA increases from 50 to 200 mN, the average value of SRS decreases from 0.20 to 0.08 and decreases from approximately 0.15 to 0.035 when x = 1. For nanocrystalline metals, creep behavior can be mainly self-diffusion, grain boundary slippage, grain boundary diffusion, grain rotation and dislocation climb [121]. However, for the present alloy with such a large grain size, we could not consider the effect of the grain boundary on the creep properties.

The small and large indentation will have different creep mechanisms. For small depths of dimples (less than 40 nm), the zone of plastic deformation is very close to the free surface of the sample. Therefore, the diffusion length of the area under the penetrator to the near free surface becomes very short. During slow creep, self-diffusion along the indentor / sample interface and the free surface of the sample will play an important role [122].

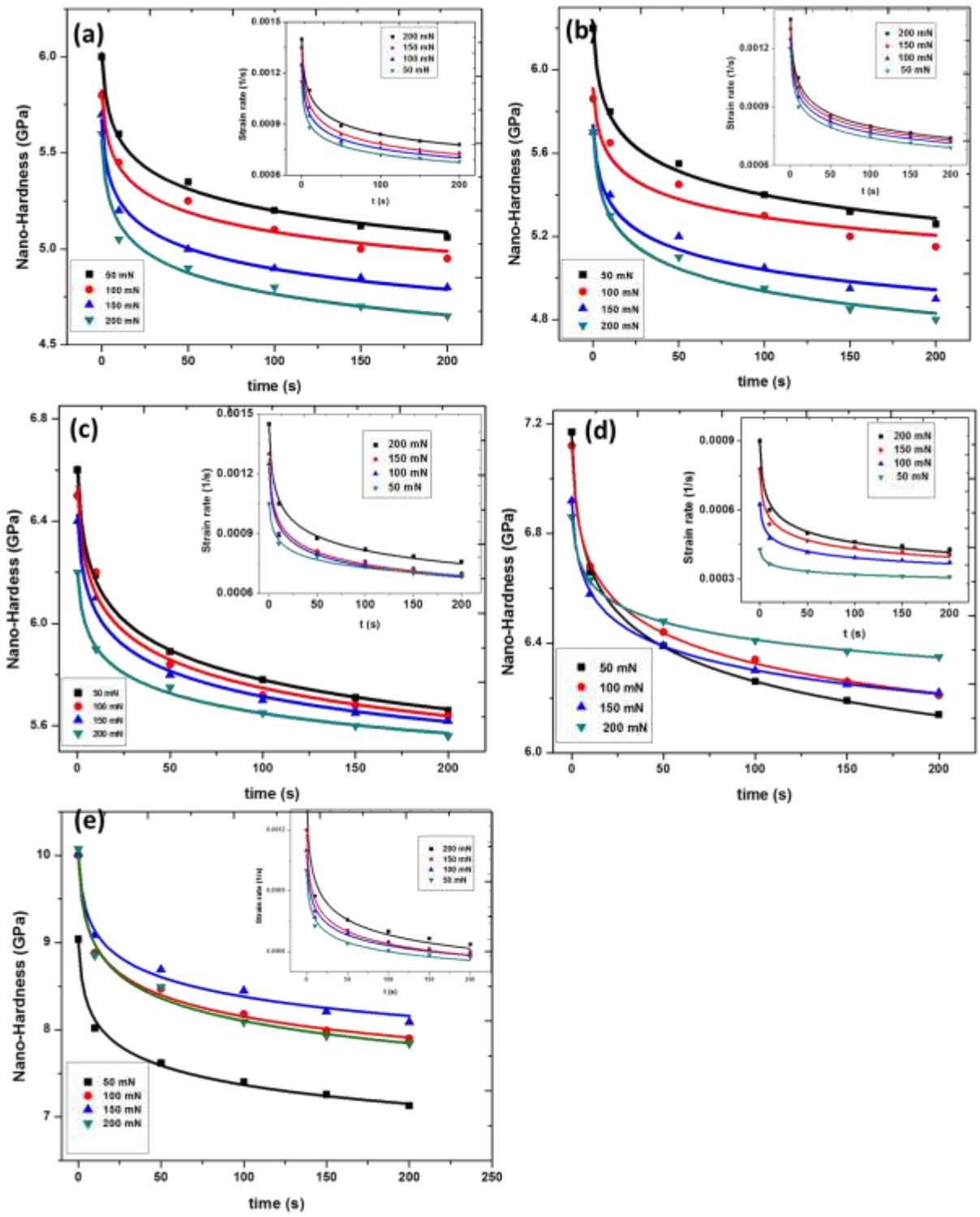

Fig. 6.6: On the basis of fitting lines in Fig. 6.5 we could calculate the hardness versus time (a,b,c,d,e) and strain rate versus time (inset) (a) AlCuCrFeMn (b) $AlCuCrFeMnW_{0.05}$ (c) $AlCuCrFeMnW_{0.1}$ (d) $AlCuCrFeMnW_{0.5}$ (e) AlCuCrFeMnW

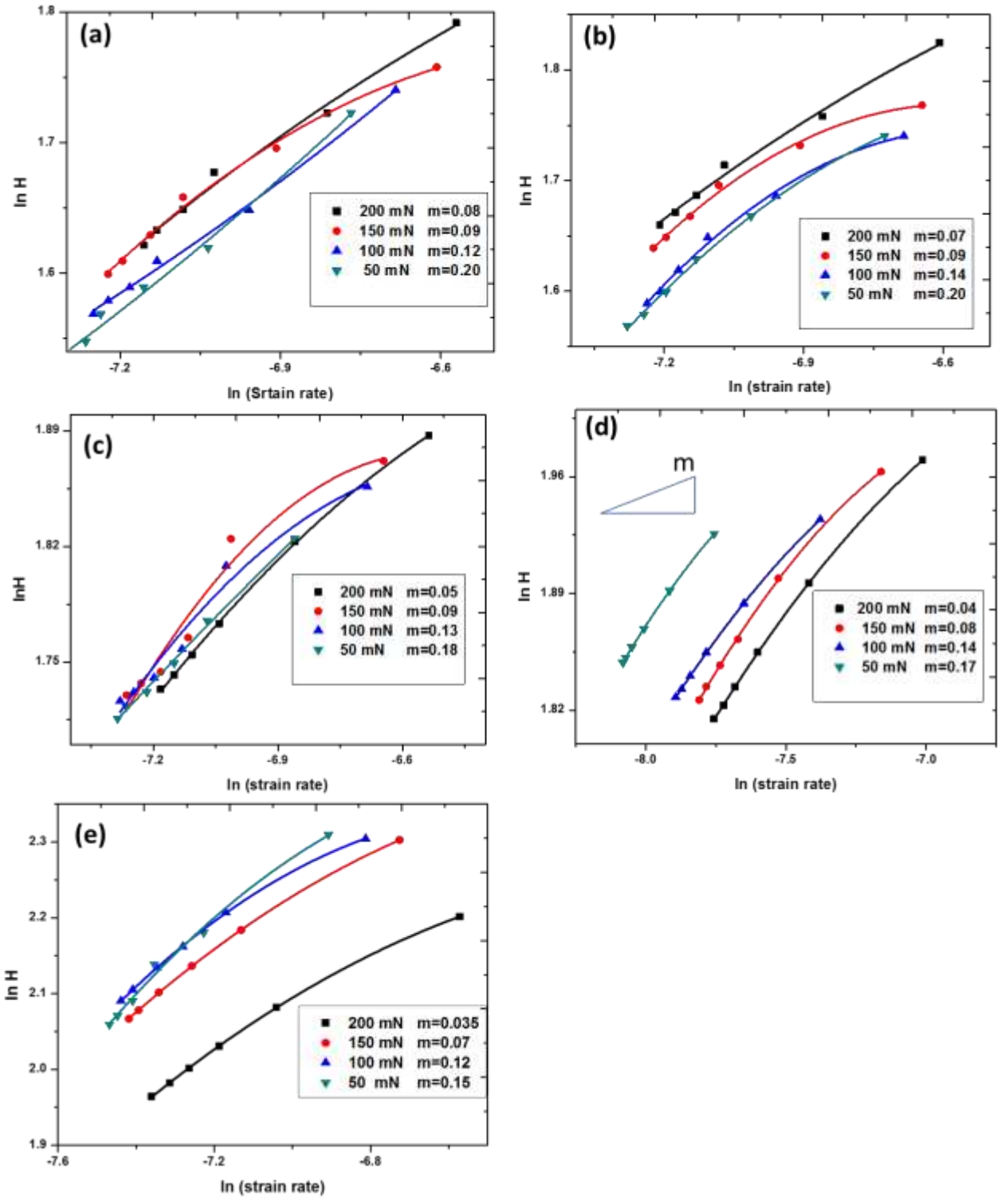

Fig. 6.7: The strain rate sensitivities (SRS) of the 50, 100, 150 and 200mN time-holding tests with constant loading rate creeps (a) AlCuCrFeMn (b) $AlCuCrFeMnW_{0.05}$ (c) $AlCuCrFeMnW_{0.1}$ (d) $AlCuCrFeMnW_{0.5}$ (e) AlCuCrFeMnW HEAs

When the indentation load increases to 200 mN and the depth of the indentation is approximately 130-150 nm, n increases to 25 for x = 1 HEA, which is approximately four times greater than for 50 mN. As shown in Table 6.3, the stress component increases with increasing holding load. This tendency shows the rapid change of the creep mechanism of the diffusive flow to the dislocation climb and slip with increasing indentation depth or depth of indentation.

For the current HEA, the stress component is higher than the typical value (~ 10) for higher holding loads. The results for some reasons, HEAs have highly distorted lattice structures and unstable dislocation lines with different atomic sizes and elementary chemical bonds. During creep deformation, multiple deformed networks and elements prevent movement of the dislocation. Nanoscale phases with a high concentration of solute atoms have the advantage of resisting creep deformation due to slow diffusion in the multiple element matrix [122]. This may be the reason why $AlCuCrFeMnW_x$ (x = 0, 0.05, 0.1, 0.5 & 1 mol) HEA have higher stress component values.

Table 6.3: Strain rate sensitivity (SRS) and stress component (n) of AlCuCrFeMnWx (x= 0, 0.05, 0.1, 0.5 & 1mol) at different loads.

	50 mN		**100 mN**		**150 mN**		**200 mN**	
	SRS	**n**	**SRS**	**N**	**SRS**	**N**	**SRS**	**N**
AlCuCrFeMn	0.20	5	0.12	8.3	0.09	11.1	0.08	12.5
$AlCuCrFeMnW_{0.05}$	0.20	5	0.14	7.1	0.095	11	0.07	14.2
$AlCuCrFeMnW_{0.1}$	0.18	5.5	0.13	7.7	0.09	11.1	0.05	20
$AlCuCrFeMnW_{0.5}$	0.17	5.9	0.14	7.1	0.08	12.5	0.04	25
AlCuCrFeMnW	0.15	6.66	0.12	8.3	0.07	14.2	0.035	28.5

Figure 6.7 presents the variations of SRS values with the strain rates for current alloy. The larger strain gradient induced by higher loads contributes to the occurrence and entanglement of more dislocations, which enhances the creep resistance and reduces the SRS values during creep process. Owing to the different atomic sizes and chemical bonds of the constituent elements,

HEAs possess a highly distorted lattice structure. The wiggled dislocation lines due to the lattice distortion, together with multiple components, arrest the dislocation movement during creep process, which is mainly responsible for the excellent creep resistance.

6.3.3 Creep mechanism and activation volume

In this study, from spherical indentation creep data the values of n can be directly obtained by using the equation [122]:

$$n = \delta \ln \dot{\varepsilon} / \delta \sigma \quad (6.12)$$

The $\dot{\varepsilon}$/was determined at the hold of 2000 sec while σ is estimated from H at the hold 200 sec by Tabor's empirical law, $\sigma \sim H/C$, where C is the constraint factor which is typically ~3 for metals. Note that the value of s is continuously varying during a constant-load indentation creep test. The Further insight into the mechanism of creep is obtained by estimating the value of the activation volume, V*, which is given by [122]:

$$V^* = \sqrt{3}\, kT\, (\delta \ln \dot{\varepsilon} / \ln \sigma) \quad (6.13)$$

where k is Boltzmann's constant.

The values of V* determined from the slopes of the linear fits of logarithmic $\dot{\varepsilon}$ vs. σ are displayed in Fig 6.8. Here, the Burgers vector b for the alloy was calculated as b = (a / 2) (111). where a is the lattice parameter (~3.07 Å). For AlCuCrFeMnW HEA, the calculated V* is ~1.2 b^3 at 50 mN which is smaller than V* for the forest dislocation cutting mechanism in conventional metals. It was suggested for shallow indentations that diffusion along the interface between the indenter tip and the sample surface may additionally play an important role, whereas for deep indentations the role of interfacial diffusion becomes negligible and conventional creep mechanisms related to microstructural activities are predominant. In this regard, the smaller-than-typical value of V* for HEA at higher load (V* = 0.8 b^3 at 200 mN) may indicate that interfacial diffusion continues to play a role and thus reduces V* while the main governing mechanism is dislocation.

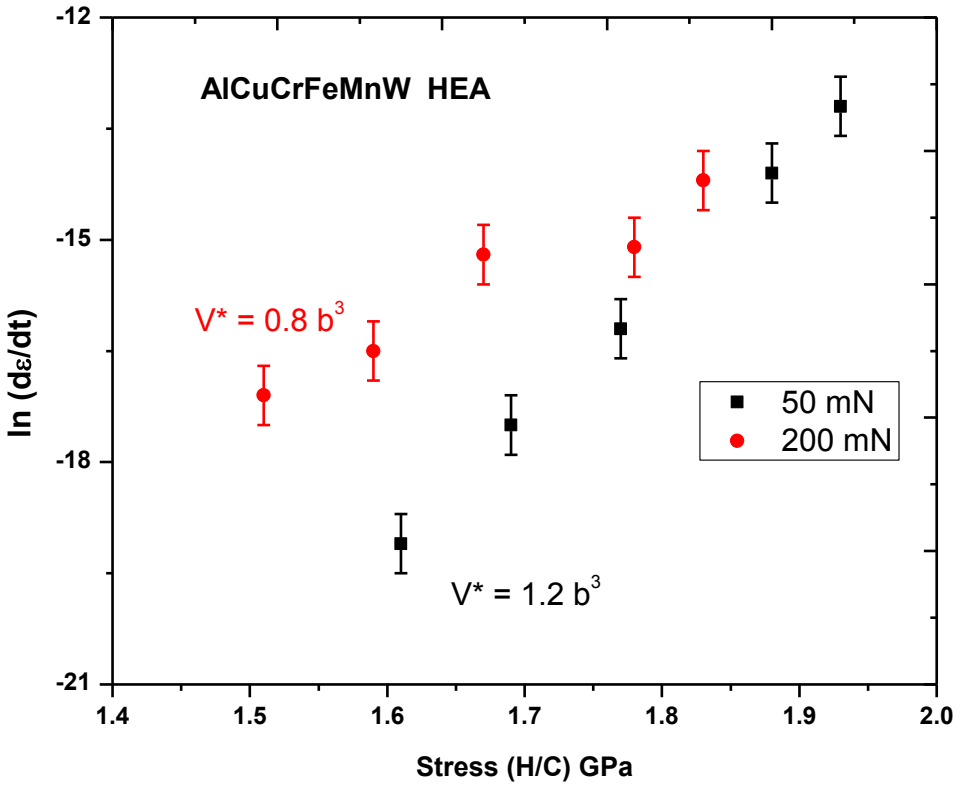

Fig. 6.8: Logarithmic strain rate vs. linear stress relation to estimate the activation volume V* for creep of AlCuCrFeMnW HEA at 50 and 200 mN Load.

Thus to summarize that present HEAs reaches 94-96% of the theoretical density, with an excellent Vickers hardness up to 780 HV. As the W content increases, the compressive fracture strength increases from 1010 to 1820 MPa. The volumetric fraction of the BCC structure phase (type W) increases with the increase of the W content, which is the main reason for increase in Vickers hardness, yield strength and fracture resistance. The main mechanisms of creep are the dislocation creep at high indentation load and self-diffusion at low indentation loads. Under different loads, the creep behavior of the alloy has obvious strain rate sensitivity (SRS). High holding loads lead to high stress components, and a lot of dislocations appear and become entangled together. Then, during the holding time, a large creep deformation of the high stress exponent will occur. In addition, the strain rate sensitivity is calculated from the creep at steady state and the mechanism of creep deformation is discussed.

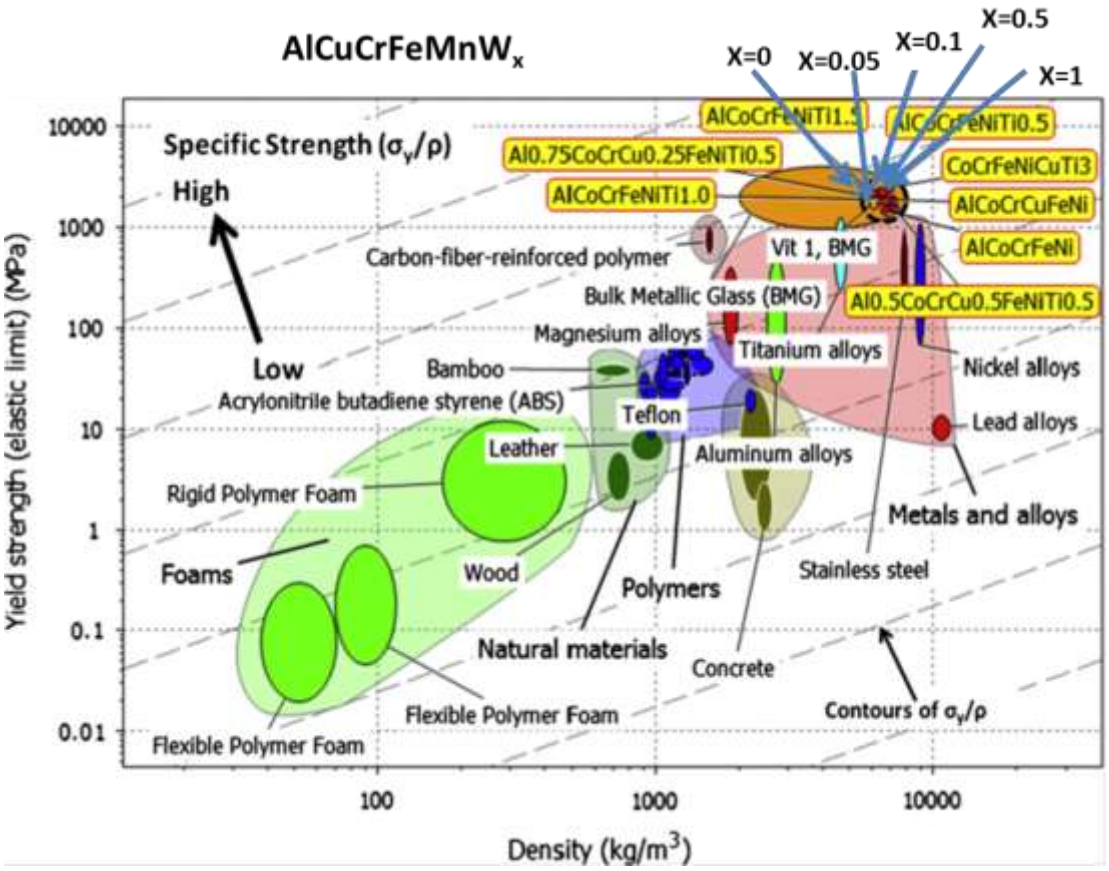

Fig. 6.9: Yield strength versus density diagram [49]

A peak hardness value has been achieved for the AlCuCrFeMnW$_x$ HEAs due to a combined effect of solid solution hardening, grain boundary hardening, and the precipitation hardening. Fig 6.9 shows that the AlCuCrFeMnW$_x$ alloys have the strengths comparable to other-density HEAs. Furthermore Corrosion behaviors of presents HEAs are discussed in next chapter 7.

Chapter 7

CORRODION STUDY OF SPSed AlCuCrFeMnW$_x$ (0, 0.05, 0.1, 0.5 & 1 mol) HEAs

Previous chapters indicate that the high entropy alloy AlCuCrFeMnW$_x$ has high hardness and can be worked and hardened with high strength at 900°C, which indicate that this alloy has potential applications in high temperature and structural. However, the corrosion behavior of AlCuCrFeMnW$_x$ alloys is not well understood. Therefore, the purpose of this study was to investigate the electrochemical behavior of AlCuCrFeMnW$_x$ alloys in a 3.5 wt% NaCl solution.

7.1 Open-Circuit Potential versus Time

The open circuit potential of AlCuCrFeMnW$_x$ (x = 0, 0.05, 0.1, 0.5 & 1 mol) as a function of time in a 3.5 wt% NaCl environment is shown in Fig 7.1.

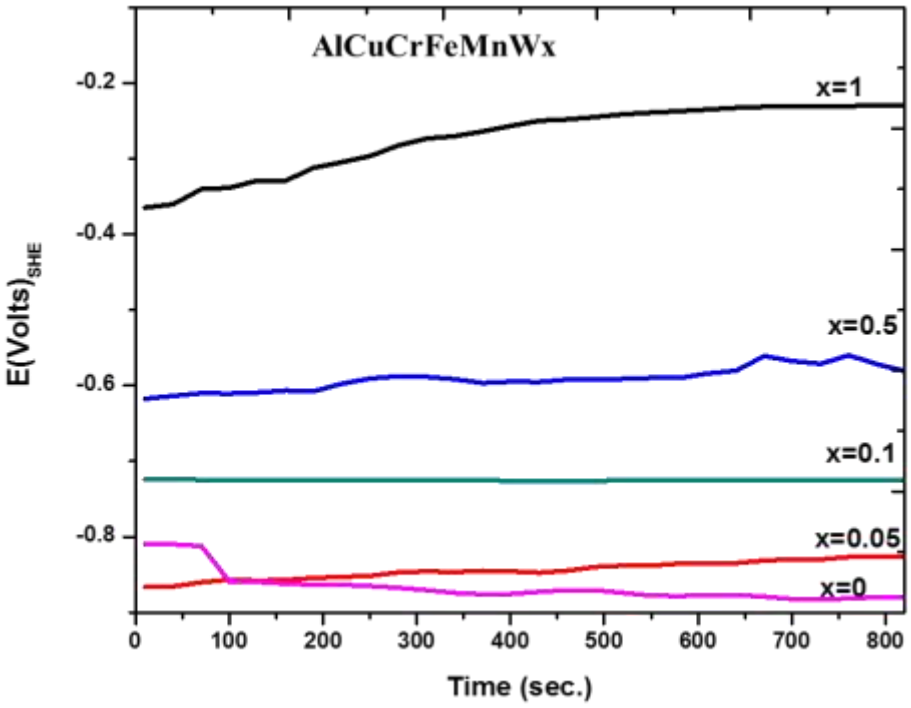

Fig. 7.1: Open-circuit potential of AlCuCrFeMnWx at different composition as a function of time in 3.5 wt% NaCl solution

It can be seen that the potential of HEA moves to the positive side initially, then slightly to the negative side when x = 0. This shows that a protective scale forms on the surface of the alloy x = 0 and then begins to dissolve. At x = 0.05 to x = 1, the alloy maintains a stable potential over time, which indicates that the film remains intact and protected. In general, an increase in positive potential means that a passivation film is formed, while a stable potential means that the film remains intact and protected. A decrease of the potential in the negative direction indicates interruption of the film, dissolution of the film or absence of film formation. Therefore, for any alloy to achieve a good resistance to corrosion, the potential should move to the more positive side or maintain a constant value over time under the chosen environmental conditions. The results show that the corrosion resistance of the alloy does not form a protective scale at x = 0 and forms a stable protective scale when x = 1 at 3.5 wt% NaCl solution.

7.2. Potentiodynamic Polarisation Curves

Figure 7.2 shows the potentiodynamic polarization curves of $AlCuCrFeMnW_x$ (x = 0, 0.05, 0.1, 0.5 & 1 mol) in 3.5 wt% NaCl solution. Table 7.1 lists the electrochemical parameters of $AlCuCrFeMnW_x$ (x = 0, 0.05, 0.1, 0.5 & 1 mol) in an environment of 3.5% by weight NaCl. The icorr for the $AlCuCrFeMnW_x$ alloy content (x = 0, 0.05, 0.1, 0.5 & 1 mol) increases with increasing tungsten content, indicating that the passivation barrier increases with increasing tungsten content. With the addition of tungsten, the corrosion potential of the alloys increased from -0.892 V to -0.313 V, and the corrosion current density decreased from 6.97×10^{-6} to 3.32×10^{-6} A/cm^2, which demonstrated that a high content of tungsten enhanced the corrosion resistance of the alloys in the 3.5 wt% NaCl solution.

It is more likely to appear passivation when the more positive of free corrosion potential, the smaller of free corrosion current density, the greater of linear polarization resistance, then the corrosion resistance is better; conversely, corrosion resistant is worse [123]. It has been determined that the addition of refractory elements to stainless steel can improve the resistance to pitting of chloride-containing media [124]. It is believed that W forms solid WO_3 layer in the outer region of the film in a neutral solution of NaCl according to the Pourbaix diagram [125]. The layer of WO_3 is selective cation oxide and can act as a very effective pitting inhibitor which blocks the binding of anions such as Cl^- and Br^- to allow the growth of the barrier layer within the Cr oxide. The bipolar layer resulting stabilizes the oxide phase [126].

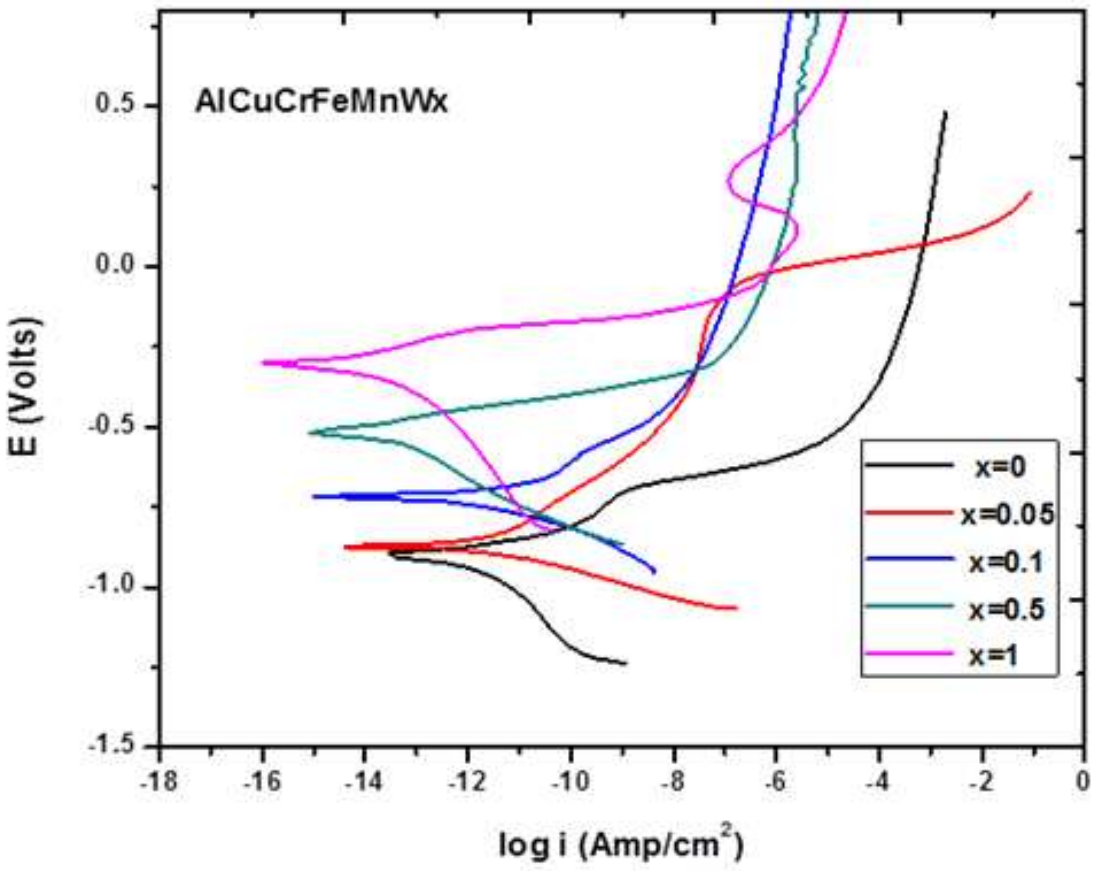

Fig. 7.2: Potentiodynamic curves for AlCuCrFeMnW$_x$ in 3.5% NaCl solution at 25 ◦C.

It can be seen in Figure 7.2, the corrosion rate of each alloy can be calculated using the following formula.

$$\text{Corrosion rate} = \frac{\text{icorr x k x EW}}{\rho} \quad (7.1)$$

Where:

i_{corr} is the corrosion current density (A cm^{-2}), p is the mass density (g cm^{-3}), EW is the equivalent of the electrode (g), k is constant (= 3272 mm / unit is millimeters per year (mmpy).

The equivalent weight is the weighted average of the ratio between the atomic weight of each element in the alloy and the number of exchange electrons (oxidation number) [62]:

$$EW = (\sum \frac{fini}{Ai})^{-1} \quad (7.2)$$

Where:

Where f_i is the mass fraction of the ith alloy component, n_i is the number of electrons exchanged for the ith alloy component and A_i is the atomic weight (g / mol) of the i th component alloy.

Table 7.1: Dynamic parameters derived from potentiodynamic polarization curves by tafel fit and corresponding corrosion rate.

$AlCuCrFeMnW_x$	**E_{corr} (V)**	**I_{corr} (A/cm^2)**	**Corrosion rate (mm/year)**
x=0	-0.892	6.97×10^{-6}	0.107
x=0.5	-0.876	6.12×10^{-6}	0.102
x=0.1	-0.716	5.39 v 10^{-6}	0.096
x=0.5	-0.503	4.32×10^{-6}	0.089
x=1	-0.313	3.32×10^{-6}	0.078
SS304	-0.223	0.76×10^{-6}	0.076 [ref 102]
Pure Mg	-1.623	5.50×10^{-6}	0.092 [ref 127]

7.3 SEM Micrographs of Corroded Surfaces

Figure 7.3 shows SEM micrographs of the potentiodynamic polarization of the $AlCuCrFeMnW_x$ alloy (x = 0, 0.05, 0.1, 0.5, 1 mol) in 3.5 wt% NaCl solution.

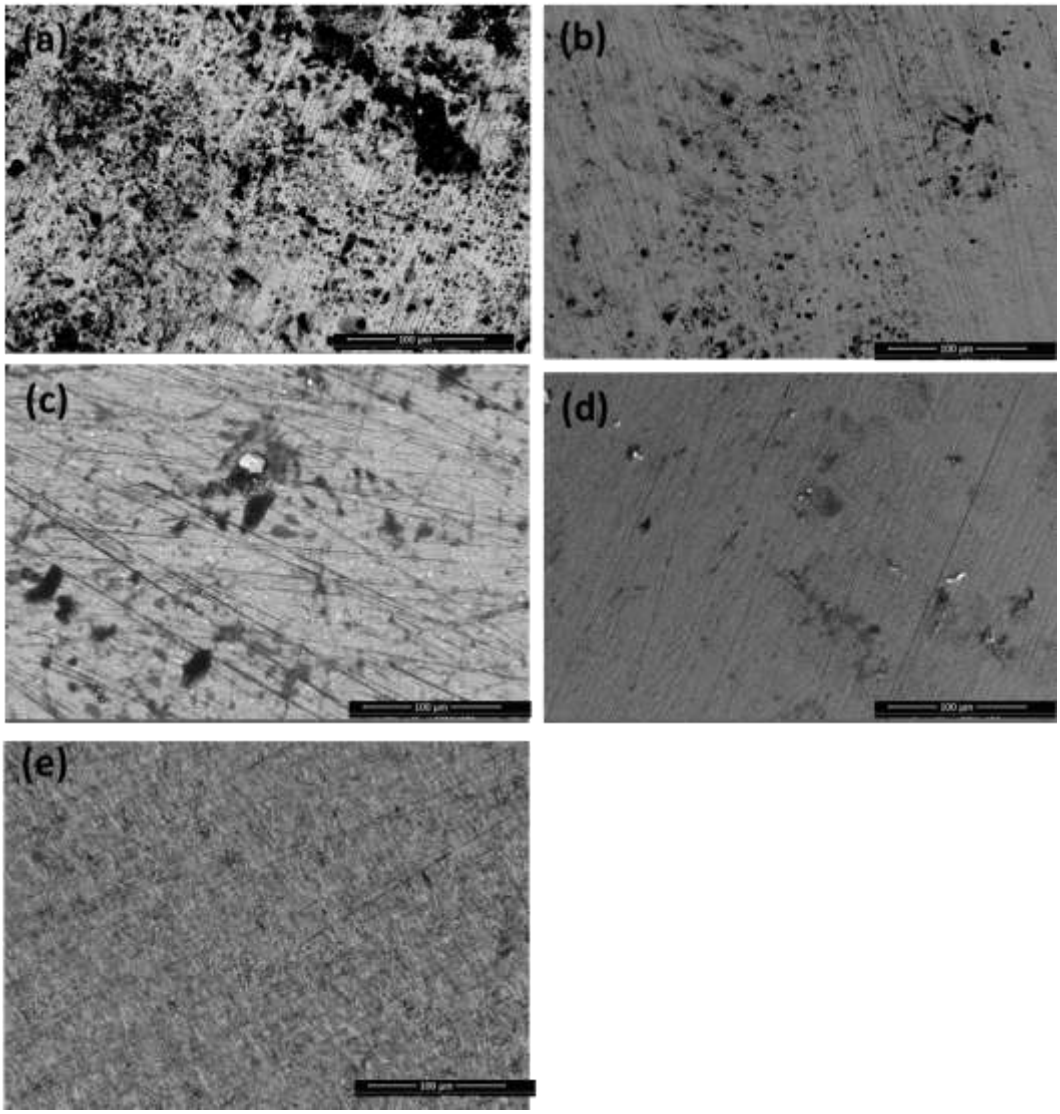

Fig. 7.3: SEM back scattered images of corrosion surface of (a) AlCuCrFeMn (b) $AlCuCrFeMnW_{0.05}$ (c) $AlCuCrFeMnW_{0.1}$ (d) $AlCuCrFeMnW_{0.5}$ (e) AlCuCrFeMnW HEAs

The corroded surfaces of the W-free alloy showed that the major type of corrosion was mainly pitting corrosion, not uniform corrosion. Several pits were observed in 3.5 wt% NaCl solution in a W-free alloy. In addition, the pits did not find in the surface of the alloy containing W, which supports the previous results from potentiodynamic polarization curve. Therefore, it appears that the alloy without W is more prone to pitting corrosion in the 3.5 wt% NaCl solution than the alloy containing W.

7.4 Functional group study by FTIR and XRD

FTIR was performed to determine the functional groups present on the surface after polarization experiment. The FTIR spectrum of the $AlCuCrFeMnW_x$ (x= 0, 0.05, 0.1, 0.5 & 1mol) alloys after polarization measurement is shown in Fig 7.4.

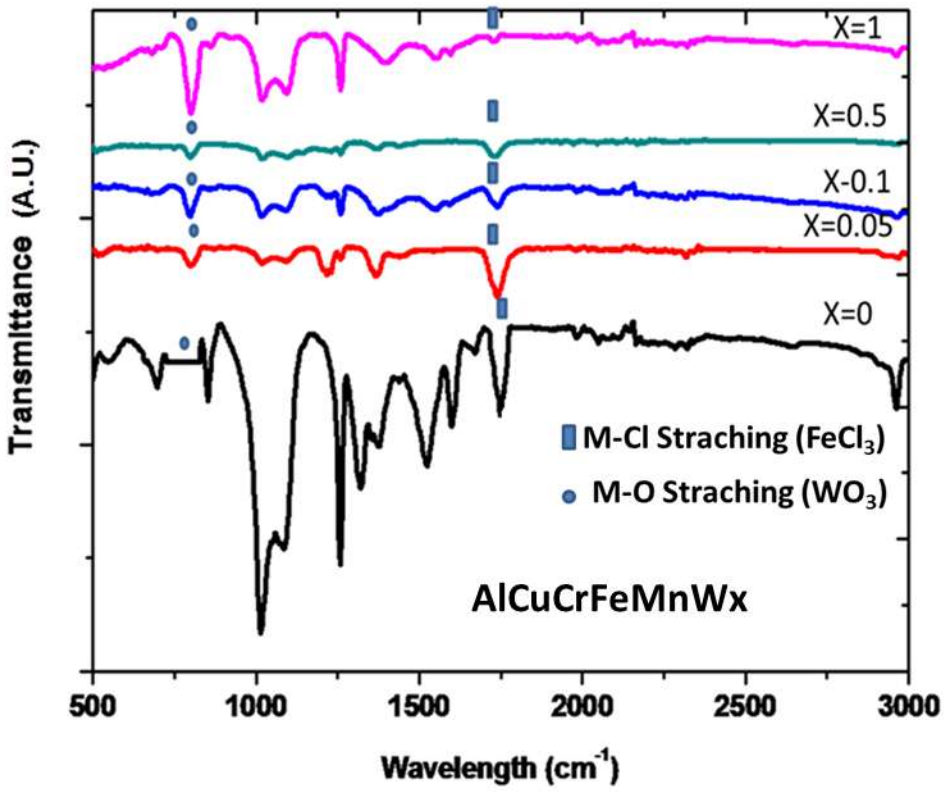

Fig. 7.4: FTIR spectrum after polarization measurement of $AlCuCrFeMnW_x$ (x=0, 0.05, 0.1, 0.5 & 1mol) HEAs

In case of AlCuCrFeMn (x=0) alloy, is to be noted that bands from the range 1701 cm^{-1} to 1797 cm^{-1}correspond to the M-X stretching in linear as well as bent triatomic molecules (like $FeCl_3$) and frequencies at 720 cm^{-1} to 787 cm^{-1} correspond to M=O (WO_3) stretching respectively. It is interesting to note that increasing of W content decreasing the M-X stretching means Cl^{-1} reaction with the metal decreases and formation of WO_3 layer increases with M=O stretching is increases. XRD spectra on the surface after polarization experiment shown in Fig. 7.5 it is also suggest that formation of passive WO_3 layer is increases with increasing the W content.

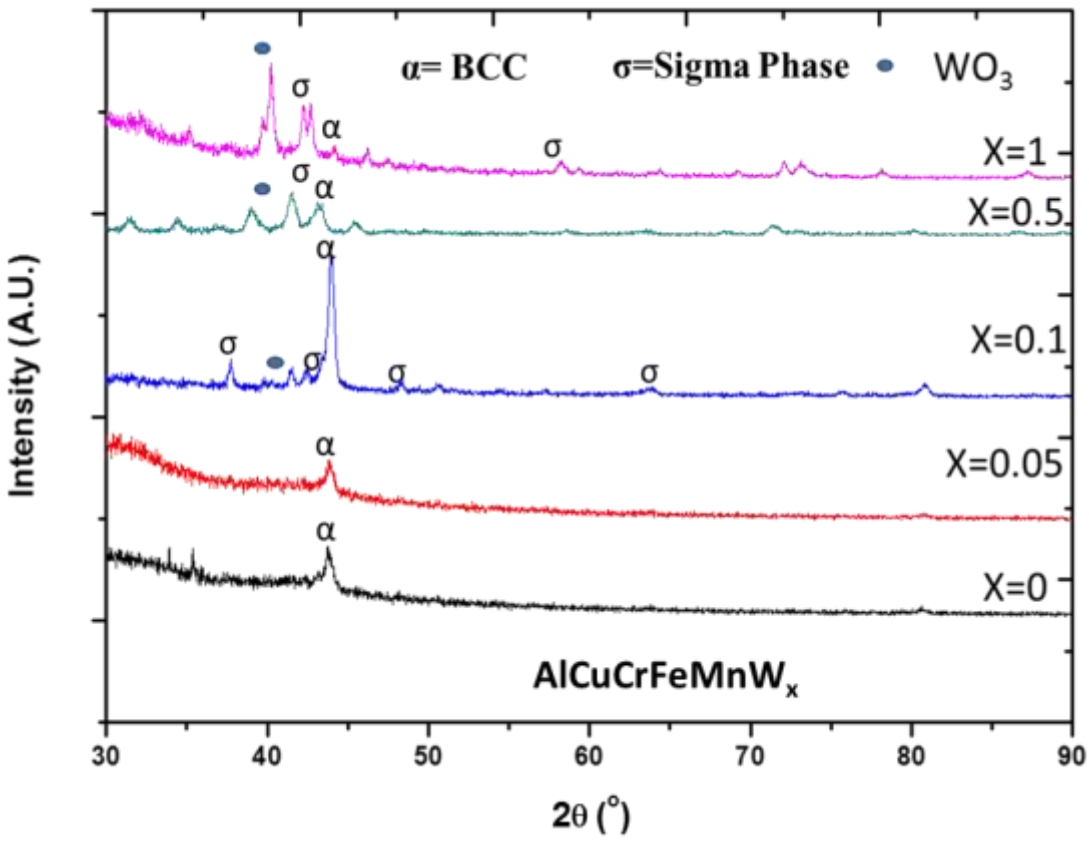

Fig. 7.5: XRD spectra after polarization measurement of SPSed AlCuCrFeMnW$_x$ (x=0, 0.05, 0.1, 0.5 & 1mol) HEAs

The corrosion experiments results indicates that the corrosion rate in AlCuCrFeMnW$_x$ alloys has a following order AlCuCrFeMn > AlCuCrFeMnW$_{0.05}$ > AlCuCrFeMnW$_{0.1}$> AlCuCrFeMnW$_{0.5}$ > AlCuCrFeMnW alloy. Thus, AlCuCrFeMnW alloy shows much easier passivation and it is more corrosion-resistant in 3.5% NaCl solution. It can be observed from Table 7.1 that AlCuCrFeMnWx alloys show exelent corrosion resistance and it's almost equal to SS304 stainless steel and greater than Pure Mg.

7.5 Electrochemical Impedance Spectroscopy

Electrochemical impedance is a powerful tool to study the processes of corrosion and passivation. EIS provides more information about electrochemical processes that occur on the surface than other electrochemical techniques. Figure 7.6 shows the effect of tungsten on Nyquist plot of the AlCuCrFeMnW$_x$ (x = 0, 0.05, 0.1, 0.5 & 1mol) alloy solution of 3.5 wt%

NaCl. Nyquist plot of $AlCuCrFeMnW_x$ (x = 0, 0.05, 0.1, 0.5 & 1mol) alloys includes one capacitive loop from high to low frequencies. The capacitive loop is related to the double layer which is typically related to the presence of charge transfer across the metal-electrolyte interface. Developing appropriate impedance models to adapt to the test data helps to evaluate the parameters and characterize the corrosion process. Figures 7.7 and 7.8 are given the $AlCuCrFeMnW_x$ (x = 0, 0.05, 0.1, 0.5 & 1mol) Bode diagram of the experimental and simulated alloy. An equivalent circuit is designed to better fit the experimental results of the electrodes, as shown in Figure 9. Such dispersion can be characterized using impedance Rs of the equivalent circuit (Rs(Cdl[Rp]), where Rs is the solution; Rp passivation resistance, Cdl is the double layer capacitance. The capacitor is a constant phase element (CPE) substituted in the compensation system for non-uniformity. The capacitors in the EIS experiments are often not ideal. Instead, its behavior is like that of a constant phase element, Z_{CPE}, which is given by [128]:

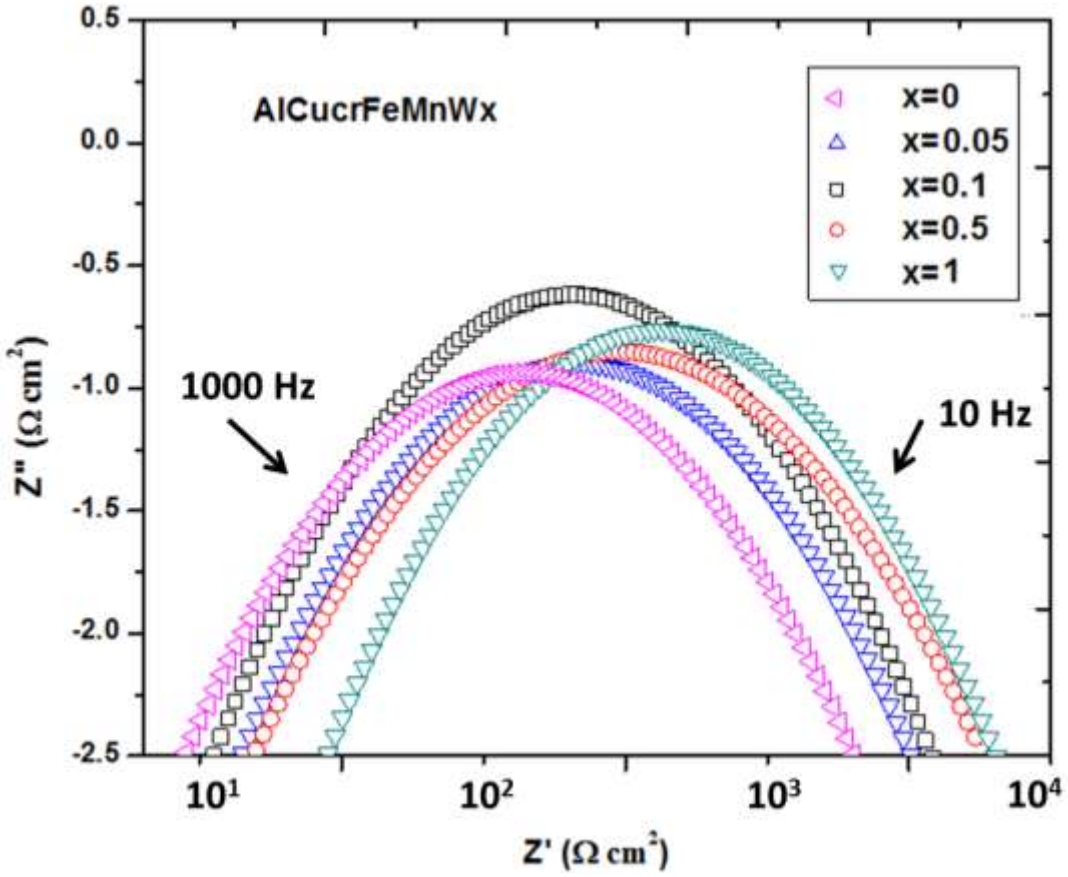

Fig. 7.6: The effect of tungsten on the Nyquist plot of the AlCuCrFeMnWx (x=0, 0.05, 0.1, 0.5 & 1mol) HEAs in 3.5 wt% NaCl solution.

$$Z_{CPE} = Q^{-1} (j\omega)^{-\alpha} \quad (7.3)$$

where, Q is the proportionality factor, j is the imaginary unit, ω is the angular frequency, and α is the phase shift. The CPE exponent α is a measure of the capacitance dispersion with values between 1 (ideal capacitance) and 0.7 (highly dispersed capacitance, such as at porous electrodes). For α = 0, Z_{CPE} represents a resistance with $R = Q^{-1}$; for α = 1, it represents a capacitance with C = Q; for α = 0.5, it represents a Warburg element, and for α = -1, it represents an inductance with $L = Q^{-1}$ [128].

The Nyquist plot consists of a semicircle of capacitance in the high frequency region and a long and little divergent tail. The average capacity of the capacitor is due to the presence of a passive film. Consequently, the large capacitance thus obtained caused by high interfacial area between the active surface of the covering layer of the large dielectric constant or a surface layer with the electrolyte. Both show that the porous corrosion products cover the alloy [129].

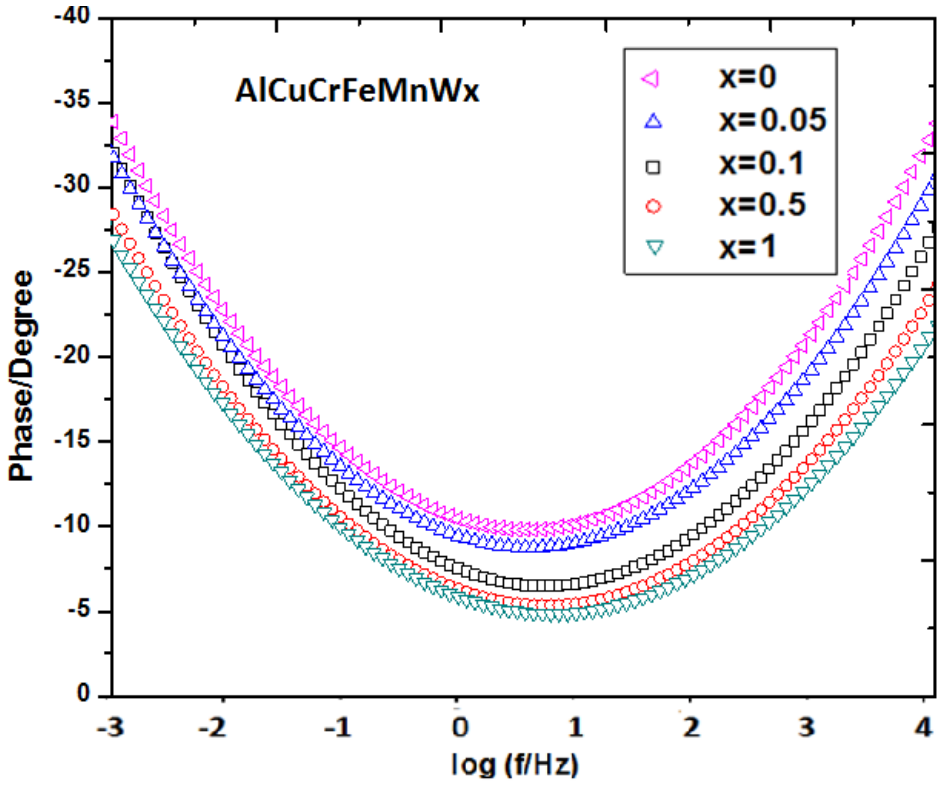

Fig. 7.7: Bode plot for the AlCuCrFeMnWx (x=0, 0.05, 0.1, 0.5 & 1mol) HEAs showing phase angle as a function of frequency.

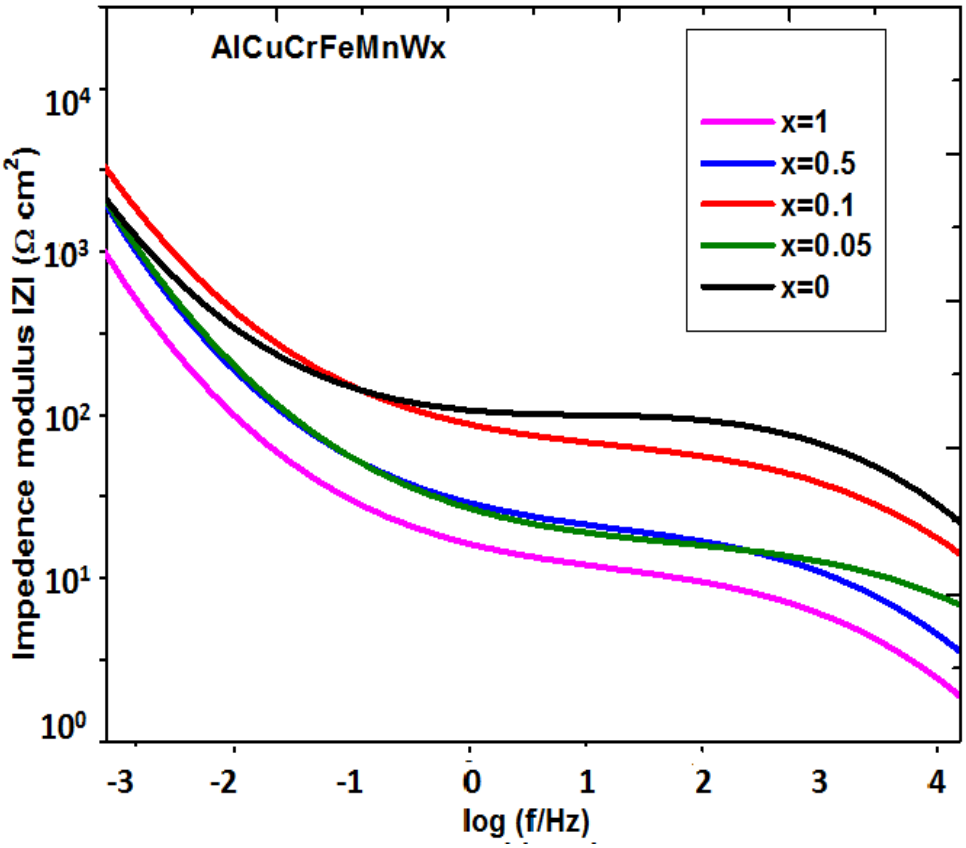

Fig. 7.8: Bode plot for the AlCuCrFeMnW$_x$ (x=0, 0.05, 0.1, 0.5 & 1mol) HEAs showing impedance modulus as a function of frequency.

The results of impedance tests are included in Fig. 7.7 and Fig. 7.8 in the form of Bode plot comparing the measured impedance of the AlCuCrFeMnW$_x$ (x= 0, 0.05, 0.1, 0.5 & 1mol) HEAs at their respective corrosion potentials. Note the curves of log(lZl (ω)) vs log(ω) and phase angle (φ) vs log (ω). The log(lZl (ω)) vs log(ω) plot provides information on polarization resistance (Rp) and solution resistance (Rs). The values of log(lZl (ω)) at very low frequencies (ω→ 0) represent Rp and at very high frequencies (ω→ ∞) represent Rs. Fig. 7.7 shows that the solution geometry (3.5 wt% NaCl) has very low resistance (Rs =5 Ω/cm2). From this, the Rp value varied from 1.12 kΩ/cm^2 to 3.92 kΩ/cm^2 with the increasing of W content, respectively, indicates that the HEA with higher W content has higher corrosion resistance than the W free HEA.

The phase angle plotted in Fig. 7.7 against log (ω) is defined as follows [129]:

$$\Phi = \tan^{-1}\left(\frac{\text{Im lzl}}{\text{Re lzl}}\right) \qquad (7.4)$$

The phase angle of all the alloys is similar to the shape of the frequency. A single local minimum shows that the capacitor is led by a single capacitor or two similar or typical capacitors. For all these alloys, these capacitors are passive films and / or double layer electric capacitors. The basis of the expansion of the phase angle and its magnitude represent the pseudocapacitive behavior, which can be quantified using constant phase elements. The magnitude of phase angle of the alloy without W is slightly smaller than that of the alloy containing W which is a result of a larger deviation from true capacitive behavior of the W free, though the difference is minimal.

This is also evidenced by the lower slope of the logarithmic-logarithmic linear region of the impedance module. As shown in Figure 7.9, the impedance curve is fitted to a simple equivalent circuit consisting of a series resistor connected in series with a resistor and a constant phase element (instead of a capacitor) in parallel. The Gamry Instruments software used by Echem Analyst and the adjusted parameters are given in Table 7.2.

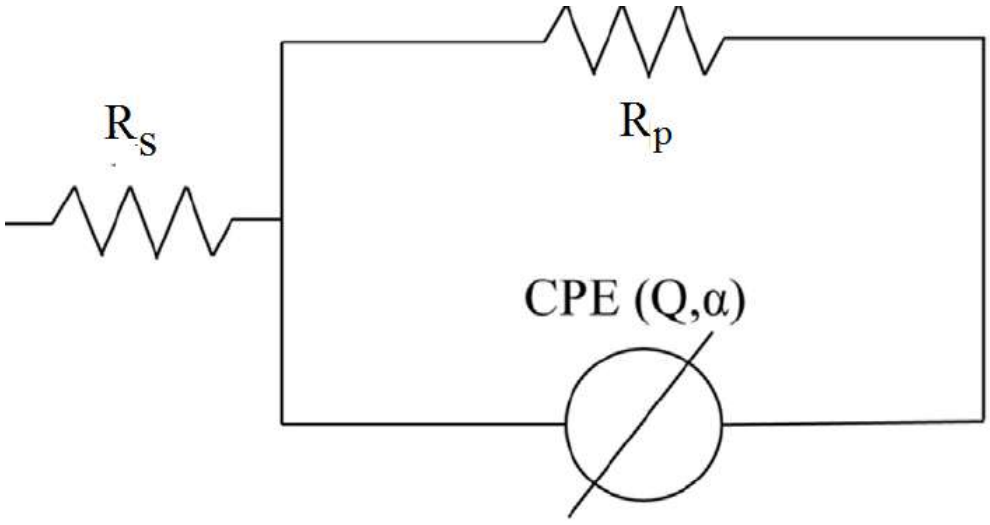

Figure 7.9: Equivalent electrical circuit used to fit impedance data. Rs and Rp are the electrolyte and polarization resistances, respectively. CPE is the constant phase element with its two fitting parameters, Q and α.

Table 7.2 : Parameters for impedance fit to the circuit in Fig. 7.9

$AlCuCrFeMnW_x$	R_s (Ω cm^2)	R_p ($k\Omega$ cm^2)	Q (Ω^{-1} s^{α})	α
x=0	4.12	1.12	9.2×10^{-5}	0.8723
x=0.05	6.23	2.11	7.5×10^{-5}	0.8897
x=0.1	7.54	2.34	5.2×10^{-5}	0.8978
x=0.5	12.78	2.78	3.0×10^{-5}	0.9188
x=1	15.34	3.98	2.1×10^{-5}	0.9284

In this work, the electrochemical performance of the high entropy alloy $AlCuCrFeMnW_x$ (x = 0, 0.05, 0.1, 0.5 & 1 mol) in a 3.5 wt% NaCl solution was studied. Polarization curves and SEM images show that in this study, the tungsten alloy containing in 3.5 wt% NaCl solution is not easily affected by pitting corrosion, and it is generally considered that the passivation film has the function of repair itself. With the addition of tungsten, the corrosion potential of the alloys increased from -0.892 V to -0.313 V, and the corrosion current density decreased from 6.97×10^{-6} to 3.32×10^{-6} A/cm^2, which confirmed that a high content of tungsten enhanced the corrosion resistance of the alloys. The FTIR and XRD spectra of the surface after the polarization experiment also show that the formation of the passive layer WO_3 increases with the increase in the content of W. The Nyquist plot is formed with one capacitive semicircle at high frequency region and a long diffusion tail at low frequency region. The capacitive semicircle is confirm tthe the presence of a passive film.

7.6 Structure-Property Correlation of Corroded Samples

It is more likely to appear passivation when the more positive of free corrosion potential, the smaller of free corrosion current density, the greater of linear polarization resistance, then the corrosion resistance is better; conversely, corrosion resistant is worse [123]. The addition of W is widely recognised for its beneficial effect on the corrosion resistance of the stainless steels and has been studied extensively in the literature [102]. However, it is proposed that the main effect of W was to decrease the rate of dissolution in active zones by formation and retention of W (VI)

oxyhydroxide (WO_3) at these sites. Furthermore, it is suggested that W is first dissolved from the substrate into the solution and then oxidised to WO_4^{-2}. However, given the 3.5 wt% NaCl solution conditions in this study and according to Pourbaix diagrams, an influence of W via WO_4^{-2} formation should be considered improbable, since, in these conditions, WO_4^{-2} is unstable thermodynamically and tends to precipitate as W (VI) oxide, e.g., WO_3. Hence, these diagrams establish WO_3 as the only compound formed in 3.5 wt% NaCl. Structure-property correlation demonstrated that a high content of tungsten enhanced the corrosion resistance of these alloys.

Thus to summarize that present HEAs reaches 94-96% of the theoretical density, with an excellent Vickers hardness up to 780 HV. As the tungsten content increases, the compressive fracture strength increases from 1010 MPa to 1820 MPa, while the fracture strain decreases from 14.81% to 5.12%. Materials-structure-property correlation study suggests that present HEAs may have potential usage in high temperature, structural and marine application.

Chapter 8

CONCLUSIONS

Following conclusions may be summarized based on present research work:

- Novel $AlCuCrFeMnW_x$ (x=0, 0.05, 0.1, 0.5 & 1 mol) HEAs prepared successfully by mechanical alloying. Calculated thermodynamic parameters suggest that present HEAs follow the criteria for the formation of a solid solution.

- XRD and SAED patterns confirmed the existence of BCC (BCC1 and BCC 2) as the pre-dominant phase and the FCC as the minor phase in $AlCuCrFeMnW_x$ (x=0, 0.05, 0.1, 0.5 & 1 mol) HEAs powders. DSC analysis depicts the thermal stability of $AlCuCrFeMnW_x$ (x=0, 0.05, 0.1, 0.5 & 1mol) HEAs powders up to 1273 K.

- As-milled $AlCuCrFeMnW_x$ (x=0, 0.05, 0.1, 0.5 & 1mol) powder samples have been compacted successfully by spark plasma sintering.

- The microstructure of bulk sintered $AlCuCrFeMnW_x$ (x=0, 0.05, 0.1, 0.5 & 1mol) HEAs consisted of predominantly AlFe type ordered structure, BCC phase and FeMn phase along with metastable Chromium rich σ-phase precipitates. Microstructure of AlCuCrFeMn is AlFe type ordered structure, FeMn phase with metastable Cr rich σ-phase precipitates. The formation and growth of Cr rich precipitates in FeMn phase in case of $AlCuCrFeMnW_x$ HEA is due to the high enthalpy difference between the binary elements.

- The activation energy E of $AlCuCrFeMnW_x$ HEAs was observed to vary in the range of 100-200 kJ mol^{-1}, which indicates that the synthesized sintered alloy have considerable crystallisation resistance.

- The hardness of the $AlCuCrFeMnW_x$ HEAs observed to vary between 633-891 HV and is attributed to the combined effect of solid solution hardening, grain boundary hardening and precipitation hardening. Maximum microhardness value achieved was 891 HV in case of x=1.

- The fracture strength under compression (σ_f) increased from 1010 to 1820 MPa with the increase of tungsten content of $AlCuCrFeMnW_x$ (x=0, 0.05, 0.1, 0.5 & 1mol) HEAs.

- Nanoindentation Creep studies suggest that the principal creep mechanism may be due to dislocation slip at high indentation loads. Self-diffusion along the indenter/specimen interface and along the free surface of the specimen might be playing an important role at a low indentation load of 50 mN.

- With the addition of tungsten, the corrosion potential of the alloys increased from -0.892 V to -0.313 V, and the corrosion current density decreased from 6.97×10^{-6} to 3.32×10^{-6} A/cm^2, which proved that a high content of tungsten improved the corrosion resistance of these alloys.

- The FTIR and XRD spectra of the surface after the polarization experiment also show that the formation of the passive layer WO_3 increased with the increasing content of tungsten. The Nyquist plot was constituted frequency region of one capacitive semicircle at high frequency region and a long diffusion tail at low frequency region. The capacitive semicircle is confirms the formation of a passive film.

Chapter 9

SUGGESTION FOR FUTURE WORK

- Theoretical study and modeling may be required to predict phases and microstructure using CALPHAD, Ab Initio…etc software.

- Detailed TEM studies of the $AlCuCrFeMnW_x$ alloys to understand the diffusion kinetics in $AlCuCrFeMnW_x$ HEAs. Interplanar spacing in SAED pattern also calculated using the IFFT through GATAN software.

- More studies on the contamination content and environmental degradation of the bulk alloys will provide the potential application areas of these HEAs.

- Studies on the mechanical properties such as tensile strength and wear behavior of $AlCuCrFeMnW_x$ HEAs.

- Suitable coating method may be selected to coat these alloys on various substrates.

- Oxidation study of the proposed HEAs may be performed to suggest their high temperature applicability.

- Extensive corrosion study may also be performed with varying electrolytes and concentration.

- For obtaining convicting results of phase fraction, Rietvelt analysis has to be conducted.

REFERENCES

[1] J. W. Yeh, S. K. Chen, S. J. Lin, J. Y. Gan, T. S. Chin, T. T. Shun, C. H. Tsau, S. Y. Chang, Nanostructured high-entropy alloys with multiple principal elements: novel alloy design concepts and outcomes, Adv. Eng. Mater.,Vol. 6, 2004, 299–303.

[2] P. Wang, H. Cai, X. Cheng, Effect of Ni/Cr ratio on phase, microstructure and mechanical properties of $Ni_xCoCuFeCr_{2x}$ (x = 1.0, 1.2, 1.5, 1.8 mol) high entropy alloys, J.Alloy. Comp.,Vol. 662, 2016, 20-31

[3] B. S. Murty, J. W. Yeh, S. Ranganathan, High-Entropy Alloy, Elsevier Inc., London, 2014.

[4] Y. Zhang, T. T. Zuo, Z. Tang, M. C. Gao, K. A. Dahmen, P. K. Liaw, Z. P. Lu, Microstructure and properties of high-entropy alloy, Prog. Mater. Sci., Vol. 61, 2014, 1-93.

[5] M. A. Hemphill, T. Yuan, G. Y. Wang, J. W. Yeh, C. W. Tsai, A Chuang and P. K. Liaw: 'Fatigue behavior of Al0.5CoCrCuFeNi high entropy alloys', Acta Mater., 2012, 60, 5723–5734.

[6] A. J. Zaddach, C. Niu, C. C. Koch and D. L. Irving: 'Mechanical properties and stacking fault energies of NiFeCrCoMn high entropy alloy', JOM, 2013, 65, 1780–1789.

[7] D. B. Miracle: 'Critical assessment 14: high entropy alloys and their development as structural materials', Mater. Sci. Technol., 2015, 31, 1142–1147.

[8] E. J. Pickering & N. G. Jones (2016): High-entropy alloys: a critical assessment of their founding principles and future prospects, International Materials Reviews, DOI: 10.1080/09506608.2016.1180020

[9] J. Joseph, T. Jarvis, X. Wu, N. Stanford, P. Hodgson, D. M. Fabijanic, Comparative study of the microstructures and mechanical properties of direct laser fabricated and arc-melted $Al_xCoCrFeNi$ high entropy alloys, Mater. Sci. Eng. A, Vol. 633, 2015, 184-193.

[10] E. Ma, Dissolving Equilibrium-Immiscible Elements via Severe Plastic Deformation, Mater. Trans., Vol. 47, 2006, 1269-1274.

[11] A.C. Reardon, Metallurgy for the Non-Metallurgist, 2nd Edition, ASM International, 2011

[12] M. H. Tsai, J. W. Yeh, High-Entropy Alloys: A Critical Review, Mater. Res. Lett., Vol. 2, 2014, 107-123.

[13] B. Cantor, I.T. Chang, microstructure development in equiatomic multicomponent alloys, mat sci and engg: A, vol 375-377,pp 213-218,7/15, 2004.

[14] M. H. Tsai, J. W. Yeh, High-Entropy Alloys: A Critical Review, Mater. Res. Lett., Vol. 2, 2014, 107-123.

[15] S. Guo, C. T. Liu, Phase stability in high entropy alloys: formation of solid solution phase and amorphous phase, Prog. Nat. Sci.*:* Mater. ***Int., Vol.***211 (21), 2015, 433–446.

[16] C. J. Tong, M. R. Chen, J. W. Yeh, S. J. Lin, S. K. Chen, T. T. Shun, S. Y. Chang, Mechanical performance of the $Al_xCoCrCuFeNi$ high-entropy alloy system with multiprincipal elements, Metall. Mater. Trans. A, Vol. 36 (5), 2005, 1263-1271.

[17] F. Otto, A. Dlouhy, Ch. Somsen, H. Bei, G. Eggeler, E. P. George, The influences of temperature and microstructure on the tensile properties of a CoCrFeMnNi high-entropy alloy, Acta Mater., Vol. 61 (15), 2013, 5743-5755.

[18] J. W. Yeh, Recent progress in high entropy alloy, Ann. Chim. Sci. Mat., Vol. 31 (6), 2006, 633-648.

[19] K.B. Zhang, Z.Y. Fu, J.Y. Zhang, J. Shi, W.M.Wang, H. Wang, Y.C.Wang, Q.J. Zhang, Nanocrystalline CoCrFeNiCuAl high-entropy solid solution synthesized by mechanical alloying, J. Alloys Comp., Vol. 485, 2009, L31–L34.

[20] H. P. Chou, Y. S. Chang, S. K. Chen, J. W. Yeh, Microstructure, thermophysical and electrical properties in Al$_x$CoCrFeNi ($0 \leq x \leq 2$) high-entropy alloys, Mater. Sci. and Eng. B, Vol. 163, 2009, 184–189.

[21] F. Otto, Y. Yang, H. Bei, E. P. George, Relative effects of enthalpy and entropy on the phase stability of equiatomic high-entropy alloys, Acta Mater. Vol. 61(7), 2013, 2628–2638.

[22] D. B. Miracle, O. N. Senkov, A critical review of high entropy alloys and related concepts, Acta Mater., 2016, 1-64, *In Press*

[23] JW Yeh. Recent progress in high-entropy alloys. Ann Chim Sci Mater 2006;31(6):633–48.

[24] MC Gao, N Unlu, M Mihalkovic, M Widom, Shiflet GJ. Glass formation, phase equilibria, and thermodynamic assessment of the Al–Ce–Co system assisted by first-principles energy calculations. Metall Mater Trans A 2007;38(10):2540–51.

[25] B Cantor, ITH Chang, P Knight, Vincent AJB. Microstructural development in equiatomic multicomponent alloys. Mater Sci Eng, A 2004;375–377:213–8.

[26] JW Yeh, SK Chen, Lin SJ, Gan JY, Chin TS, Shun TT, et al. Nanostructured high-entropy alloys with multiple principal elements: novel alloy design concepts and outcomes. Adv Eng Mater 2004;6(5):299–303.

[27] Y Zhang, X Yang, Liaw PK. Alloy design and properties optimization of high-entropy alloys. JOM 2012;64(7):830–8.

[28] Y Zhang, YJ Zhou, Lin JP, Chen GL, Liaw PK. Solid-solution phase formation rules for multi-component alloys. Adv Eng Mater 2008;10(6):534–8.

[29] JW Yeh. Recent progress in high-entropy alloys. Presentation at Changsha meeting; 2011.

[30] Y Zhang, YZ Zhou, XD Hui, ML Wang, GL Chen. Minor alloying behavior in bulk metallic glasses and high-entropy alloys. Sci China, Ser G 2008;51(4):427–37.

[31] S Singh, N Wanderka, BS Murty, U Glatzel, J Banhart. Decomposition in multi-component AlCoCrCuFeNi high-entropy alloy. Acta Mater 2011;59:182–90.

[32] B. Gludovatz, A. Hohenwarter, K. V. S. Thurston, H. Bei, Z. Wu, E. P. George, R. O. Ritchie, Exceptional damage-tolerence of a medium-entropy alloy CrCoNi at cryogenic temperatures, Nat. Comm., Vol. 7, 2015, 1-8.

[33] A. Gali, E. P. George, Tensile properties of high- and medium- entropy alloys, Intermetallics, Vol. 39, 2013, 74-78.

[34] J. W. Yeh, Y. L. Chen, S. J. Lin, S. K. Chen, High-entropy alloys – A new era of exploitation, Mater. Sci. Forum Vol. 560, 2007, 1-9.

[35] J. W. Yeh, S. J. Lin, T.S. Chin, J. Y. Gan, S. K. Chen, T. T. Shun et al., Formation of simple crystal structures in Cu–Co–Ni–Cr–Al–Fe–Ti–V alloys with multiprincipal metallic elements, Metall. Mater. Trans. A, Vol. 35 (8), 2004, 2533–2536.

[36] JW Yeh, SJ Lin, Chin TS, Gan JY, Chen SK, Shun TT, et al, Formation of simple crystal structures in Cu–Co–Ni–Cr–Al–Fe–Ti–V alloys with multiprincipal metallic elements. Metall Mater Trans A 2004;35(8):2533–6.

[37] JW Yeh, SY Chang, YD Hong, SK Chen, Lin SJ. Anomalous decrease in X-ray diffraction intensities of CuNiAlCoCrFeSi alloy systems with multi-principal elements. Mater Chem Phys 2007;103:41–6.

[38] Y Zhang, X Yang, PK Liaw. Alloy design and properties optimization of high-entropy alloys. JOM 2012;64(7):830–8.

[39] YJ Zhou, Y Zhang, YL Wang, Chen GL. Solid solution alloys of AlCoCrFeNiTix with excellent room-temperature mechanical properties. Appl Phys Lett 2007;90(18):181904.

[40] Y Zhang, YJ Zhou, XD Hui, ML Wang, Chen GL. Minor alloying behavior in bulk metallic glasses and high-entropy alloys. Sci China, Ser G 2008;51(4):427–37.

[41] JW Yeh, SK Chen, SJ Lin, JY Gan, Chin TS, Shun TT, et al. Nanostructured high-entropy alloys with multiple principal elements: novel alloy design concepts and outcomes. Adv Eng Mater 2004;6(5):299–303.

[42] JW Yeh. Recent progress in high-entropy alloys. Presentation at Changsha meeting; 2011

[43] Y Zhang, TT Zuo, Liaw PK, Cheng YQ. High-entropy alloys with high saturation magnetization and electrical resistivity. Sci Rep 2013;3:1455. http://dx.doi.org/10.1038/srep01455.

[44] Y Zhang, GL Chen, CL Gan. Phase change and mechanical behaviors of TixCoCrFeNiCu1_yAly high entropy alloys. J ASTM Int 2010;7(5):102527.

[45] K.Y. Tsai, M. H. Tsai, J. W. Yeh, Sluggish diffusion in Co-Cr-Fe-Mn-Ni high entropy alloys. Acta Mater., Vol. 61, 2013, 4887-4897.

[46] JW Yeh, SK Chen, SJ Lin, JY Gan, TS Chin, TT Shun, et al. Nanostructured high-entropy alloys with multiple principal elements: novel alloy design concepts and outcomes. Adv Eng Mater 2004;6(5):299–303.

[47] S. Ranganathan, Alloyed pleasures: multimetallic cocktails, Curr. Sci., Vol. 85, 2003, 1404-1406.

[48] S. Guo, Q. Hu, C. Ng, C. T. Liu, More than entropy in high-entropy alloys: forming solid solutions or amorphous phase, Intermetallics, Vol. 41, 2013, 96-103

[49] M. Avedesian, Hugh Baker, Magnesium and Magnesium Alloys, ASM International,Materials Park, OH, 1999.

[50] C. J. Tong, Y. L. Chen, S. K. Chen, J. W. Yeh, T. T. Shun, C. H. Tsau, et al., Microstructure characterization of Al_xFeCuCrCoNi high entropy alloy system with multiprincipal elements, Metall. Mater. Trans. A, Vol. 36, 2005, 881-893

[51] F. Otto, Y. Yang, H. Bei, E. P. George, Relative effects of enthalpy and entropy on the phase stability of equiatomic high-entropy alloys, Acta Mater. Vol. 61(7), 2013, 2628–2638.

[52] Y. Zhang, Y. J. Zhou, J. P. Lin, G. L. Chen, P. K. Liaw, Solid-solution phase formation rules for multi-component alloys, Adv. Eng. Mater., Vol. 10(6), 2008, 534–538.

[53] S. Guo, Q. Hu, C. Ng, C. T. Liu, More than entropy in high-entropy alloys: forming solid solutions or amorphous phase, Intermetallics, Vol. 41, 2013, 96-103.

[54] K. B. Zhang, Z. Fu, Effects of annealing treatment on phase composition and microstructure of CoCrFeNiTiAl_x high-entropy alloys, Intermetallics, Vol. 22, 2012, 24–32.

[55] X. Yang, Y. Zhang, Prediction of high-entropy stabilized solid-solution in multicomponent alloys, Mater. Chem. Phys., Vol. 132, 2012, 233-238.

[56] Y. Zhang, X. Yang, P. K. Liaw, Alloy design and properties optimization of high entropy alloys, JOM, Vol. 64, 2012, 830-838.

[57] Y. Dong, Y. Lu, L. Jiang, T. Wang, T. Li, Effects of electronegativity on the stability of topologically closed packed phase in high entropy alloy, Intermetallics, Vol. 52, 2014, 105-109.

[58] S. Guo, C. Ng, J. Lu, C. T. Liu, Effect of valence electron concentration on stability of fcc and bcc phase in high entropy alloy, J. Appl. Phys., 2011, Vol. 109, 103505-1-103505-2.

[59] M. H. Tsai, K.Y. Tsai, C. W. Tsai, C. Lee, C. C. Juan, J. W. Yeh, Criterion for sigma phase formation in Cr- and V- containing high-entropy alloys, Mater. Res. Lett., Vol. 1, 2013, 207-212.

[60] S Guo,C Ng, J Lu, CT Liu. Effect of valence electron concentration on stability of fcc or bcc phase in high entropy alloys. J.Appl Phys 2011;109:103505.

[61] M. Laurent-Brocq, L. Perriere, R, Pir`es, Y. Champion, From high entropy alloys to diluted multi-component alloys: Range of existence of a solid-solution, Mater. Design, 2016, doi: 10.1016/j.matdes.2016.04.046.

[62] YY Chen, T Duval, UD Hung, JW Yeh, HC Shih. Microstructure and electrochemical properties of high entropy alloys—a comparison with type-304 stainless steel. Corros Sci 2005;47(9):2257–79.

[63] H. Cui, H. Wang, J. Wang., H. Fu, 2011a. Microstructure and micro segregation in directionally solidified FeCoNiCrAl high entropy alloy. Adv. Mater. Res. Vol. 189-193, 2011, 3840-3843.

[64] S. G. Ma, S. F. Zhang, M. C. Gao, P. K. Liaw, Y. Zhang, A successful synthesis of the $CoCrFeNiAl_{0.3}$ single-crystal, high-entropy alloy by Bridgman solidification, JOM,Vol. 65, 2013, 1751-1758.

[65] B. A. Welk, R. E. A. Williams, G. B. Viswanathan, M. A. Gibson, P. K. Liaw, H. L. Fraser, Nature of the interfaces between the constituent phases in the high entropy alloy CoCrCuFeNiAl, Ultramicroscopy, Vol. 134, 2013, 193-199.

[66] V. Ocelik, N. Janssen, S. N. Smith, J. Th. M. De Hosson, Additive Manufacturing og high entropy alloys by laser processing, JOM, Vol. 68(7), 2016, 1810-1818.

[67] S. Chen, X. Chen, L. Wang, J. Liang, C. Liu, Laser cladding FeCrCoNiTiAl highentropy alloys coating reinforced with self-generated TiC particles, J. Laser Appl., Vol. 29(1), 2016, 012004-1-8.

[68] C. Suryanarayan,Mechanical alloying and milling, Prog. Mater. Sci., Vol. 46, 2001, 1-184.

[69] S. Varalakshmi, M. Kamaraj, B. S. Murty, Synthesis and characterization of nanocrystalline AlFeTiCrZnCu high entropy solid solution by mechanical alloying. J. Alloy Compd., Vol. 460, 2008, 253-257.

[70] M. Omori, Sintering, consolidation, reaction and crystal growth by the spark plasma system (SPS), Mater. Sci. Eng. A 287 (2000) 183-188.

[71] N. Saheb, Z. Iqbal, A. Khalil, A.S. Hakeem, N.A. Aqeeli, T. Laoui, A.A. Qutub, R. Kirchner, Spark plasma sintering of metals and metal matrix nanocomposites: A Review, J. Nano, 983470 (2012) 1-13.

[72] Z. A. Munir, U. Anselmi,Tamburini, The effect of electric field and pressure on the synthesis and consolidation of materials: A review of the spark plasma sintering method, J. Mater. Sci., Vol. 41, 2006, 763 –777.

[73] S. Chakraborty, P. K. Das, D. Ghosh, Spark Plasma Sintering and Structural Properties of ZrB_2 Based Ceramics: A Review, Rev.Adv. Mater. Sci., Vol. 44, 2016, 182-193.

[74] P.J. Kelly, R.D. Arnell, Magnetron sputtering: a review of recent developments and applications, Vacuum, Vol 56, 2000, 159-172.

[75] Z. An, H. Jia, Y. Wu, P. D. Rack, A. D. Patchen, Y. Liu, Y. Ren, N. Li, P. K. Liaw, Solid-Solution CrCoCuFeNi High-Entropy Alloy Thin Films Synthesized by Sputter Deposition, Mater. Res. Lett., Vol. 3(4), 203–209.

[76] T. Yang, S. Xia, S. Liu, C. Wang, S. Liu, Y. Zhang, J. Xue, S. Yan, Y. Wang, Effects of AL addition on microstructure and mechanical properties of Al*x*CoCrFeNi High entropy alloy, Mater. Sci. Eng. A, 2015,http://dx.doi.org/10.1016/j.msea.2015.09.034.

[77] A. Munitz, S. Salhov, S. Hayun, N. Frage, Heat treatment impacts the micro-structure and mechanical properties of AlCoCrFeNi high entropy alloy, J. Alloy Compd., 2016, 10.1016/j.jallcom.2016.05.034.

[78] A. Zhang, J. Han, J. Meng, B. Su, P. Li, Rapid preparation of AlCoCrFeNi high entropy alloy by spark plasma sintering from elemental powder mixture, Mater. Lett., Vol. 181, 2016, 82-85.

[79] O Maulik, V Kumar, Synthesis of AlFeCuCrMgx (x = 0, 0.5, 1, 1.7) alloy powders by mechanical alloying, Materials Characterization, (2015),110, p116-125.

[80] O Maulik, D Kumar, S Kumar, DM Fabijanic, V Kumar, Structural evolution of spark plasma sintered AlFeCuCrMgx (x=0, 0.5, 1, 1.7) high entropy alloys, Intermetallics 77 (2016) 46-56.

[81] B. Liu, J. Wang, Y. Liu, Q. Fang, Y. Wu, S. Chen, C. T. Liu, Microstructure and mechanical properties of equimolar FeCoCrNi high entropy alloy prepared via powder extrusion, Intermetallics, Vol. 75, 2016, 25-30.

[82] C. F. Lee, T. T. Shun, Effect of Fe content on microstructure and mechanical properties of $Al_{0.5}CoCrFe_xNiTi_{0.5}$ high-entropy alloys, Mater Charac., 2016, doi: 10.1016/j.matchar.2016.02.018.

[83] C. Y. Hsu, C. C. Juan, W. R. Wang, T. S. Sheu, J. W. Yeh,, S. K. Chen, On the superior hot hardness and softening resistance of $AlCoCr_xFeMo_{0.5}Ni$ high-entropy alloys, Mater. Sci. Engg. A, Vol. 528, 2011, 3581-3588.

[84] Y. J. Hsu, W. C. Chiang, J. K. Wu, Corrosion behavior of $FeCoNiCrCu_x$ high-entropy alloys in 3.5% sodium chloride solution, Mater. Chem. Phy., 2005, Vol. 92, 112-117.

[85] H. F. Sun, C. M. Wang, X. Zhang, R. Z. Li, L. Y. Ruan, Study of microstructure and performance of high entropy alloys $Al_xFeCuCoNiCrTi$, Mater. Res, Innov., Vol. 19, 2015, 89-93.

[86] L. Tian, Z.M. Jiao, G.Z. Yuan, S.G. Ma, Z.H. Wang, H.J. Yang, Y. Zhang, and J.W. Qiao, Effect of Strain Rate on Deformation Behavior of AlCoCrFeNi High-Entropy Alloy by Nanoindentation, Journal of Materials Engineering and Performance, DOI: 10.1007/s11665-016-2082-8

[87] N.D. Stepanov, N.Y. Yurchenko, D.G. Shaysutanov, G.A. Salishchev, M.A. Tikhonovsky, Effect of Al on structure and mechanical properties of $Al_xNbTiVZr$ (x=0, 0.5, 1, 1.5) high entropy alloys, Mater. Sci. Technol. 2015, Vol. 31, 1184–1193.

[88] Yan Zhang, Yuan Liu, Yan xiang Li, Xiang Chen, Huawei Zhang, Microstructure and mechanical properties of refractory HfNbTiVSi0.5 high-entropy alloy composite, Materials Letters174(2016)82–85

[89] N.D. Stepanov, N.Yu. Yurchenko, E.S. Panina, M.A. Tikhonovsky, S.V. Zherebtsov, Precipitation-strengthened refractory Al0.5CrNbTi2V0.5 high entropy alloy, Materials Letters 188 (2017) 162–164

[90] O.N. Senkov, J.K. Jensen, A.L. Pilchak, D.B.Miracle, H.L. Fraser, Compositional variation effects on the microstructure and properties of a refractory high-entropy superalloy AlMo0.5NbTa0.5TiZr, Materials and Design 139 (2018) 498–511

[91] G.A. Salishchev, M.A. Tikhonovsky, D.G. Shaysultanov, N.D. Stepanov , A.V. Kuznetsov, I.V. Kolodiy, A.S. Tortika, O.N. Senkov, Effect of Mn and V on structure and mechanical properties of high-entropy alloys based on CoCrFeNi system, Journal of Alloys and Compounds 591 (2014) 11–21

[92] Owais Ahmed Waseem, Junho Lee, Hyuck Mo Lee, Ho Jin Ryu, The effect of Ti on the sintering and mechanical properties of refractory high-entropy alloy TixWTaVCr fabricated via spark plasma sintering for fusion plasma-facing materials, Materials Chemistry and Physics 210 (2018) 87-94

[93] É. Fazakas, V. Zadorozhnyy, L.K. Varga, A. Inoue, D.V. Louzguine-Luzgin, Fuyang Tian, L. Vitos, Experimental and theoretical study of Ti20Zr20Hf20Nb20X20 (X = V or Cr) refractory high-entropy alloys, Int. Journal of Refractory Metals and Hard Materials 47 (2014) 131–138

[94] Hui Jiang, Huanzhi Zhang, Tiandang Huang, Yiping Lu, Tongmin Wang, Tingju Li, Microstructures and mechanical properties of Co2MoxNi2VWx eutectic high entropy alloys, Materials and Design 109 (2016) 539–546

[95] O.N. Senkov, C.F. Woodward, Microstructure and properties of a refractory NbCrMo0.5Ta0.5TiZr alloy, Materials Science and Engineering A 529 (2011) 311– 320

[96] O.N. Senkov, J.M. Scott S.V. Senkov, D.B. Miracle, C.F. Woodward, Microstructure and room temperature properties of a high-entropy TaNbHfZrTi alloy, Journal of Alloys and Compounds 509 (2011) 6043–6048

[97] Chun-Ming Lin, Chien-Chang Juan, Chia-Hsiu Chang, Che-Wei Tsai, Jien-Wei Yeh ,Effect of Al addition on mechanical properties and microstructure of refractory AlxHfNbTaTiZr alloys, Journal of Alloys and Compounds 624 (2015) 100–107

[98] N.D. Stepanov, N. Yu Yurchenko, D.V. Skibin, M.A. Tikhonovsky, G.A. Salishchev, Structure and mechanical properties of the AlCrxNbTiV (x =0, 0.5, 1, 1.5) high entropy alloys, Journal of Alloys and Compounds 652 (2015) 266-280

[99] Yuan Liu, Yan Zhang, Heng Zhang, Naijuan Wang, Xiang Chen, Huawei Zhang, Yan xiang Li, Microstructure and mechanical properties of refractory HfMo0.5NbTiV0.5Six high-entropy composites, Journal of Alloys and Compounds 694 (2017) 869-876

[100] N.D. Stepanov, D.G. Shaysultanov, G. A. Salishchev, M.A. Tikhonovsky, Structure and mechanical properties of a light-weight AlNbTiV high entropy alloy, Mater. Lett., 2015, 142, p 153-155.

[101] Hui Jiang, Li Jiang, Kaiming Han, Yiping Lu, Tongmin Wang, Zhiqiang Cao, and Tingju Li, Effects of Tungsten on Microstructure and Mechanical Properties of CrFeNiV0.5Wx and CrFeNi2V0.5Wx High-Entropy Alloys, Journal of Materials Engineering and Performance, 4594—Volume 24(12) December 2015

[102] Y. Hsu, W. Chiang, J. Wu, Corrosion behavior of FeCoNiCrCux high-entropy alloys in 3.5% sodium chloride solution, Mater. Chem. Phys. 92 (2005) 112-117.

[103] W.C. Oliver and G.M. Pharr: J. Mater. Res., 1992, vol. 7, pp. 1564–83.

[104] YL Chen, YH Hu, CA Hsieh, JW Yeh, SK Chen, Competition between elements during mechanical alloying in an octonary multi-principal-element alloy system, J. Alloys Compd. 481 (2009) 768–775.

[105] R. Sriharitha, B.S. Murty, R.S. Kottada, Phase formation in mechanically alloyed AlxCoCrCuFeNi (x = 0.45, 1, 2.5, 5 mol) high entropy alloys, Intermetallics, 32 (2013) 119-126

[106] C.S. babu, K. Sivaprasad, Characterization of nanocrystalline AlCoCrCuNiFeZn high entropy alloys produced by mechanical alloying, Procedia material science (2014) 1020-1026

[107] R. M..Pohan', B. Gwalani, J. Lee, T. Alam, J.Y.Hwang, H. J. Ryu, R. Banerjee', S. H. Hong, Microstructures and mechanical properties of mechanically alloyed and spark plasma

sintered $Al_{0.3}$CoCrFeMnNi high entropy alloy, Materials Chemistry and Physics https://doi.org/10.1016/j.matchemphys.2017.09.013 (In press)

[108] HA Baghbaderani, S Sharafi, MD Chermahini, Investigation of nanostructure formation mechanism and magnetic properties in Fe45Co45Ni10 system synthesized by mechanical alloying, Powder Technol. 230 (2012) 241–246.

[109] A Takeuchi, A Inoue, Calculations of mixing enthalpy and mismatch entropy for ternary amorphous alloys, Mater. Trans. JIM 41 (2000) 1372–1378.

[110] ASM Handbook, Voluvol. 3, ASM International

[111] D. Tabor, The hardness and strength of metals, J. Inst. Met. 79 (1951) 1-18.

[112] R. S. Ganji , P. S. Karthik , K. B. S. Rao , K. V. Rajulapati, Strengthening mechanisms in equiatomic ultrafine grained AlCoCrCuFeNi high-entropy alloy studied by micro- and nanoindentation methods, Acta Materialia 125 (2017) 58-68

[113] G.K. Williamson, R.E. Smallman, Dislocation densities in some annealed and cold-worked metals from measurements on the X-ray debye-scherrer spectrum, Philos. Mag.1 (1956) 34-46

[114] R. Labusch, Statistical theories of solid solution hardening, Acta Metall. 20 (1972) 917-927

[115] B.G. Yoo, K.S. Kim, J.H. Oh, U. Ramamurty, and J.I. Jang, Room Temperature Creep in Amorphous Alloys: Influence of Initial Strain and Free Volume, Scr. Mater., 2010, 63, p 1205

[116] W.B. Li, J.L. Henshall, R.M. Hooper, and K.E. Easterling, The Mechanisms of Indentation Creep, Acta Metall. Mater., 1991, 39, p 3099

[117] S.A. Syed Asif and J.B. Pethica, Nanoindentation Creep of Single- Crystal Tungsten and Gallium Arsenide, Philos. Mag. A, 1997, 76, p 1105

[118] Z.J. Wang, S. Guo, Q. Wang, Z.Y. Liu, J.C. Wang, Y. Yang, and C.T. Liu, Nanoindentation Characterized Initial Creep Behavior of a High- Entropy-Based Alloy CoFeNi, Intermetallics, 2014, 53, p 183

[119] Z.M. Jiao, M.Y. Chu, H.J. Yang, Z.H. Wang, and J.W. Qiao, Nanoindentation Characterized Plastic Deformation of a Al0.5CoCrFe-Ni High Entropy Alloy, Mater. Sci. Technol., 2015, 31, p 1244

[120] Y. Ma, G.J. Peng, D.H. Wen, and T.H. Zhang, Nanoindentation Creep Behavior in a CoCrFeCuNi High-Entropy Alloy Film with Two Different Structure States, Mater. Sci. Eng. A, 2015, 621, p 111

[121] C.L. Wang, M. Zhang, and T.G. Nieh: 2009, vol. 42, p. 115405.

[122] H. Li and A.H.W. Ngan, J. Mater. Res., 2004, vol. 19 (2),pp. 513–522.

[123] D. Zander, B. Heisterkamp, I. Gallino, Corrosion resistance of Cu–Zr–Al–Y and Zr–Cu–Ni–Al–Nb bulk metallic glasses, J. Alloys Compd. 434–435 (2007) 234– 236.

[124] R.J. Brigham, Pitting of molybdenum bearing austenitic stainless steel, Corrosion 28 (1972) 177–179

[125] M. Pourbaix, Atlas of electrochemical equilibria in aqueous solutions, NACE, Houston, TX, 1974

[126] C.R. Clayton, Y.C. Lu, A bipolar model of the passivity of stainless steel: the role of Mo addition, J. Electrochem. Soc. 133 (1986) 2465–2473.

[127] I.B. Singh, M. Singh, S. Das, A comparative corrosion behavior of Mg, AZ31 and AZ91 alloys in 3.5% NaCl solution, Journal of Magnesium and Alloys 3 (2015) 142-148

[128] M. Kissi, M. Bouklah, B. Hammouti, M. Benkaddour, Establishment of equivalent circuits from electrochemical impedance spectroscopy study of corrosion inhibition of steel by pyrazine in sulphuric acidic solution, Appl. Surf. Sci. 252 (2006) 4190–4197.

[129] C.N. Cao, J.Q. Zhang, An Introduction to Electrochemical Impedance Spectroscopy, Science Press, Beijing, 2002.

List of published papers from this research work

1. **Devesh Kumar**, O. Maulik, S. Kumar, Y.V.S.S. Prasad, V. K. Sharma, V. Kumar, Impact of tungsten on phase evolution in nanocrystalline AlCuCrFeMnW$_x$ (x=0, 0.05, 0.1 and 0.5 mol) high entropy alloys, Material Research Express, Vol.4 No.11 (2017) DOI https://doi.org/10.1088/2053-1591/aa96df (**Chapter 4**)
2. **Devesh Kumar**, O. Maulik, S. Kumar, Y.V.S.S. Prasad, V. Kumar, Phase and thermal study of equiatomic AlCuCrFeMnW high entropy alloy processed via spark plasma sintering, Material Chemistry and Physics, vol. 210 (2018) pp 71-77, DOI https://doi.org/10.1016/j.matchemphys.2017.08.049 (**Chapter 5**)
3. **Devesh Kumar**, O. Maulik, A.S. Bagri, Y.V.S.S. Prasad, V. Kumar, Microstructure and characterization of mechanically alloyed equiatomic AlCuCrFeMnW high entropy alloy, Material Today: Proceedings, Vol 3, Issue 9, Part B (2016) pp.2926-2933 DOI https://doi.org/10.1016/j.matpr.2016.09.005 (**Chapter 4**)
4. Ornov Maulik, **Devesh Kumar**, Saurav Kumar, Sheetal Devagan and V. Kumar, Light weight high entropy alloys: A brief review, Materials Research Express, Vol 5, No. 5 (2018) DOI https://doi.org/10.1088/2053-1591/aabbca (**Chapter 2**)
5. **Devesh Kumar**, O. Maulik, V. K. Sharma, Y.V.S.S. Prasad and V. Kumar, Understanding the Effect of Tungsten on Corrosion Behavior of AlCuCrFeMnWx High Entropy Alloys in 3.5 Wt% NaCl Solution, Journal of Materials Engineering and Performance, vol 27 (9). pp 4481-4488, (2018), DOI 10.1007/s11665-018-3536-y (**Chapter 7**)
6. **Devesh Kumar,** V.K.Sharma, Y.V.S.S. Prasad, V. Kumar, Material structure properties correlation of spark plasma sintered AlCuCrFeMnWx high entropy alloys, Journal of Materials Research, vol 34 (5) (2019) pp 767-776, (**Chapter 5 & 6**)

Other Publications

7. Ornov Maulik, **Devesh Kumar**, Saurav Kumar, Daniel M. Fabijanic, and Vinod Kumar, "Structural evolution of spark plasma sintered AlFeCuCrMg$_x$ (x=0, 0.5, 1, 1.7) high entropy alloys", Intermetallics, 77, 2016 pp.46-56.
8. Saurav Kumar, **Devesh Kumar,** Ornov Maulik, A.K.Pradhan, Amar Patnaik and Vinod Kumar, Synthesis and Air jet erosion study of AlxFe1.5CrMnNi0.5 High entropy alloys, metallurgical and materials transactions A, (2018), 49 (11)